Strål
säkerhets
myndigheten
Swedish Radiation Safety Authority

Author: Joel Geier

Technical Note

2014:44

Independent evaluation of the number of critical canister positions in the KBS-3 repository at Forsmark

Main Review Phase

Report number: 2014:44 ISSN: 2000-0456
Available at www.stralsakerhetsmyndigheten.se

SSM perspektiv

Bakgrund

Strålsäkerhetsmyndigheten (SSM) granskar Svensk Kärnbränslehantering AB:s (SKB) ansökningar enligt lagen (1984:3) om kärnteknisk verksamhet om uppförande, innehav och drift av ett slutförvar för använt kärnbränsle och av en inkapslingsanläggning. Som en del i granskningen ger SSM konsulter uppdrag för att inhämta information och göra expertbedömningar i avgränsade frågor. I SSM:s Technical Note-serie rapporteras resultaten från dessa konsultuppdrag.

Projektets syfte

Det övergripande syftet med projektet är att ta fram synpunkter på SKB:s säkerhetsanalys SR-Site för den långsiktiga strålsäkerheten för det planerade slutförvaret i Forsmark. Det specifika målet för denna studie är att genom oberoende beräkningar verifiera antalet kritiska kapselpositioner med hänsyn till seismisk skjuvning genom stora sprickor i berg (N_{crit}) i Tabell 10-17 och 10-18 i SR-Site. Antalet kritiska positioner ingår i beräkningen av sannolikheten för kapselbrott på grund av framtida jordskalv i Forsmark som utgör ett av de mindre sannolika scenarierna i SR-Site för vilket den ekvivalenta stråldosen till omgivningen uppskattas.

Författarens sammanfattning

Oberoende beräkningar genomfördes för att uppskatta antalet kritiska kapselpositioner Ncrit som förväntas förekomma i det planerade slutförvaret i Forsmark. Beräkningarna har baserats på statistiska simuleringar av SKB:s geologiska diskreta spricknätverksmodeller (Geo-DFN), tillämpningen av SKB:s fullperimeter-kriterium (FPC) samt det utvidgade fullperimeter-kriterium (EFPC) som används för att välja bort kapselpositioner som potentiellt skulle kunna korsas av långa sprickor i berg. Nyttjandegraden *DoU* för deponeringstunnlarna har också tagits fram från realiseringar av den föreslagna slutförvarslayouten D2.

Tre olika Geo-DFN alternativ utvecklade av Fox m.fl. (2007) har utvärderats: (1) ”r_0-fixed” modell, (2) OSM+TFM (”outcrop-scale” modell + ”tectonic fault” modell) och (3) TCM (”tectonic continuum” modell). Effekten av variationen hos sprickintensiteten (P_{32}) har också studerats genom en 25% ökning av sprickintensiteten för de tre Geo-DFN-alternativen. Stokastiska realiseringar av Geo-DFN-modellerna har använts som utgångspunkt för en explicit simulering av depositionshåls-gallringsprocessen genom tillämpningen av FPC och EFPC längs med deponeringstunnlarna i Forsmarks slutförvarslayout.

Beräkningarna av Ncrit baseras på sprickor med kritisk radie i förhållande till fem deformationszoner; ZFMNW0017, ZFMNW1200, ZFMWNW0123, ZFMNW0809A och ZFMA2, som antas vara seismiskt aktiva, såväl som två zoner; ZFMENE0060A och ZFMNE0062A, som antas vara seismiskt inaktiva enligt Munier (2010).

Beräknade värden för nyttjandegrad (*DoU*) är i denna studie något högre, ca 3%, än SKB:s beräknade värden. Skillnaden kan förklaras av valet av ett konstant c-c-avstånd på 6,0 m mellan deponeringspositionerna som gäller bergdomän RFM029 och även bränsleförvarsdelarna som ligger i RFM045 där SKB använder ett större c-c-avstånd på 6,8 m.

Värdena för N_{crit} beräknande i denna studie är generellt högre än de beräknade av SKB med en faktor på mellan 2,5 och 14 beroende på Geo-DFN-modellen. Vissa implementeringsskillnader – såsom en kortare tunnellängd baserad på den aktuella layouten D2 – förklarar endast en liten del av skillnaden i N_{crit}. Därför rekommenderas ytterligare granskning av de matematiska antagandena i SKB:s beräkningsmodell. Särskilt SKB:s värden för N_{crit} för en av de längre deformationszonerna ZFMNW0017 förefaller vara onormalt låga även i jämförelse med de värden SKB har tagit fram för andra deformationszoner.

De kritiska positioner som påträffats i denna studie förekommer huvudsakligen nära ändarna av deponeringstunnlarna. När kritiska positioner ligger nära ingången av deponeringstunneln är geometrin sådan att sprickan bör skära även den intilliggande huvudtunneln. Antigen i detta fall eller i det fallet då den kritiska positionen förekommer nära slutet av deponeringstunneln kan sprickan ofta även undvikas i intilliggande deponeringstunnlar tack vare liknande fullperimeterskärningar. Därför stöds SKB:s antagande, att många av de kritiska sprickorna kan undvikas genom att använda geoinformationen från flera tunnlar, av resultaten i denna studie.

Projektinformation
Kontaktperson på SSM: Flavio Lanaro
Diarienummer ramavtal: SSM2011-3628
Diarienummer avrop: SSM2013-2408
Aktivitetsnummer: 3030012-4053

SSM perspective

Background

The Swedish Radiation Safety Authority (SSM) reviews the Swedish Nuclear Fuel Company's (SKB) applications under the Act on Nuclear Activities (SFS 1984:3) for the construction and operation of a repository for spent nuclear fuel and for an encapsulation facility. As part of the review, SSM commissions consultants to carry out work in order to obtain information and provide expert opinion on specific issues. The results from the consultants' tasks are reported in SSM's Technical Note series.

Objectives of the project

The general objective of the project is to provide review comments on SKB's postclosure safety analysis, SR-Site, for the proposed repository at Forsmark. In particular, the goal of this study is to verify that independent calculations yield results on the number of canisters in critical positions with respect to seismic shearing through large rock fractures (N_{crit}) similar to those contained in Table 10-17 and 10-18 in SKB TR-11-01. The number of critical position is an input to the calculation of the probability of canister failure due to a future earthquake at Forsmark. This is one of the low probability scenarios in SR-Site for which the equivalent dose to the environment is calculated.

Summary by the Author

Independent calculations were carried out to estimate N_{crit}, the number of canisters in critical positions that can be expected in the proposed repository at Forsmark, based on statistical simulations of SKB's geological discrete-fracture network (Geo-DFN) models, and taking into account SKB's full-perimeter criterion (FPC) and extended full-perimeter criterion (EFPC) to screen out canister positions that can be identified as potentially intersected by large fractures. Degree-of-utilization factors *DoU* for the deposition tunnels are also obtained from the simulations of the proposed repository layout D2.

Three different Geo-DFN alternatives as developed by Fox et al. (2007) were assessed: (1) r_0-fixed model, (2) OSM+TFM (outcrop-scale model + tectonic fault model), and (3) TCM (tectonic continuum model). Consequences of variation of fracture intensity (P_{32}) were also scoped by considering a 25% increase in fracture intensity for each of the three Geo-DFN alternatives. Stochastic realizations of the Geo-DFN models were used as the basis for explicit simulation of the deposition-hole screening process along deposition tunnels in the Forsmark repository layout, using FPC and EFPC.

The calculations of Ncrit are based on critical radii of fractures relative to the five deformation zones ZFMNW0017, ZFMNW1200, ZFMWNW0123, ZFMNW0809A and ZFMA2 considered as potentially seismically active, as well as for two zones ZFMENE0060A and ZFMNE0062A that were considered as inactive by Munier (2010).

DoU values calculated in the present study are slightly higher than SKB has calculated, by about 3%. This difference is largely accounted for by the use of a fixed spacing of 6.0 m between canisters in rock domain RFM029, even in the portion of the repository that lies within RFM045, where SKB used a larger canister spacing of 6.8 m.

The values of N_{crit} obtained here are generally higher than those of SKB, by factors ranging from 2.5 to 14 depending on the Geo-DFN alternative. Differences in implementation that have been identified – primarily a smaller average tunnel length based on the actual layout D2 – can account for only a small part of this difference. Therefore further examination of the mathematical assumptions of SKB's model is advisable. In particular, SKB's values of N_{crit} for one of the longer deformation zones, ZFMNW0017, appear to be anomalously low even in comparison with SKB's calculations for other deformation zones.

The critical positions that were found in the present study are mainly near the ends of deposition tunnels. When critical positions occur near the plug end of a deposition hole, the geometry is frequently such that the fracture would intersect the adjacent access tunnel. For either this case or the case in which critical intersections occur near the blind end of a deposition tunnel, frequently the same fracture would be avoided in neighboring tunnels based on full-perimeter intersections. Hence SKB's argument that many of these fractures could be avoided by making use of information from multiple tunnels, is supported by the results of this study.

Project information
Contact person at SSM: Flavio Lanaro

Strål
säkerhets
myndigheten
Swedish Radiation Safety Authority

Author: Joel Geier
Clearwater Hardrock Consulting, Corvallis, Oregon, USA

Technical Note 65

2014:44

Independent evaluation of the number of critical canister positions in the KBS-3 repository at Forsmark

Main Review Phase

Date: July, 2014
Report number: 2014:44 **ISSN:** 2000-0456
Available at www.stralsakerhetsmyndigheten.se

This report was commissioned by the Swedish Radiation Safety Authority (SSM). The conclusions and viewpoints presented in the report are those of the author(s) and do not necessarily coincide with those of SSM.

Contents

1. Introduction

The Swedish Nuclear Fuel and Waste Management Co. (SKB) has presented a technique for inferring the number of radioactive-waste canisters in positions that are critical concerning the risk of failure due to shearing caused by earthquakes (Munier, 2010). SKB's calculations are based on the application of the following models and methods:

- A stochastic geological discrete-fracture network (Geo-DFN) description of the fractures on scales of up to 1 km which could occur in the repository volume (Fox et al., 2007).
- A deterministic description of deformation zones on larger scales (SKB, 2008) which are considered as potential hosts of future earthquakes;
- The *full-perimeter criterion* (FPC) and the *extended full perimeter criterion* (EFPC) for avoiding large fractures in the selection of deposition-hole positions (Munier, 2010).
- Modelling results regarding shear displacements on single rock fractures due to hypothetical earthquakes on nearby deformation zones (Fälth et al., 2010).

The EFPC is also referred to as the "extended full perimeter intersection criterion" in some places in the SR-Site main report (SKB TR 11-01), but this longer term is not used consistently either in that report or by Munier (2010).

The main results yielded by these calculations are estimates of the number of canisters (N_{crit}) that would be placed in critical positions for a full repository of 6000 spent-fuel canisters, for a given Geo-DFN model variant and assuming that the EFPC is applied consistently throughout the proposed repository at Forsmark. The value of N_{crit} directly affects the evaluated risk for the shear-failure scenario.

As a secondary result, the calculations also yield estimates of the degree of utilization *DoU*, which is a measure of the percentage of the total length of deposition tunnels that will be suitable for waste package emplacement. The utilization percentage affects whether or not the design layout will contain sufficient space for the planned number of waste packages.

SKB's calculations are based on application of a series of analytical and numerical methods, taking into account the stochastic properties of the Geo-DFN model. Due to the complex nature of these calculations and the importance of the results for the evaluation of risk for the shear failure scenario, the Swedish Radiation Safety Authority (SSM) has commissioned independent calculations to verify the outcome. This technical note presents the methodology and results of these calculations.

2. Evaluation of number of critical canister positions

2.1. SKB's presentation

2.1.1. SKB's definition of critical positions

Munier (2010, p. 11) defines a critical position as "[a] canister position that is intersected by a fracture able to host a slip exceeding the canister failure criterion." Such a fracture is referred to by Munier (2010) as a "critical fracture."

In practice, Munier (2010) assesses critical positions based on whether a fracture (assumed to be disc-shaped) that intersects a given canister position has a radius that exceeds some critical radius. The "critical radius," denoted r_{crit}, is the minimum radius for which a fracture with a given dip, and at a given distance from any of the nearby deformation zones which are considered to be potentially unstable faults, is expected to be able to host a slip exceeding the canister failure criterion of 5 cm (SKB, 2011).

Critical radii for different categories of deformation zones are assessed based on modelling by Fälth et al. (2010), as summarized in Table 7-2 of Munier (2010). This table is reproduced here as Table 1. It may be noted that the precise meaning of the notation for critical radius "> 300 m" or ">> 300 m" is not clear. Following the conventions of mathematics these notations apparently should be interpreted as "greater than 300 m" and "much greater than 300 m," but how much greater appears to be a matter of judgement. A conservative approach used in the present assignment has been to treat the critical radius for these categories as equal to 300 m, in the first case, and 400 m in the second case.

For Forsmark, Munier (2010) identifies two deformation zones with trace length greater than 5 km:

ZFMNW0017
ZFMWNW0123

and three deformation zones with trace length between 3 and 5 km:

ZFMNW1200
ZFMWNW0809A
ZFMA2

as potentially unstable zones that should be used to assess the critical fracture radius for a given canister position, based on the results of Fälth et al. (2010). These deformation zones are shown in relation to the repository layout in Figure 1. Two additional, subvertical deformation zones in the 3 to 5 km trace length category are regarded by SKB as always stable:

ZFMENE0060A
ZFMENE0062A

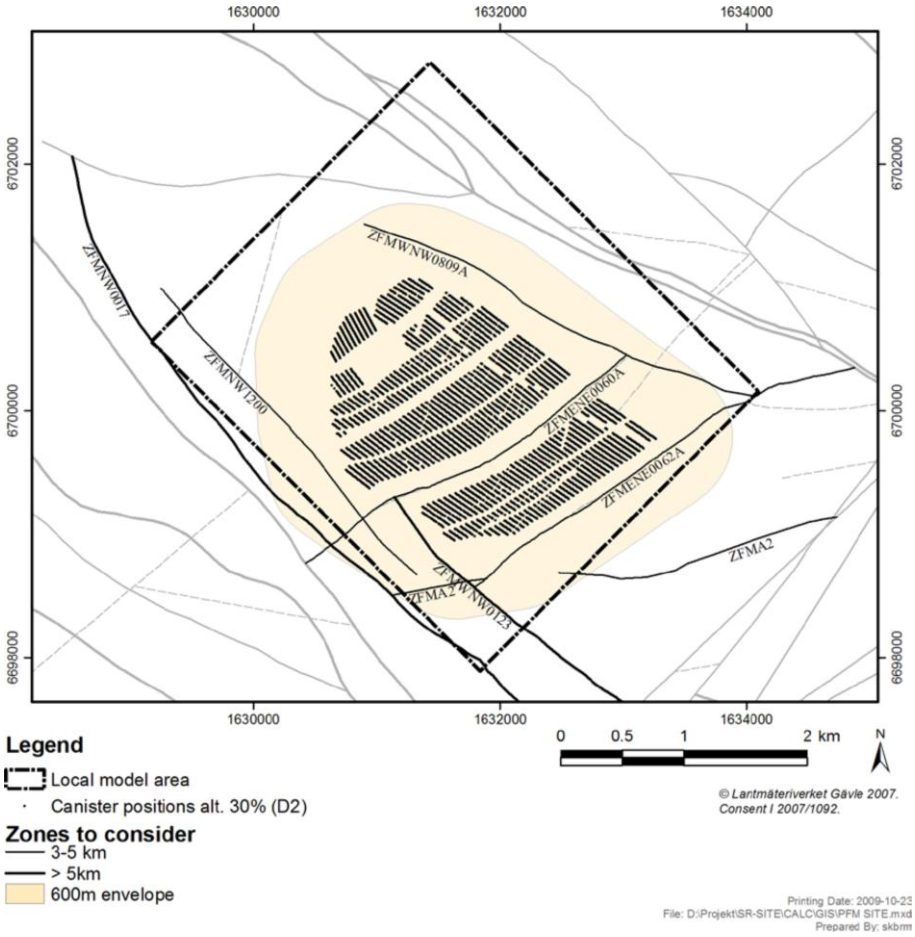

Figure 1: Deformation zones considered as potentially unstable in the present calculations. The deformation zones are shown as traces in the plane of the repository, in relation to the positions of canisters along deposition tunnels as considered by Munier (2010) in N_{crit} calculations for Forsmark. Figure based on Figure 7-2 of Munier (2010).

Table 1: Relationship between deformation zone trace length, target fracture dip, distance from deformation zone and critical target fracture radius (reproduced from Munier, 2010, based on results of Fälth et al., 2010).

Zone trace length (km)	Target fracture dip (degrees)	Distance from zone (m)	Critical target fracture radius (m)
>5	0–55	100–200	62.5
>5	0–55	200–400	125
>5	0–55	400–600	160
>5	0–55	>600	225
>5	55–90	100–200	85
>5	55–90	200–400	170
>5	55–90	400–600	215
>5	55–90	>600	>300
3–5	0–55	100–200	75
3–5	0–55	200–400	150
3–5	0–55	400–600	235
3–5	0–55	>600	>300
3–5	55–90	100–200	100
3–5	55–90	200–400	200
3–5	55–90	400–600	>300
3–5	55–90	>600	>>300

In the most conservative analysis by Munier (2010), a canister position is judged to be a critical position if it is intersected by a fracture of radius $r \geq r_{crit}$.

If credit is taken for the theoretical decay of slip toward the circumference of a circular fracture with zero-displacement conditions at the boundaries, a modified critical radius can be calculated as (Munier, 2010, Eq. 28):

$$r'_{crit} = \sqrt{r^2 - r_{crit}^2} \ , \quad r > r_{crit} \qquad \text{Eq. (2.1)}$$

With this assumption, a shear displacement exceeding the allowable displacement across a canister is only exceeded if the canister lies with a distance r'_{crit} of the fracture center.

Note that Munier (2010) used the notation r_{Min} in place of r_{crit} as used here. The notation rCritMin is also used by Munier (2010).

It should be noted that the theoretical decay of slip toward the boundary (i.e. the circumference) of a circular fracture is based on the assumption of zero displacement at the boundary. A substantial percentage of the fractures at Forsmark are observed to terminate at other fractures, rather than in intact rock (Fox et al., 2007). For such fractures, the zero-displacement boundary condition assumed by Munier (2010) and Hedin (2011) might not be conservative.

Munier (2010, p. 54) and Hedin (2011) argue for a further reduction in the portion of a fracture over which, probabilistically speaking, a critical shear displacement could take place, due to differences in fracture orientation and location relative to the fault tip. This reasoning leads to a "probabilistic" mean critical radius:

$$\tilde{r}'_{crit} = \sqrt{r^2 + r_{crit}^2 - 2rr_{crit}} \qquad \text{Eq. (2.2)}$$

The last version of the critical fracture radius has not been utilized in the present study. However, independent calculations are given in terms of r_{crit} and r'_{crit}.

2.1.2. SKB's definitions of FPI, FPC and EFPC

A fracture is considered to make a *full perimeter intersection* (FPI) with a tunnel if its trace is visible across the roof, sides, and floor of the tunnel, to identify traces of large fractures in a tunnel.

The basic *full perimeter criterion* (FPC) as defined by Munier (2010, p. 11) means that any deposition hole intersected by the extrapolation of an FPI-generating fracture to an infinite plane will be considered for rejection regardless of the true fracture size.

In an initial application by (Munier, 2006), a position was rejected as potentially critical if the extrapolation of the FPI fracture intersected any part of the planned deposition hole. In the application by Munier (2010) for SR-Site, the FPC was relaxed such that a position is regarded as potentially critical only if the extrapolation of the FPI fracture intersects any portion of the planned canister position within the deposition hole. The difference between these two versions of the FPC is illustrated in Figure 2.

For brevity in this technical note, where it is necessary to distinguish between these two definitions of FPC, the more conservative criterion of Munier (2006) based on any intersection with a deposition hole is referred to as FPC(hole), while the criterion based on intersections with canister positions used by Munier (2010) is referred to as FPC(can).

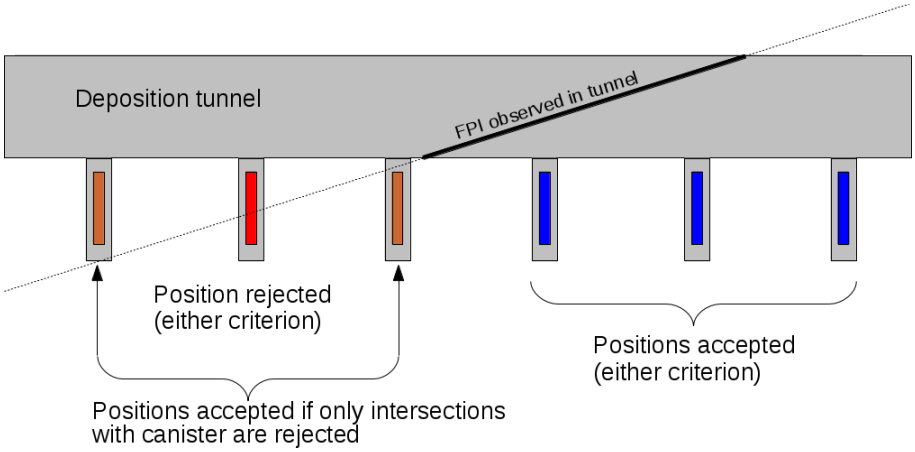

Figure 2: Illustration of the difference between the FPC(hole) and FPC(can) versions of the full perimeter criterion (FPC).

The *extended full perimeter criterion* (EFPC) as defined by Munier (2010, p. 12-13) is an extended version of the FPC. Munier (2010) also refers to this as the "expanded full perimeter intersection criterion." With the EFPC, deposition holes are excluded even if they are acceptable based on the FPC, if they are crossed by any large fracture that can be detected in n' consecutive deposition holes (where n' is some specified integer). Munier (2010) considers values of n' in the range from 2 to 5. Figure 3 shows a plan-view illustration of deposition-hole positions that could be rejected based on an EFPC with $n' < 5$.

Munier (2010, p. 57) considers fractures to be detectable in a deposition hole, for the purpose of the EFPC, only if the fracture makes a full-perimeter intersection with the deposition hole. With this strict criterion for detectability within deposition holes, the two disc-shaped fractures shown in Figure 3 would not be regarded as detectable in the fifth deposition hole from the left, because they only make partial-perimeter intersections with this deposition hole. In the present study, this version of the EFPC is referred to as "EFPC with strict detectability." Fractures that are detectable in more than n' consecutive deposition holes are referred to in this technical note as "EFPC fractures."

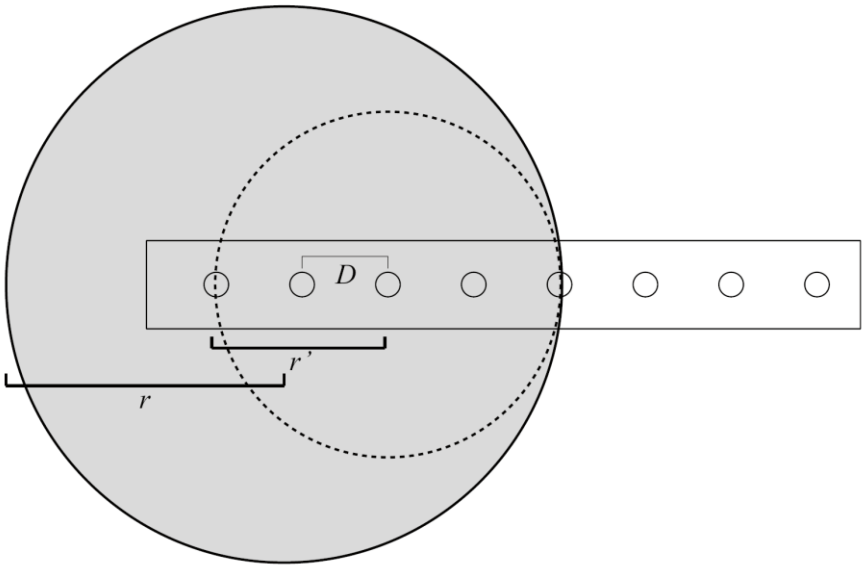

Figure 3: Illustration of the extended full perimeter criterion, EFPC (from Munier, 2010, Figure 3-3).

The EFPC can be applied to exclude any deposition hole that is intersected by an EFPC fracture, or less conservatively, only those deposition holes for which an EFPC fracture would intersect the canister position. These two cases are referred to herein as EFPC(hole) and EFPC(can), analogous to the notation that has been introduced for the FPC.

According to the account given Munier (2010), the EFPC(can) version of the EFPC, with strict detectability, is used together with the FPC(can) as the main case for SR-Site. Possible geometries of intersection between a fracture and a tunnel or deposition hole idealized as a cylinder are illustrated in Figure 4.

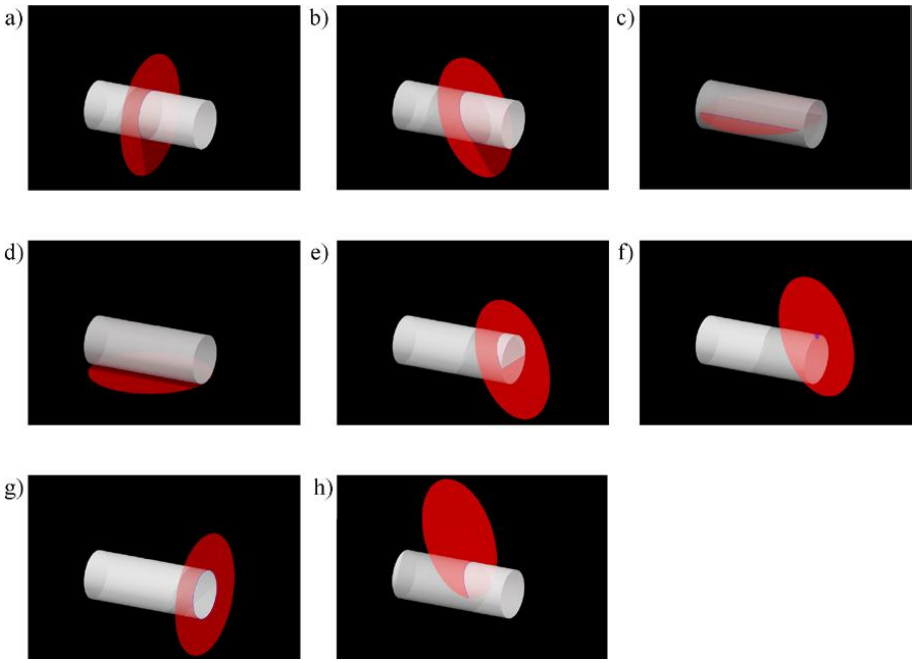

Figure 4: Possible intersection geometries between a plane and a finite cylinder. Cases “c” and “h” can only occur for finite discs (assumed for EFPC) whereas the remaining cases can also occur for infinite planes (assumed for FPC). The illustration is from Munier (2010, Figure 4-1).

2.2. Motivation of the assessment

The goal of this assignment is to verify, by independent calculations, SKB's results for N_{crit}, the number of canisters in critical positions after taking credit for use of the FPC and EFPC to screen out canister positions that can be identified as potentially intersected by large fractures. These results have been presented by SKB as Tables 7-5 and 7-6 of Munier (2010), and as Tables 10-17 and 10-18 of SKB (SKB, 2011).

The independent calculations make use of the parameters of SKB's Geo-DFN models for the following variants as developed by Fox et al. (2007) and with parameters summarized by Munier (2010, Appendix 3):

- r_0-fixed model
- OSM+TFM (outcrop-scale model + tectonic fault model)
- TCM (tectonic continuum model)

The aim has been to mimic, as closely as possible with independent software and numerical algorithms, SKB's description of the implementation of the FPC(can) and EFPC(can) criteria for simulations of the proposed repository layout for Forsmark.

Specific aspects considered in these calculations include:

- The critical radii for deformation zones of different length as described in Fälth et al. (2010), for the "active" deformation zones at Forsmark as listed in Munier (2010), Table 7-3;

- The contribution to N_{crit} when considering zones ZFMA2, ZFMENE0060A and ZFMNE0062A along with the zones that have been assessed as "active;"

- The effect of considering variation of P_{32} according to a gamma distribution of the fracture intensity P_{32} in the repository volume (as assessed by Fox et al., 2007).

The last issue is assessed here by considering a globally elevated-P_{32} with a value 25% larger than the average P_{32} proposed by SKB. Based on scoping calculations an increase of 18% would correspond to the 60th percentile of the gamma distribution for P_{32} in rock domain FFM01, as fitted by Fox et al. (2007). It is not expected that this elevated value of P_{32} would apply across the whole repository volume, but the consequences have been investigated by considering a homogeneous increase in P_{32}.

In addition to the primary objective of verifying calculations of N_{crit}, degree-of-utilization factors *DoU* are also of interest for confirming SKB's estimates of the number of waste packages that can be emplaced in the available space. These factors can be calculated as by-products of simulating the implementation of the FPC and EFPC criteria for the proposed repository layout.

2.3. The Consultant's assessment of N_{crit}

The approach to estimating the number of critical fracture positions makes use of the Discrete-Feature Model (DFM) software as described by Geier (2008). The main steps are:

1) Stochastic simulation of the fracture population in the vicinity of the proposed repository;
2) Simulation of the adaptive placement of deposition holes within the repository layout;
3) Identification of intersections between fractures and deposition holes, and
4) Identification of critical fractures.

The calculations make use of the following modules of the DFM software:

fracgen (version 2.4.1.1, executable fracgen2411 compiled March 5, 2014);

repository (version 2.4.1.1, executable repository2411 compiled February 17, 2014);

pancalc (version 2.4.1.1, executable pancalc2411 compiled February 17, 2014).

The details of the steps in these calculations are described in the following subsections.

2.3.1. Stochastic simulation of the fracture population

Selection of DFN model variants

Statistical models for the following "alternatives" of SKB's Geo-DFN models for fracture domains FFM01 and FFM06 were simulated based on the tables given in Appendix 3 of Munier (2010):

- r_0-fixed alternative
- OSM + TFM alternative
- TCM alternative ("k_r-fixed")

For each of these alternatives, an elevated-P_{32} variant was also tested to scope the consequences of fracture intensities higher than the mean estimated values.

Fox et al. (2007) suggested the gamma distribution as a model for variability in P_{32} for the Geo-DFN, on scales of 6 to 30 m. The gamma function for a given variable x

has probability density function:

$$p(x) = \frac{x^{\alpha-1}e^{-x/\beta}}{\Gamma(\alpha)\beta^{\alpha}}, x > 0 \quad \text{Eq. (2.3)}$$

and cumulative density function:

$$P\left(\alpha, \frac{x}{\beta}\right) = \frac{\gamma(\alpha,x)}{\Gamma(\alpha)} \quad \text{Eq. (2.4)}$$

where $P(\alpha,x) = \gamma(\alpha,x))/\Gamma(\alpha)$ is the normalized incomplete gamma function. The percentiles of the gamma distribution for P_{32} for a given fracture set can be calculated by solving:

$$P\left(\alpha, \frac{x}{\beta}\right) = q \quad \text{Eq. (2.5)}$$

in terms of the random variable x (x stands for P_{32}, in this case) for a given percentage q.

Fox et al. (2007, Table 4-96) list fitted values for the shape parameter α and scale parameter β, based on scales of either 6 or 30 m, for all except two of the fracture sets that they defined for fracture domain FFM01, and all of the fracture sets that they defined for FFM06. These fitted values of α and β were used to calculate resulting quantiles for FFM01 and FFM06 (r_0-fixed alternative), as plotted in Figure 5.

Using the 60th percentile values for each of these fracture sets, and assuming a uniform value of P_{32} for the two fracture sets for which Fox et al. (2007) were not able to fit a gamma distribution, results in an 18% increase in total P_{32} for FFM01 and a 28% increase in total P_{32} for FFM06, compared with the median values.

Fox et al. (2007) did not investigate whether the distributions of P_{32} that they estimated independently for the different fracture sets are strongly correlated (which would lead to a larger probability of all fracture sets having high P_{32} in a given part of the host rock), or if they are independent (in which case even a modest increase in overall P_{32} might be viewed as highly improbable).

The approach taken here is to assume that these distributions are correlated, in order to formulate a conservative case to scope the consequences in terms of the number of critical canister positions. A simultaneous increase of 25% in the P_{32} values for all fracture sets is used to scope this possibility.

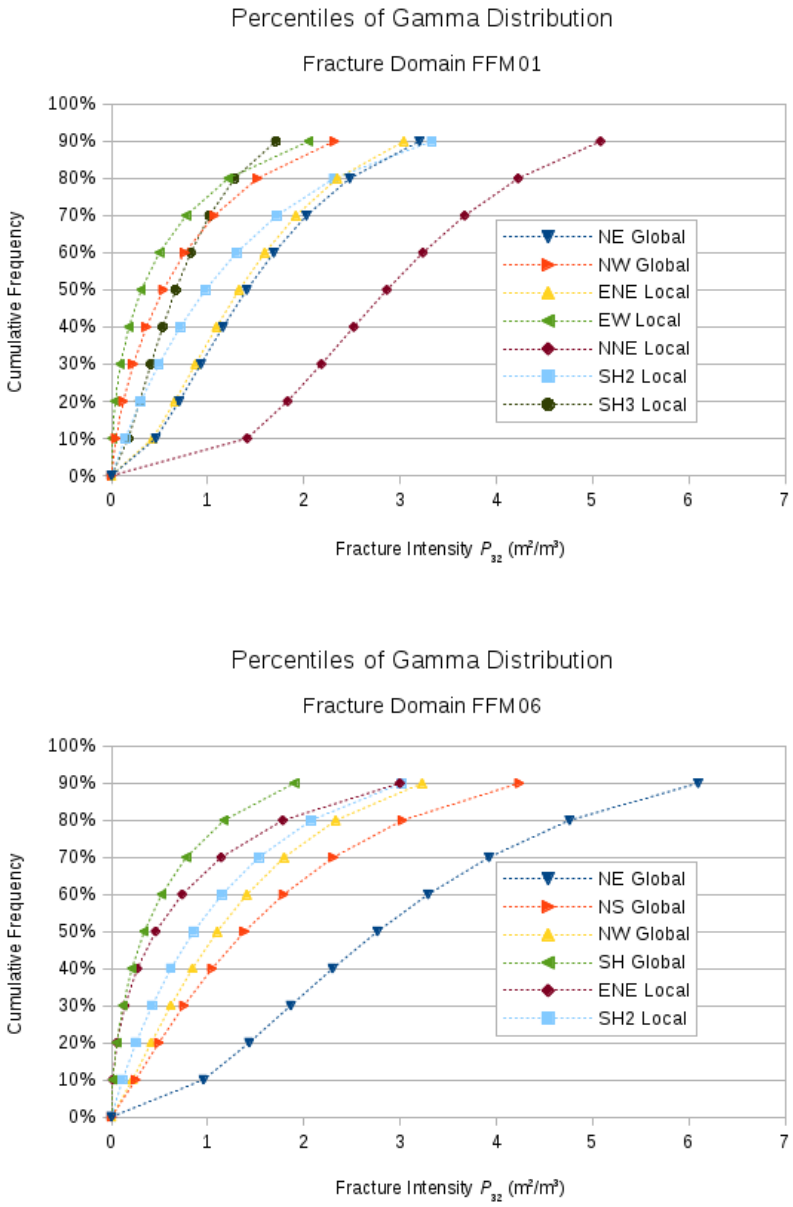

Figure 5: Cumulative density functions of P_{32} fracture intensity for fracture sets in fracture domains FFM01 and FFM06, calculated from the parameters estimated by Fox et al. (2007).

Fracture domain geometry

Fracture domains in SKB's nomenclature define the volumes within which a given statistical model of the fracture population is considered to apply. The geometry of the fracture domain boundaries for the present analysis was defined based on the following delivery from SKB to SSM:

Data Delivery	skb#09_04 (0:4)
Date:	2009-06-09
Delivered by:	Veronika Linde
Delivered to:	Sven Tirén, Geosigma AB
Description:	*FD_PFM_v22.01 basemodel_joel* (file translated to AutoCAD® DXF format by Geosigma AB)

A more recent delivery obtained by SSM for the purpose of rock mechanics models which required a different format was not utilized. Geosigma AB checked this newer delivery (skb#13_03_SSM , 2013-09-16, SKB Document ID 1407195) and found no significant differences with the previous delivery (skb#09_04 (0:4)).

Further processing of the data describing fracture domain geometry to the format used in the DFM software is documented by Geier (2010). For the present analysis, only fracture domains FFM01 and FFM06 are utilized.

Fracture properties and statistical distributions

Each individual fracture in the DFN model simulations is idealized as a circular disc characterized by three purely geometric attributes (see Figure 6):

$\boldsymbol{x}_c$	location (3-D coordinates of the disc center),
r	radius of disc,
$\boldsymbol{n}$	orientation (vector normal to the disc, also called fracture pole).

In addition, three hydrogeological properties are assigned to each fracture:

T	transmissivity,
S	storativity, and
b_T	transport aperture (effective aperture for solute transport).

These properties are not needed in the context of the present study, as critical fracture intersections are defined strictly based on the geometry of intersections with deposition holes. However, the DFM-*fracgen* software module used to generate realizations of the fracture population requires that these properties be defined. Therefore arbitrary constant values have been assigned for transmissivity and storativity for all fracture sets: $T = 10^{-10}$ m^2/s and $S = 10^{-8}$. The transport aperture is calculated from T based on the cubic law (Snow, 1965; Witherspoon et al., 1979), resulting in a value $b_T \approx 0.01$ mm for all fractures.

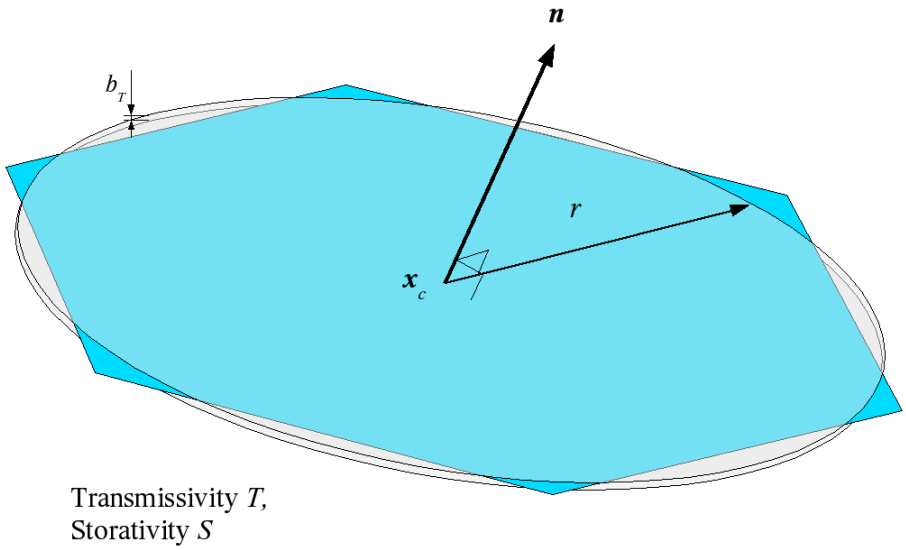

Figure 6: Geometric attributes of disc-shaped fractures and representation as equivalent polygon (hexagon).

a) Location

For a given fracture set, fracture locations are simulated by a 3-D stochastic process. For each of the fracture sets in the Geo-DFN models as defined by Fox et al. (2007) and used by Munier (2010), a 3-D Poisson process is used. This results in fracture locations which are uniformly random in three dimensions, within the specific fracture domain.

b) Fracture radius

Fracture radius is defined in terms of a scalar probability distribution for r. For all of the fracture sets specified in SKB's model variants as considered here, a power-law distribution is used:

$$f(r) = \frac{k_r r_0^{k_r}}{r^{k_r+1}}, r \geq r_0 \qquad \text{Eq. (2.6)}$$

where r_0 is the minimum fracture radius for which the distribution is considered to apply, and k_r is an empirical constant that describes how rapidly the number of fractures decays with increasing radius.

c) Orientation

Fracture orientation is described by a directional probability distribution for the normal vector $\boldsymbol{n}$, which can be expressed in terms of spherical polar coordinates (θ,ϕ) or in geological coordinates as a trend and plunge of the normal vector $\boldsymbol{n}$ (analogous to the method used to describe lineations). The relationship between these two alternative ways of describing $\boldsymbol{n}$ is depicted in Figure 7.

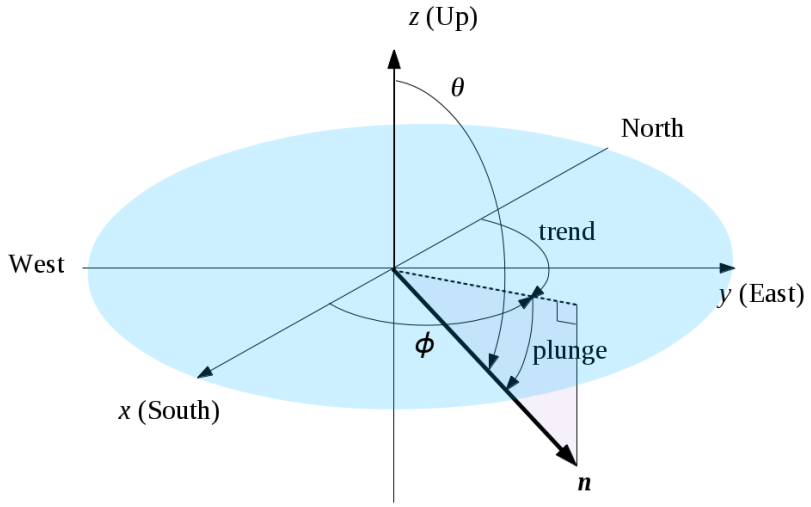

Figure 7: Relationship between spherical polar coordinates and geological coordinates for describing the direction of a fracture normal vector. The shaded area indicates the horizontal plane.

For each of the fracture sets in the Geo-DFN models as defined by Fox et al. (2007) and used by Munier (2010), the probability distribution for fracture orientation is in the form of a Fisher distribution (Mardia, 1972; Mardia et al., 1979), which has the following probability density function in spherical coordinates:

$$p(\omega, \psi; \kappa, \bar{\theta}, \bar{\phi}) = \frac{\kappa}{2sinh\kappa} sin\omega e^{\kappa cos\omega} \quad \text{Eq. (2.7)}$$

where ω is the polar angle of the direction vector (θ,ϕ) as measured from the mean direction $\bar{n}$(with components$(\bar{\theta}, \bar{\phi})$in spherical polar coordinates), and ψ is a uniformly random angular rotation from 0 to 2π about an axis through the mean direction $(\bar{\theta}, \bar{\phi})$. The parameter κ is referred to as the Fisher concentration parameter. High values of κ (*e.g.* more than 10) imply a strongly clustered distribution of poles about the mean pole. Lower values of κ imply a wider spread. In the limit as $\kappa \rightarrow 0$, the Fisher distribution becomes a spherically uniform distribution with no preferred orientation.

d) Fracture intensity

The number or density of fractures belonging to a given fracture set, within a particular fracture domain, is governed by the fracture intensity measure P_{32} as defined by Dershowitz and Herda (1990):

$$P_{32} = \frac{\sum_{i=1}^{n} A_i}{V_\Omega} \quad \text{Eq. (2.8)}$$

where:

n = the number of fractures,
V_Ω = the volume of the generation domain Ω,
A_i = the area of the part of the ith fracture that is inside Ω.

The scaled fracture intensity for a given increment of the fracture size (radius) distribution $r_1 \le r \le r_2$ is:

$$P_{32}[r_1, r_2] = \int_{r_1}^{r_2} \frac{k_r r_0^{k_r}}{r^{k_r+1}} dr \qquad \text{Eq. (2.9)}$$

When a power-law is used for the fracture size distribution (as is the case for all fracture sets in the Geo-DFN models for FFM01 and FFM06), this becomes:

$$\frac{P_{32}[r_1, r_2]}{P_{32}[0, \infty]} = \frac{\int_{r_1}^{r_2} \frac{k_r r_0^{k_r}}{r^{k_r+1}} r^2 dr}{\int_{r_0}^{\infty} \frac{k_r r_0^{k_r}}{r^{k_r+1}} r^2 dr} = \frac{r_1^{2-k_r} - r_2^{2-k_r}}{r_0^{2-k_r}} = \left(\frac{r_0}{r_1 r_2}\right)^{k_r-2} \left(r_2^{k_r-2} - r_1^{k_r-2}\right) \qquad \text{Eq. (2.10)}$$

for $k_r > 2$ and $r_2 \ge r_1 \ge r_0 > 0$.

Calculation cases

Six different calculation cases are defined in this report:

- r_0-fixed alternative, "base case" (r3)
- r_0-fixed alternative, elevated-intensity variant (rg2)
- OSM + TFM alternative, "base case" (o3)
- OSM + TFM alternative, elevated-intensity variant (og3)
- TCM alternative, "base case" (t2)
- TCM alternative, elevated intensity variant (tg2)

The parameters for these calculation cases are listed in Tables 2 through 7. The fracture set definition files are listed in Appendix 2. Ten realizations have been generated and evaluated for each of the six calculation cases.

The most important difference among these models is the variation of fracture intensity as a function of size. Figures 8 through 10 show the theoretical distributions of fracture intensity as function of fracture radius for the base case of each of the three alternatives, for each of the two fracture domains FFM01 through FFM06. In Figure 8, the distributions are plotted as the cumulative distribution summed over all fracture sets. In Figures 9 and 10, the distributions are plotted as histograms giving the intensity for discrete increments of fracture radius, with the contributions of the different fracture sets distinguished by colour. These histograms show only the contribution of fractures with radius larger than 3 m (roughly, the

minimum fracture radius that can produce a full-perimeter intersection with a deposition tunnel).

The most noticeable difference among the alternatives is that the fracture intensity attributed to fractures with radius r larger than 3 m is much higher for the TCM alternative, in comparison with either the r_0-fixed or the OSM-TFM alternative. This is especially apparent from the histograms plotted in Figures 9 and 10.

From Figure 8 it can be seen that, even though the total fracture intensity is similar for all three alternatives, the fraction attributed to fractures with $r < 1$ m is much higher for the r_0-fixed and OSM-TFM alternatives than for the TCM alternative, and this difference persists for r up to 3 m.

Another significant difference is that the OSM-TFM model has elevated intensity for fracture radii in the range from about 30 to 100 m, in comparison with the r_0-fixed and TCM alternatives. This is in the range where the larger TFM (tectonic fault model) fracture sets begin to show up. The ENE- and NE-striking TFM sets are especially dominant.

Table 2: Parameters for generation of fracture sets for fracture domain FFM01, r_0-fixed alternative, Calculation Cases r3 (base case) and rg2 (elevated-P_{32}). For all sets r_{min} = 3 m and r_{max} = 564.2 m.

Set	Mean pole trend (°)	Mean pole plunge (°)	Fisher concen-tration κ	r_0 (m)	k_r (-)	Base case P_{32} (unscaled) (m^{-1})	Elevated P_{32} (unscaled) (m^{-1})
NE global	314.9	1.3	20.94	0.039	2.72	1.733	2.166
NS global	270.1	5.3	21.34	0.039	2.75	1.292	1.615
NW global	230.1	4.6	15.70	0.039	2.61	0.948	1.185
SH global	0.8	87.3	17.42	0.039	2.58	0.624	0.780
ENE local	157.5	3.1	34.11	0.039	2.97	0.256	0.320
EW local	0.4	11.9	13.89	0.039	2.93	0.169	0.211
NNE local	293.8	0.0	21.79	0.039	3.00	0.658	0.823
SH2 local	164.0	52.6	35.43	0.039	2.61	0.081	0.101
SH3 local	337.9	52.9	17.08	0.039	2.61	0.067	0.084

Table 3: Parameters for generation of fracture sets for fracture domain FFM06, r_0-fixed alternative, Calculation Cases r3 (base case) and rg2 (elevated-P_{32}). For all sets r_{min} = 3 m and r_{max} = 564.2 m.

Set	Mean pole trend (°)	Mean pole plunge (°)	Fisher concen-tration κ	r_0 (m)	k_r (-)	Base case P_{32} (unscaled) (m^{-1})	Elevated P_{32} (unscaled) (m^{-1})
NE global	125.7	10.1	45.05	0.039	2.79	3.299	4.124
NS global	91.0	4.1	19.49	0.039	2.78	2.150	2.688
NW global	34.1	0.8	16.13	0.039	2.66	1.608	2.010
SH global	84.3	71.3	10.78	0.039	2.58	0.640	0.800
ENE local	155.4	8.3	20.83	0.039	2.87	0.194	0.243
SH2 local	0.0	47.5	12.71	0.039	2.61	0.429	0.536

Table 4: Parameters for generation of fracture sets for fracture domain FFM01, OSM-TFM alternative, Calculation Cases o3 (base case) and og3 (elevated-P_{32}). For all OSM sets r_{min} = 3 m. For all TFM sets r_{min} = 28 m. For all sets r_{max} = 564.2 m.

Set	Mean pole trend (°)	Mean pole plunge (°)	Fisher concen-tration κ	r_0 (m)	k_r (-)	Base case P_{32} (scaled) (m^{-1})	Elevated P_{32} (scaled) (m^{-1})
OSM NE global	314.9	1.3	20.94	0.0385	2.60	0.0800	0.1001
OSM NS global	270.1	5.3	21.34	0.0385	2.90	0.0222	0.0277
OSM NW global	230.1	4.6	15.70	0.0385	2.44	0.0827	0.1034
OSM SH global	0.8	87.3	17.42	0.0385	2.61	0.0321	0.0401
OSM ENE local	157.5	3.1	34.11	0.0385	2.20	0.0283	0.0354
OSM EW local	0.4	11.9	13.89	0.0385	3.06	0.0015	0.0019
OSM NNE local	293.8	0.0	21.79	0.0385	3.00	0.0075	0.0094
OSM SH2 local	164.0	52.6	35.43	0.0385	2.61	0.0042	0.0052
OSM SH3 local	337.9	52.9	17.08	0.0385	2.61	0.0034	0.0043
TFM NE global	315.3	1.8	27.02	28	3.00	0.0285	0.0356
TFM NS global	92.7	1.2	30.69	28	2.20	0.0003	0.0042
TFM NW global	47.6	4.4	19.67	28	2.06	0.0003	0.0032
TFM SH global	347.4	85.6	23.25	28	2.83	0.0286	0.0358
TFM ENE global	157.9	4.0	53.18	28	3.14	0.0871	0.1088
TFM EW global	186.3	4.3	34.23	28	2.85	0.0014	0.0017

Table 5: Parameters for generation of fracture sets for fracture domain FFM06, OSM-TFM alternative, Calculation Cases o3 (base case) and og3 (elevated-P_{32}). For all OSM sets r_{min} = 3 m. For all TFM sets rmin = 28 m. For all sets r_{max} = 564.2 m.

Set	Mean pole trend (°)	Mean pole plunge (°)	Fisher concen-tration κ	r_0 (m)	k_r (-)	Base case P_{32} (scaled) (m^{-1})	Elevated P_{32} (scaled) (m^{-1})
OSM NE global	125.7	10.1	45.05	0.0385	2.64	0.26800	0.1903
OSM NS global	91.0	4.1	19.49	0.0385	2.90	0.07390	0.0461
OSM NW global	34.1	0.8	16.13	0.0385	2.44	0.23280	0.1751
OSM SH global	84.3	71.3	10.78	0.0385	2.61	0.05720	0.0411
OSM ENE local	155.4	8.3	20.83	0.0385	2.20	0.04130	0.0268
OSM SH2 local	0.0	47.5	12.71	0.0385	2.61	0.03840	0.0276
TFM NE global	315.3	1.8	27.02	28	3.00	0.02851	0.0356
TFM NS global	92.7	1.2	30.69	28	2.20	0.00034	0.0042
TFM NW global	47.6	4.4	19.67	28	2.06	0.00026	0.0032
TFM SH global	347.4	85.6	23.25	28	2.83	0.02861	0.0358
TFM ENE global	157.9	4.0	53.18	28	3.14	0.08707	0.1088
TFM EW global	186.3	4.3	34.23	28	2.85	0.00138	0.0017

Table 6: Parameters for TCM (k_r-fixed model), fracture domain FFM01, Calculation Cases t2 (base case) and tg2 (elevated-P_{32}). For all sets r_{min} = 3 m and r_{max} = 564.2 m.

Set	Mean pole trend (°)	Mean pole plunge (°)	Fisher concen-tration κ	r_0 (m)	k_r (-)	Base case P_{32} (unscaled) (m^{-1})	Elevated P_{32} (unscaled) (m^{-1})
NE global	314.9	1.3	20.94	0.6592	3.02	1.7332	2.166
NS global	270.1	5.3	21.34	0.0593	2.78	1.2921	1.615
NW global	230.1	4.6	15.70	0.5937	2.85	0.9478	1.185
SH global	0.8	87.3	17.42	0.8163	2.85	0.6239	0.780
ENE local	157.5	3.1	34.11	0.3249	3.25	0.2563	0.320
EW local	0.4	11.9	13.89	0.1700	3.10	0.1686	0.211
NNE local	293.8	0.0	21.79	0.0385	3.00	0.6582	0.823
SH2 local	164.0	52.6	35.43	0.0385	2.61	0.0812	0.101
SH3 local	337.9	52.9	17.08	0.0385	2.61	0.0669	0.084

Table 7: Parameters for TCM (k_r-fixed model), fracture domain FFM06, Calculation Cases t2 (base case) and tg2 (elevated-P_{32}). For all sets r_{min} = 3 m and r_{max} = 564.2 m.

Set	Mean pole trend (°)	Mean pole plunge (°)	Fisher concen-tration κ	r_0 (m)	k_r (-)	Base case P_{32} (unscaled) (m^{-1})	Elevated P_{32} (unscaled) (m^{-1})
NE global	125.7	10.1	45.05	0.3509	3.02	3.2987	4.124
NS global	91.0	4.1	19.49	0.0385	2.78	2.1504	2.688
NW global	34.1	0.8	16.13	0.3193	2.85	1.6078	2.010
SH global	84.3	71.3	10.78	0.7929	2.85	0.6396	0.800
ENE local	155.4	8.3	20.83	0.7400	3.25	0.1940	0.243
SH2 local	0.0	47.5	12.71	0.0385	2.61	0.4294	0.536

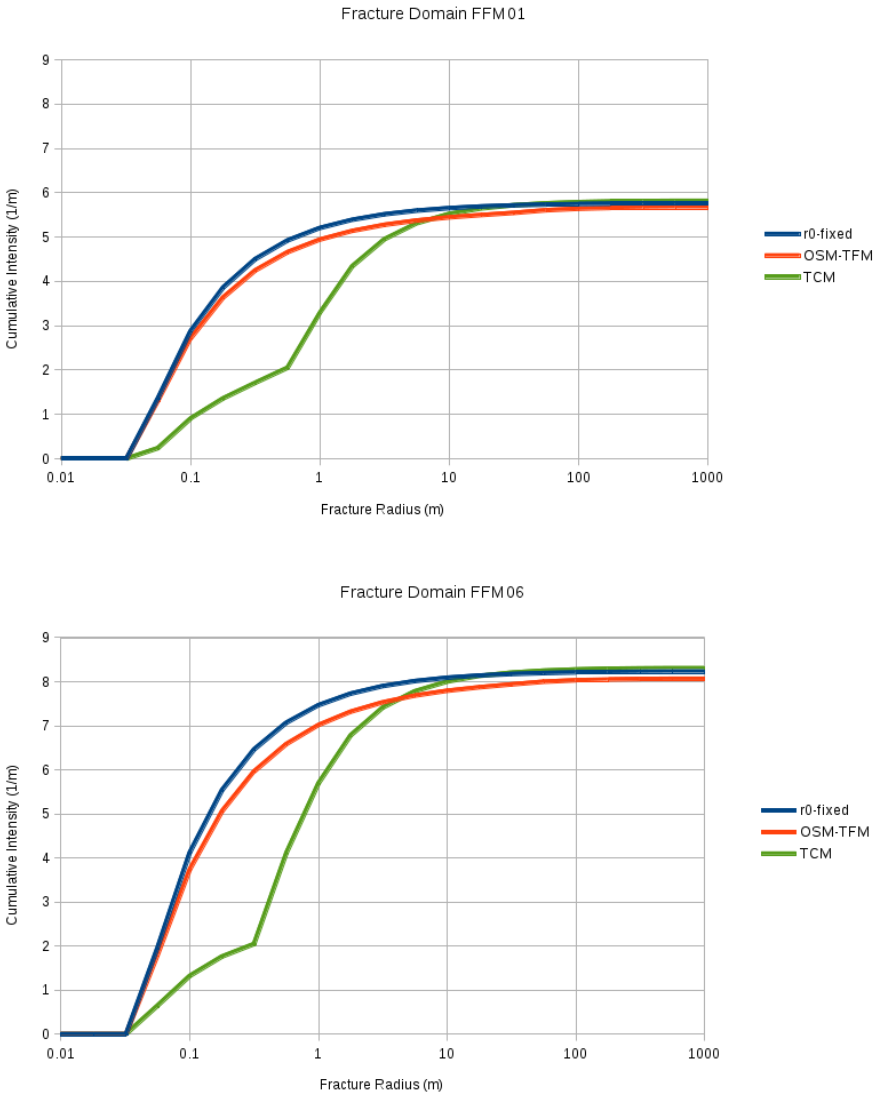

Figure 8: Fracture intensity P_{32} as a cumulative function of fracture radius for fracture domains FFM01 and FFM06. In each case the cumulative distributions are plotted for the r_0-fixed alternative, the OSM-TFM alternative, and the TCM (k_r-fixed) alternative. Only the base case is plotted for each DFN alternative. The corresponding functions for the elevated-P_{32} variants are similar but are increased by a constant multiplier of 1.25.

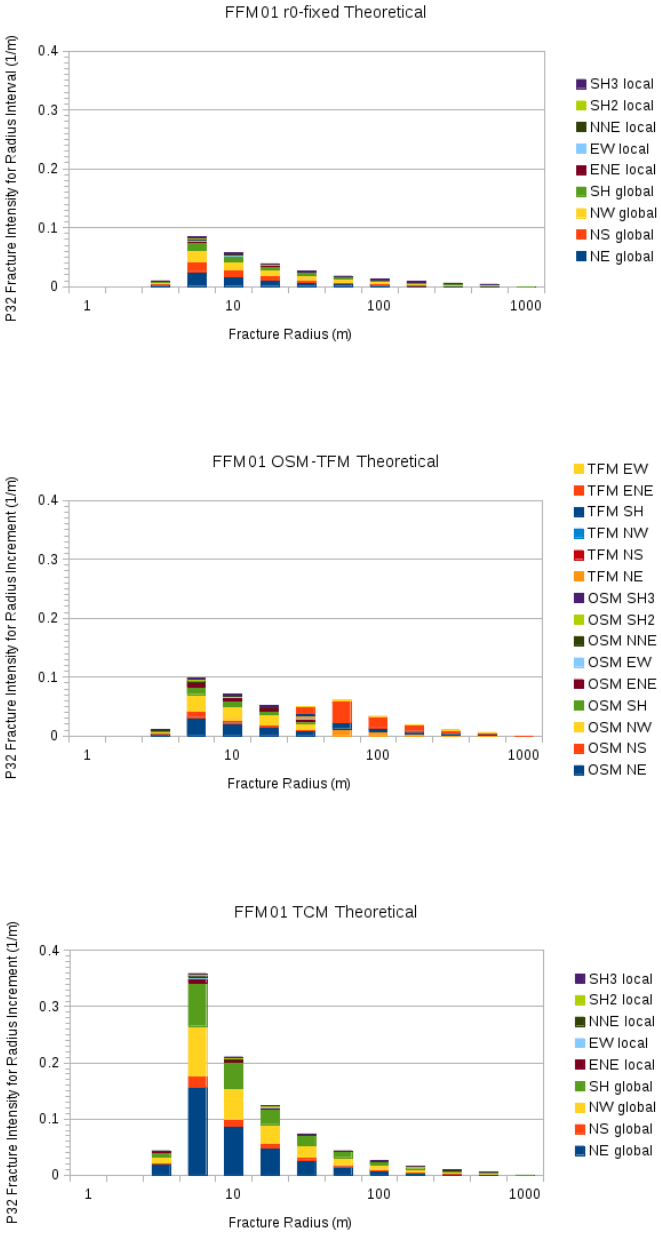

Figure 9: Fracture intensity as a function of fracture radius *r* for fracture domain FFM01, showing the contribution of each fracture set in the r_0-fixed alternative, the OSM-TFM alternative, and the TCM alternative. Each histogram bin represents an increment of one quarter order of magnitude for fracture radius. The contributions of fractures with radius smaller than 3 m are excluded from these histograms, in order to highlight the part of the fracture size distributions that can produce FPIs with deposition tunnels.

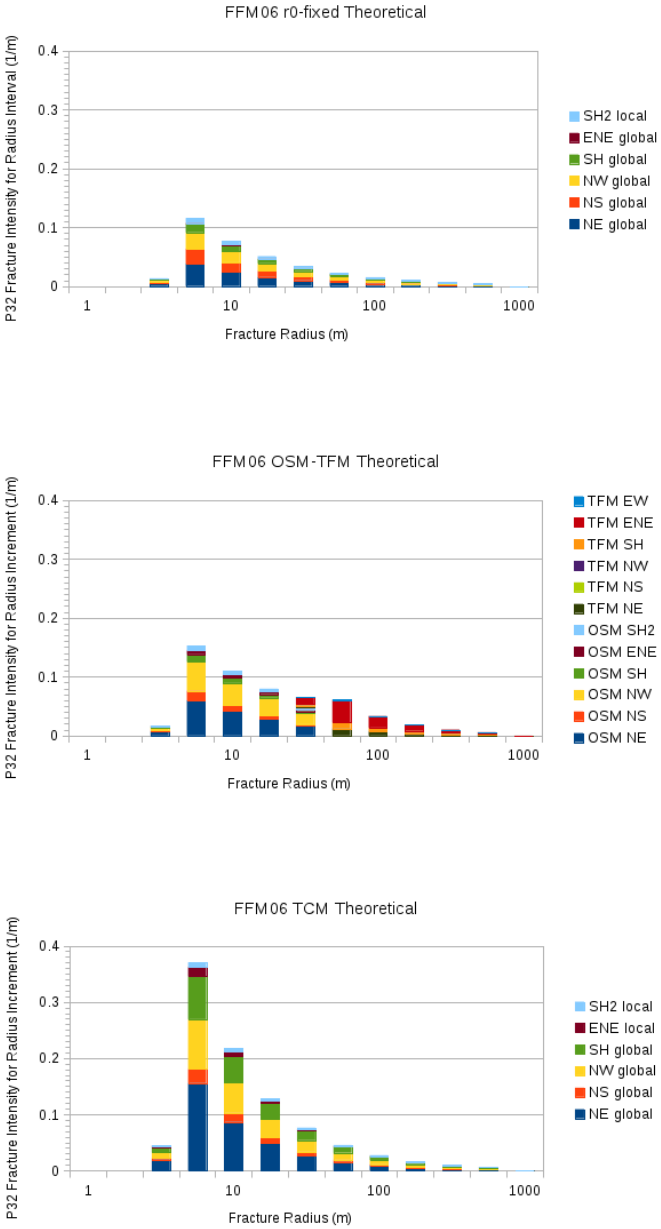

Figure 10: Fracture intensity as a function of fracture radius *r* for fracture domain FFM06, showing the contribution of each fracture set in the r_0-fixed alternative, the OSM-TFM alternative, and the TCM alternative. Each histogram bin represents an increment of one quarter order of magnitude for fracture radius. The contributions of fractures with radius smaller than 3 m are excluded from these histograms, in order to highlight the part of the fracture size distributions that can produce FPIs with deposition tunnels.

Stochastic simulation methodology

Fractures are generated by the DFM-*fracgen* module of the DFM software (*fracgen* version 2.411, March 5, 2014) by Monte Carlo simulation, for each fracture set within each fracture domain. Each of the 10 realizations for each calculation case uses a different seed (1, 2, …, 10) to initialize the pseudo-random number generator that is used to sample values from the probability distributions for each stochastic fracture property (location, radius, and orientation).

For all of the calculation cases presented here, a minimum fracture radius r_{min} = 3 m was used, so that fractures smaller than this were effectively discarded everywhere in the domain. Fractures of radius smaller than 3 m cannot form FPIs with the tunnels so they will not affect implementation of the FPC; they are also smaller than the spacing between deposition holes so they will not affect the EFPC.

Fractures are generated throughout each of the fracture domains FFM01 and FFM06, as these have been defined by SKB. However, fractures are stored for further calculations only if they have a non-zero chance of intersecting one of the tunnels in the repository. For a given fracture of radius *r*, if the minimum distance between the fracture and the nearest point in the repository area (see Figure 11) is greater than *r*, the fracture does not need to be retained and can be screened out. This reduces the number of fractures that need to be stored for simulation of the adaptive placement of deposition holes and identification of critical positions, as described in Section 2.3.2.

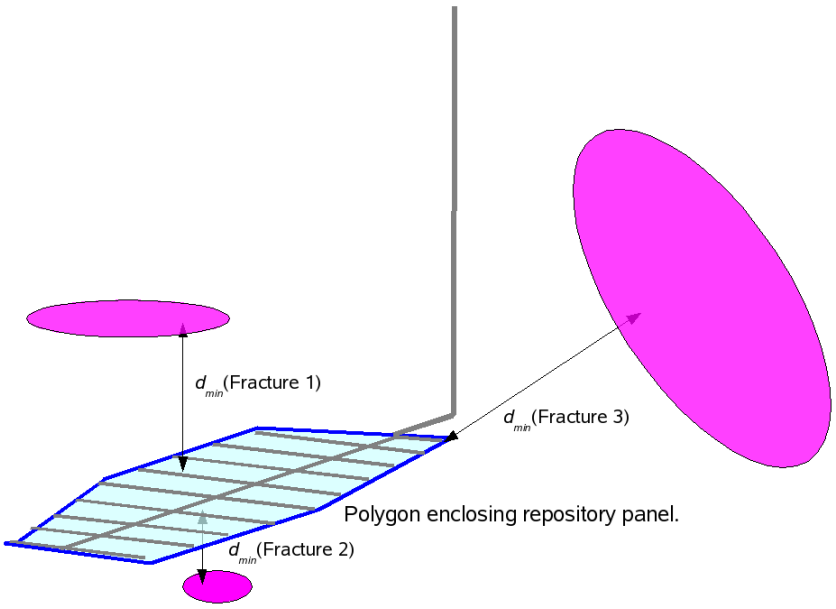

Figure 11: Schematic illustration of minimum distances from different fractures to a polygon enclosing a repository deposition panel.

In practice this screening is accomplished by using the concepts of "generation sites" and "generation shells" as defined in the DFM user documentation (Geier, 2008). For Forsmark, a single "generation site" is specified as a polygon in the plane z = -468.0 m that encloses all of the deposition tunnels in the D2 layout (SKB, 2009). The coordinates of this polygon are defined in the input file for the Forsmark Site Descriptive Model (*SDMForsmark468m.sites*, Appendix 2). The elevation z = -468.0 m is chosen so that this is approximately midway between the roof of the deposition tunnels and the bottom of the deposition holes.

A "generation shell" is the volume bounded by two surfaces, each of which is at a uniform distance from the nearest generation site (Figure 12). Fractures are associated with a given shell S_i based on the distance from the fracture to the nearest generation site. Specifically, this distance is evaluated as the minimum three-dimensional distance d_{min} from the nearest point in the generation site to the nearest point $\boldsymbol{x}$ on the fracture.

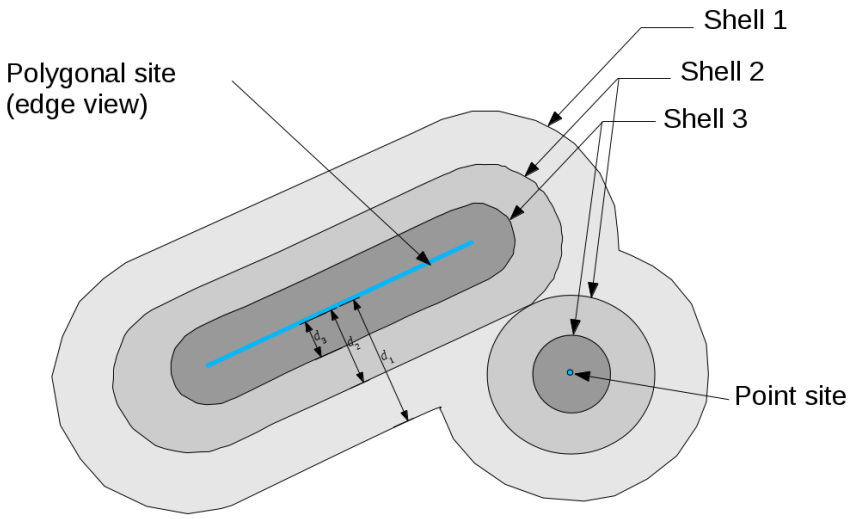

Figure 12: Concept of generation shells as used in the DFM-*fracgen* module to define volumes at a given range of distances from generation sites (either points or polygons), as indicated in blue in the figure.

A fracture is assigned to the shell S_i if:

$$d_{i-1} \geq d_{min} > d_i\,, \qquad d_0 = \infty \qquad \text{Eq. (2.11)}$$

Each shell S_i of shell radius d_i is associated with a threshold fracture size (i.e. disc radius) r_i as assigned in the generation shell file. The shell radii and corresponding values of r_i are listed in Table 8. Note that the shell radius d_1 = 50,000 m for the first shell has been chosen to be so large that any fractures with $d_{min} > d_1$ would be entirely outside the simulated fracture domains, so the threshold fracture size for this shell has no effect.

The shell radii d_i and fracture radii r_i for the smaller shells have been chosen such that any fracture that could possibly intersect any part of the repository is always retained for further calculations.

Table 8: Fracture generation shell parameters governing which fractures are retained for further calculations in the *i* th shell. These values are specified in the DFM-*fracgen* input file *Forsmark_Ncrit0.shells*.

Shell	Shell radius d_i (m)	Minimum fracture radius r_i (m)
1	50000	10000
2	500	100
3	200	50
4	100	20
5	50	10
6	10	5
7	5	2.5
8	2.5	1.5

2.3.2. Simulation of adaptive placement of deposition holes in the repository

Simulation of the adaptive placement of deposition holes in the proposed Forsmark repository is carried out for each realization of each Geo-DFN calculation case, using the DFM-*repository* module of the DFM software (*repository* version 2.411, February 17, 2014). Details of the methodology and data are described in the following paragraphs.

Repository layout

The (*X*,*Y*) coordinates of repository access tunnels and deposition tunnels are based on a version of the D2 layout. The coordinates of tunnel segments were defined based on the following delivery from SKB, as processed by Geosigma AB for SSM's hydrogeological modelling:

Date:	2010-06-02 16:27
Delivered by:	Stefan Sehlstedt
Delivered to:	Sven Tirén, Geosigma AB
Description:	Layout for the repository at Forsmark.

Another delivery was provided to SSM in 2013 for purposes of rock mechanics modelling by other consultants who required a different format. That delivery was not obtained for this task and has not been compared directly with the earlier delivery.

Tunnel axis coordinates for this analysis were taken from the layout delivery and converted to the DXF format used for DFM-*repository* module input, as documented by Geier (2010). Although the *Z* coordinates of the access and deposition tunnels were provided in this delivery, these were not used in the present analysis. Instead these tunnels are modelled as horizontal tunnels with their floors at a single nominal depth, *Z* = -465 m. The resulting tunnel layout is shown in Figure 13.

Although the 2010 data delivery was described as the D2 layout, it differs in some details from the D2 layout as shown, for example, in Figures 4-9 and 4-15 of SKB (2009). It apparently represents an earlier version of the layout which is depicted elsewhere (for example Figures 4-1 and 5-6) in the same report. The main differences, as can be seen from comparing Figure 13 with Figure 14 is that the later version includes additional deposition tunnels in the south corner and along the NE side of the repository.

SKB's calculations of N_{crit} by Munier (2010) apparently are based on the larger layout with additional tunnels, based on the canister positions reproduced previously in Figure 1. The main consequence of this larger layout, in terms of N_{crit} calculations, is that it includes a few more tunnels that are relatively close to deformation zone ZFMWNW0809A on the northeast side and to zones ZFMENE0062A, ZFMNW0123, and ZFMA2 on the south side of the repository.

The layout produced by SKB takes into account respect distances for the major deformation zones longer than 3 km (as shown in Figure 1). Smaller deformation zones (with lengths from 1 to 3 km) are accounted for in determining deposition positions by avoiding direct intersections with deposition hole positions, but are not given a respect distance.

In the present analysis, it was assumed that SKB's application of respect distances for these features in this layout has been performed correctly in the D2 Layout, so that deposition tunnels would only be located in areas that are beyond the respect distance for these structures. This assumption simplifies the calculations which are focused on the consequences of deposition-hole intersections with smaller-scale fractures as represented by the Geo-DFN model.

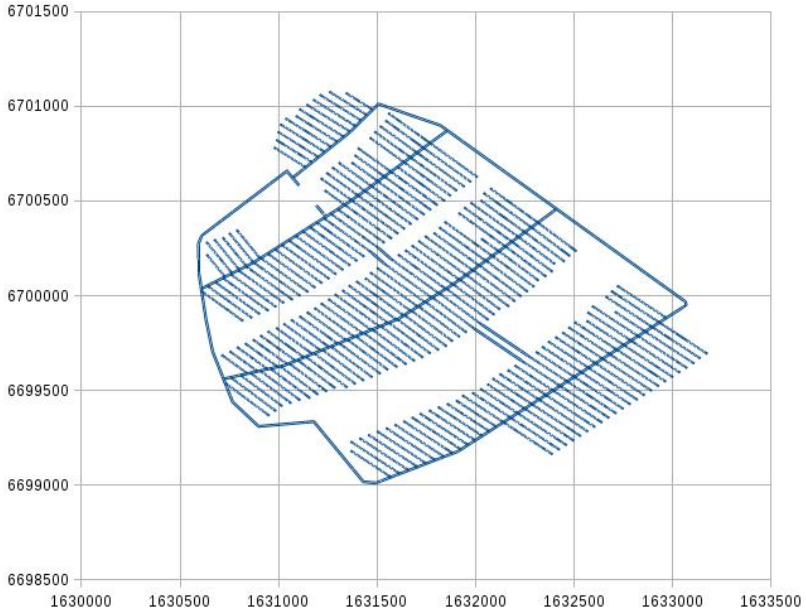

Figure 13: Horizontal section through a representative adaptation of the repository tunnels to one realization of the Geo-DFN model (r_0-fixed case), for comparison with the reference layout. Note that the central area portion of the repository, the ventilation and transport shafts, and access ramp are not included in this simulation.

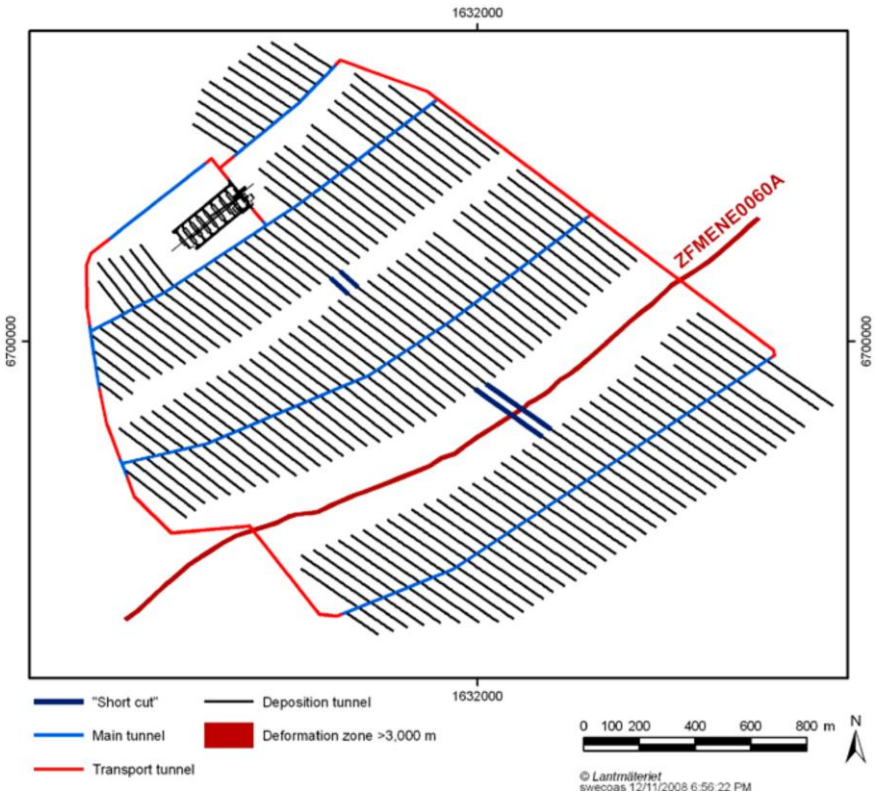

Figure 14: Plan view of deposition tunnels and access (main or transport) tunnels in the D2 layout for Forsmark, from Figure 4-9 of SKB (2009). Note that this figure contains additional deposition tunnels in the south corner of the repository, and just inside the transport tunnel on the NE side, in comparison with the earlier version of the layout which was used as the basis for simulations in the present study (as shown in the preceding figure).

Access and deposition tunnels

Coordinates of the end points of the access (main or transport) tunnels and deposition tunnels are taken from the layout data as described in the previous section. All tunnels are assumed to be horizontal with a floor elevation Z = -465 m.

The tunnels are modelled with simplified, rectangular cross sections 7 m wide by 7 m high for the access tunnels, and 4.2 m wide by 4.8 m high for the deposition tunnels. The access tunnel dimensions were based on the design specifications for SKB's SR-Can safety assessment, but are close to the 7 m × 5.8 m dimensions depicted in the "typical drawing" of a transport tunnel shown in Appendix A of SKB (2009). The results of the present study are not expected to be sensitive to access tunnel dimensions. The deposition tunnel dimensions are consistent with those used by Munier (2010, Figure 7-1) as well as with the SR-Site design report for underground openings (SKB (2010b), Figure 2-2, p. 24).

The parameters governing tunnel geometry as well as the dimensions of deposition holes and canisters are specified in the input file *SRGeoPFCv2.tunnelpars*, which is listed in Appendix 2.

Placement of deposition holes along deposition tunnels

Deposition-hole positions are chosen sequentially by the following procedure, working along one deposition tunnel at a time, and avoiding positions in which the canister or deposition hole would be intersected by FPI fractures.

First, for a given deposition tunnel, full-perimeter intersections (FPIs) are identified as the simulated fractures that cross all surfaces (top, bottom, and sides) of the tunnel. Since each fracture is modelled as a convex polygon, it is sufficient to check if a fracture intersects each of the line segments parallel to the tunnel axis, that pass through the four corners of the tunnel cross section, and with length equal to the deposition tunnel length.

Next the deposition hole positions are chosen by testing a series of trial positions (X_i,Y_i), starting from the entrance of the deposition tunnel.

The first part of length l_{plug} is avoided (see Figure 15) in order to allow room for a sealing plug. As the first deposition hole should be entirely outside of the plug space, the first trial position is located a distance $l_{plug} + r_{hole}$ from the tunnel starting point, where r_{hole} is the deposition hole radius (0.875 m based on a deposition hole diameter of 1.75 m, as indicated by SKB (2010b), Figure 2-1, p. 23).

For the present simulations, the value l_{plug} = 18.5 m is used. This takes into account the design specification of 15 m, plus an additional 3.5 m to account for half of the access tunnel width (because the deposition tunnel coordinates in the file *ForsmarkD2.tunnels* start along the axes of the access tunnels).

Each trial position *i* is tested to see if a canister positioned within a deposition hole centred at (X_i,Y_i) would be intersected by any of the FPI fractures. The canisters are considered to be of radius 0.525 m (based on SKB (2010c), Figure 4-1, p. 124 which

indicates a canister diameter of 1.050 m) and length 4.835 m (the length of the copper shell portion in SKB (2010b), Table 3-6), and located 2.75 m below the floor of the tunnel (allowing 1.25 m for the bevel dimensions as shown in SKB (2010a), Figure 5.2 plus 1.5 m for the buffer thickness above canister as indicated in SKB (2010a), Table 2-2).

If the trial position (X_i,Y_i) is acceptable based on the FPI criterion, a deposition hole is created centred on this position, with a depth of 7.833 m (consistent with SKB (2010b) Figures 2-1 and 5-2, if the bottom plate thickness is included).

The next trial position is chosen a distance $l_{spacing}$ = 6.0 m further along the tunnel. This value of $l_{spacing}$ is the design spacing between canisters for rock domain RFM029 (corresponding to fracture domain FFM01), according to Munier (2010, p. 62).

The slightly higher value of 6.8 m for rock domain RFM045 (corresponding to FFM06) is not taken into account in the present calculations, for practical reasons due to limitations of the DFM-*repository* module which allows only a single value of $l_{spacing}$ within a simulated repository. Thus even in the part of the model volume within which the Geo-DFN statistics for fracture domain FFM06 are used to generate fractures, the same value of $l_{spacing}$ = 6.0 m is used as for the rest of the model volume. Hence the utilization factors calculated here will be slightly higher than would be expected for a simulation that takes into account a larger minimum spacing in FFM06.

If the trial position (X_i,Y_i) is rejected, a new trial position is chosen by advancing a small distance l_{step} along the tunnel and repeating the tests, until an acceptable position is found.

For these calculations the value of l_{step} = 1 m is used. This is consistent with an equivalent parameter that governs stepwise testing of trial positions in the algorithm of Munier (2010, p. 44). However it should be noted that this is an artificial parameter simply for numerical modelling purposes, which may not be relevant for implementation of the FPC in a real repository. An alternative method, which is likely to be more practical underground, would be just to move however far along the tunnel is necessary to avoid an observed FPI fracture. Such an approach would also be somewhat more efficient in terms of utilization of the available space.

The sequential placement of deposition holes along a deposition tunnel terminates when the next possible position would be less than l_{end} = 15 m from the end of the drift. This is consistent with Munier (2010, Figure 4-9). According to SKB's design, this space at the end of the tunnel is needed in order to position equipment over a deposition hole.

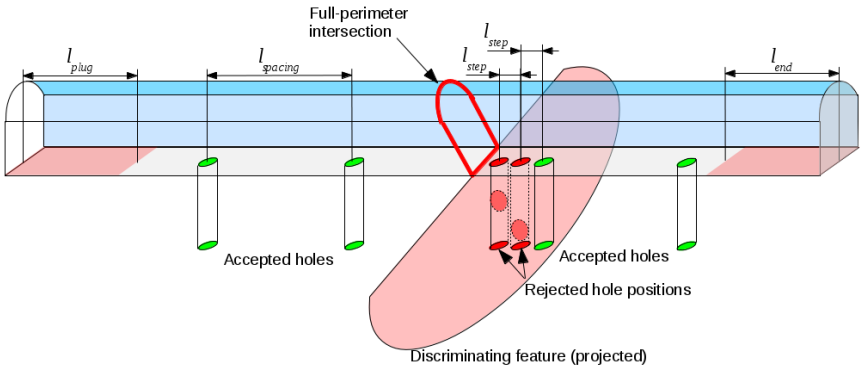

Figure 15: Schematic illustration of DFM-*repository* algorithm for simulation of sequential placement of deposition holes along a deposition tunnel.

Implementation of the full-perimeter criterion (FPC)

In the DFM-*repository* module (version 2.4.1.1) implementation of the full-perimeter criterion (FPC), as used here, a trial position is rejected if any part of a canister positioned within the hole (according to the design criteria) would be intersected by any fracture that makes an FPI with the tunnel.

This is slightly different from the way that SKB has defined the FPC. Munier (2010) rejects trial positions if any part of the canister positioned within the hole (according to the design criteria) would be intersected by the extrapolated plane of any fracture that makes an FPI with the tunnel.

The difference between SKB's implementation and the DFM-*repository* implementation is illustrated in Figure 16. SKB's implementation of the FPC is stricter, effectively treating FPI fractures as infinite. SKB's implementation will result in rejection of some deposition holes that would be accepted by the DFM-*repository* implementation, if a FPI fracture terminates just below the tunnel floor without intersecting the canister position. This difference in implementation is expected to increase the utilization factors obtained from the DFM-*repository* implementation, in comparison to what would be obtained with a more exact implementation of SKB's criterion.

However, this difference is not expected to affect the number of critical positions. The additional trial positions that are rejected by SKB's stricter implementation of the FPC are not positions in which a canister would be intersected by the FPI fractures. Rather, they represent an inefficiency in the full-perimeter criterion. Critical positions result from intersections with fractures that are not detected as FPIs in the tunnel, and thus are not excluded either by the DFM-*repository* implementation or by SKB's implementation.

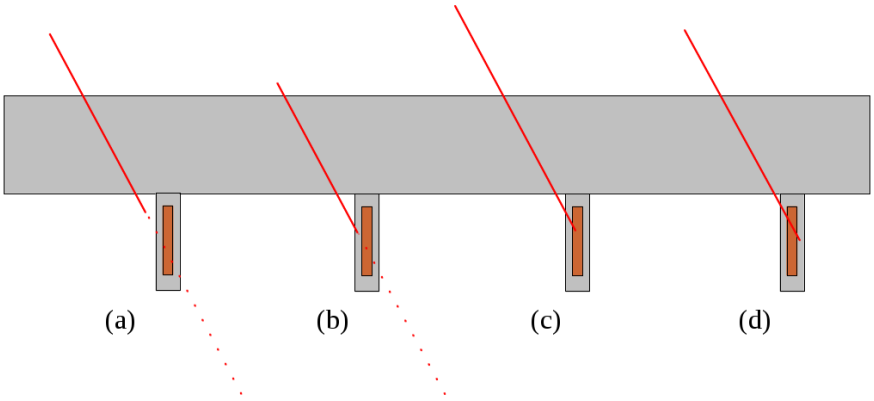

Figure 16: Comparison of DFM-*repository* (version 2.4.1.1) implementation of the FPC with SKB's implementation of the FPC as described by Munier (2010). The red lines represent the actual extent of fractures that produce FPIs with the deposition tunnel, while dotted lines represent the extrapolated planes of the fractures. The deposition holes labelled (a) and (b) would be accepted in DFM-*repository* because the fractures do not intersect the canister positions, but would be rejected in SKB's implementation because the extrapolated planes of the fractures pass through these canister positions. The deposition holes labelled (c) and (d) would be rejected both in DFM-*repository* and in SKB's implementation.

Implementation of the extended full-perimeter criterion (EFPC)

The EFPC criterion is applied based on the set of all trial positions that were accepted for a given deposition tunnel. The deposition-hole fracture mapping process is simulated by checking each intersection of a fracture with a deposition hole, to see if it would be "detectable."

If a given fracture is detectable in 5 or more deposition holes in the same tunnel, it is classified as an EFPC fracture. Any deposition holes for which an EFPC fracture cuts through any part of the canister position are rejected based on this criterion.

The calculations presented here follow Munier (2010) by regarding a fracture intersection to be detectable only if it makes a full-perimeter intersection with the deposition hole (i.e. its trace either cuts the full circumference of the deposition hole, or cuts at an angle across the top or bottom of the hole.

One difference of implementation is that Munier (2010, p. 50) suggests that fractures crossing at an angle through the bottom end of a deposition hole, such as the case depicted in Figure 4 (e), might not be detectable. In the algorithms implemented for the present study, this case is considered to be "detectable" along with the cases (a) and (b) of the same figure, in which the fracture trace makes a complete circle or ellipse on the perimeter of the deposition hole.

Thus the calculations by Munier (2010) are more conservative in assessing detectability of fractures in deposition holes. However, the number of such cases in a repository simulation is limited, as only a limited range of fracture inclinations can intersect 5 consecutive deposition holes (approximately from 0 to17 degrees), and

such a fracture can only intersect the bottom of a deposition hole if it intersects the side of the hole within about 30 cm of the bottom.

Calculation of utilization measures

The utilization percentage, or degree-of-utilization *DoU* according to the nomenclature of Munier (2010), is defined as:

$$DoU = \frac{\text{Number of accepted positions}}{\text{Planned number of positions}} \cdot 100\% \qquad \text{Eq. (2.12)}$$

The planned number of positions is considered here to be the total number of deposition holes that could ideally be located in the tunnels, taking into account the required spacing between deposition holes as well as the portion of each tunnel that is reserved for plug and end space:

$$N_{planned} = \sum_i \text{integer}\left(\frac{L_i - l_{plug} - l_{end}}{l_{spacing}}\right) \qquad \text{Eq. (2.13)}$$

where L_i is the length of the i^{th} deposition tunnel, and integer(x) denotes the largest integer that is less than or equal to a given positive number x.

2.3.3. Identification of critical fractures

"Critical fractures" are identified by the following procedure:

1) Identification of intersections between fractures and deposition holes;
2) Calculation of distances from each intersecting fracture to potentially unstable deformation zones; and
3) Comparison with the critical radii for each intersection position based on the distance to each of the potentially unstable deformation zones according to Table 1.

Upon completion of these steps, "critical fractures" are identified as fractures that intersect deposition holes which were not screened out either by the FPC alone, or by the combination of FPC and EFPC, and for which the fracture radius exceeds the critical radius for that position.

Intersections between deposition holes and fractures

Intersections between deposition holes and fractures are identified by testing for an intersection between a polygonal representation of the fracture and a right circular cylinder representing the deposition hole.

To simplify the mathematics and allow for faster calculations, the intersection test is based on whether the polygonal fracture intersects any of 8 vertical line segments along the perimeter of the cylinder. This is essentially the same approximation as

used by Munier (2010, p. 48), who judged that 8 line segments gave sufficient accuracy. In effect, this means that the comparison is made with an octagonal cylinder rather than a circular cylinder. From considerations of basic geometry, any large fracture (i.e., with radius much larger than the deposition-hole radius so that the curvature of its perimeter can be neglected) that intersects the deposition hole but is not detected by this simplified test would penetrate at most about:

$$(0.875 \text{ m}) \times [1 - \sin(45 \text{ degrees})] \approx 26 \text{ cm} \qquad \text{Eq. (2.14)}$$

into the deposition hole, which is less than the 35 cm gap between the deposition-hole perimeter and the surface of the canister.

When an intersection with the deposition hole is found, the same simplified test is also used to check if the canister position would be intersected. A large fracture missed by this simplified test could penetrate at most about 15 cm into the canister.

The coordinates of all intersections between fractures and deposition holes are calculated and recorded to a fracture intersection data (*fxd*) file for the given realization. This includes all deposition holes that are accepted based on FPC, even if they are rejected based on EFPC. The latter category is of interest because holes that would be rejected based on EFPC would still need to be backfilled, in a plausible construction sequence. Deposition holes rejected according to EFPC criterion are identified in the *fxd* file by the "RJCT" flag, while the other holes are identified by a "KEEP" flag.

The *fxd* file also records, for each intersection, the equivalent radius r of the intersecting fracture as well as the 3-D components of its normal vector (fracture pole) $\boldsymbol{n}$ and its centroid $\boldsymbol{c}$.

Calculation of distances from intersecting fractures to deformation zones

For each fracture that intersects a deposition hole, distances are calculated to each of the eight deformation zones classified that were mentioned in Section 2.1.1 of this technical note (and shown in Figure 1), classified as either having trace length L in the range 3 to 5 km, or greater than 5 km:

ZFMNW0017	$L > 5$ km
ZFMWNW0123	$L > 5$ km
ZFMNW1200	3 km $< L \leq 5$ km
ZFMWNW0809A	3 km $< L \leq 5$ km
ZFMA2	3 km $< L \leq 5$ km
ZFMENE0060A	3 km $< L \leq 5$ km
ZFMENE0062A	3 km $< L \leq 5$ km

The distances are calculated from the centroid $\boldsymbol{c}$ of a given fracture to the closest point on a given deformation zone.

For this purpose, the deformation zones are modelled as piecewise planar surfaces using the single-sided deformation zones from the Forsmark site descriptive model:

Data delivery:	May 2010.
Delivered to:	Sven Tirén, Geosigma AB
Description:	*DZ_PFM_Loc_v22_01. without boundary.dxf* and *DZ_PFM_REG_v22.02 without boundary.dxf* (files translated by Geosigma, then converted to a DFM-panel file as described in Geier, 2010).

These calculations were carried out using a simple C program developed for this specific purpose, DFM-*pancalc* (version 2.4.1.1, February 17, 2014). Distances were calculated using an existing algorithm for calculating the Cartesian distance to the nearest point in an arbitrary collection of polygons (previously developed for certain alternative DFN models in which fracture intensity depends on the distance to larger-scale features, as described by Geier, 2010).

For each fracture/deposition-hole intersection, the distance to each of the eight deformation zones is appended to the data previously recorded in the *fxd* file.

Calculation of critical radius

The critical radius r_{crit} for a given fracture-deposition hole intersection with respect to a particular deformation zone is essentially a matter of looking up the appropriate value in Table 1, based on:

- The length category of the zone (3 to 5 km or > 5 km),
- The fracture dip angle which is readily calculated as $\arccos(n_z)$ where n_z is the vertical component of $\boldsymbol{n}$, the fracture normal vector, and
- The distance from the fracture centre $\boldsymbol{c}$ to the deformation zone (as appended to the *fxd* file data).

The radial distance r_x from the fracture centre $\boldsymbol{c}$ to the point $\boldsymbol{x}$ at which the fracture plane intersects the mutual axis of the canister and the deposition hole is also calculated:

$$r_x = \|x - c\| \qquad \text{Eq. (2.15)}$$

If the fracture radius r exceeds r_{crit} for this intersection position with respect to a given zone, then an additional check is made of whether $r_x < r_{crit}'$, i.e. whether $\boldsymbol{x}$ is within the modified critical radius taking credit for the theoretical decay of slip toward the circumference of a circular fracture. The modified critical radius is calculated using Eq. (2.1).

These simple calculations and the table look-up function were implemented in a script *identify_critical_fractures.awk* (version dated January 21, 2014, Appendix 2). The ambiguity in Table 1-1 which was noted previously, regarding how to interpret the notations ">300 m" and ">>300 m" was dealt with by setting r_{crit} = 300 m in the first case, and r_{crit} = 400 m in the second case.

For each fracture/deposition-hole intersection and for each of the eight deformation zones, this script classifies the intersection to indicate the category of critical fracture:

c_{fr} (full-radius):	$r > r_{crit}$ but $r_x > r'_{crit}$
C_{rs} (reduced-slip):	$r > r_{crit}$ and $r_x < r'_{crit}$

The script also tabulates the number of fracture/deposition-hole intersections in each of these categories for which the fracture intersects the canister position, but escapes detection either using FPC, or using FPC together with EFPC.

2.3.4. Results of calculations

Fracture realizations

Figures 17 through 22 show examples of the realizations of the fracture population, for each of the calculation cases, for a 1.2 km × 1 km area within the footprint of the repository. In order to highlight the differences among the DFN alternatives for larger fractures that could conceivably act as critical fractures, fracture traces are only plotted for fractures of radius r > 7 m.

The most obvious difference is the strikingly higher intensity of fractures with r > 7 m in the TCM and OSM-TFM alternatives, compared with the r_0-fixed alternative. This is expected based on the theoretical distributions of fracture intensity as a function of r, as plotted in Figures 8 through 10.

The r_0-fixed alternative has relatively sparse fracturing but includes a relatively high proportion of very large fractures that are several hundred meters in extent. Although the number of such fractures is low in absolute terms, many of them are NW-striking and thus approximately parallel to the axes of the deposition tunnels in the D2 layout.

The OSM-TFM alternative, for fractures in the larger size ranges, is dominated by the ENE-striking set, with a secondary NE-striking set. The NW-striking and EW-striking sets are also evident but are less strongly expressed. Thus the dominant sets in this model tend to be perpendicular or oblique to the axes of the deposition tunnels.

The TCM alternative has a more isotropic pattern of large fractures, with similar intensities of fractures striking both perpendicular and parallel to the axes of the deposition tunnels. Fractures that extend several hundred meters or more are present, but are not as easy to distinguish due to the abundance of fractures with extents in the 30 to 200 m range.

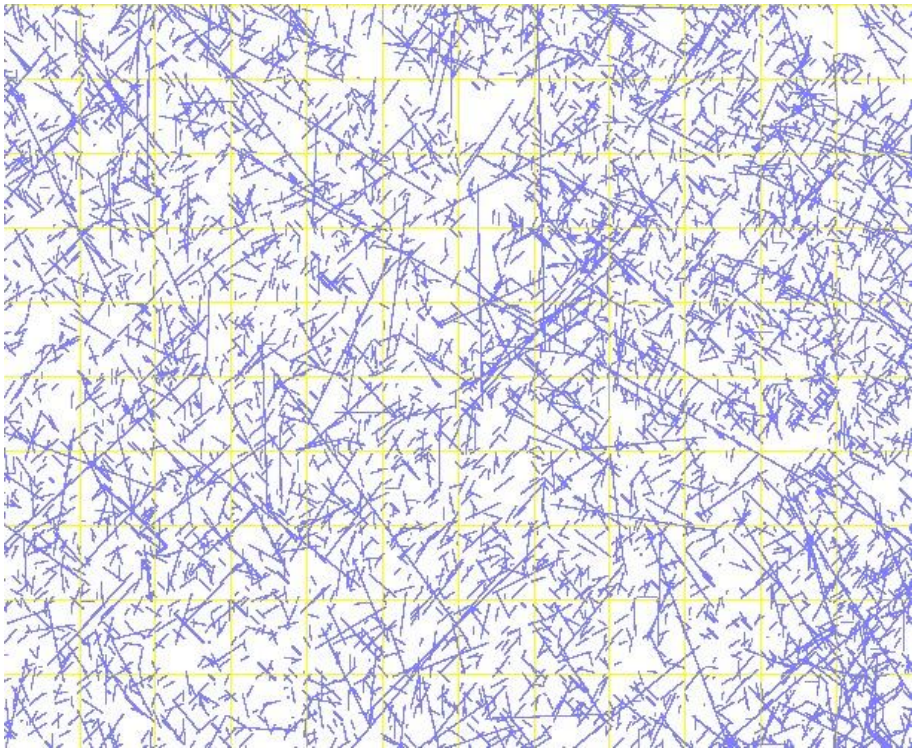

Figure 17: Fracture traces (r > 7 m) in a horizontal section at z = -465 m through one realization of the r_0-fixed base case (Calculation case r3, Realization 01). The yellow lines are aligned with the regional coordinate grid and are spaced 100 m apart in both N-S and E-W directions (RAK X = 1630800 to 1632000, RAK Y = 669600 to 6700600). North is upward.

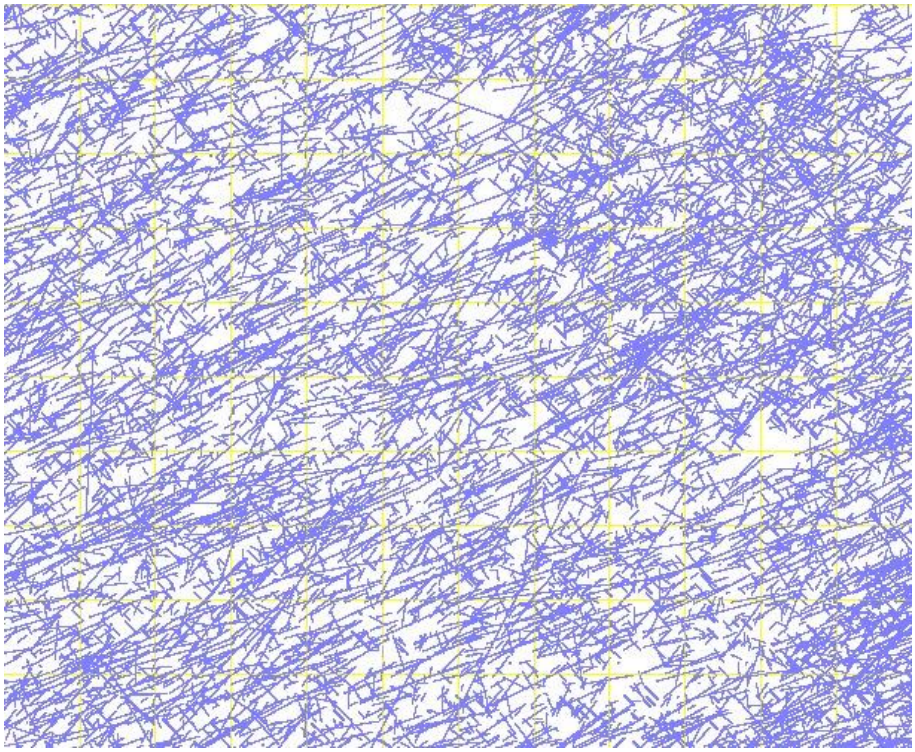

Figure 18: Fracture traces (r > 7 m) in a horizontal section at z = -465 m through one realization of the OSM-TFM base case (Calculation case o3, Realization 01). The location and orientation of the cross section and the yellow grid lines are the same as in Figure 17.

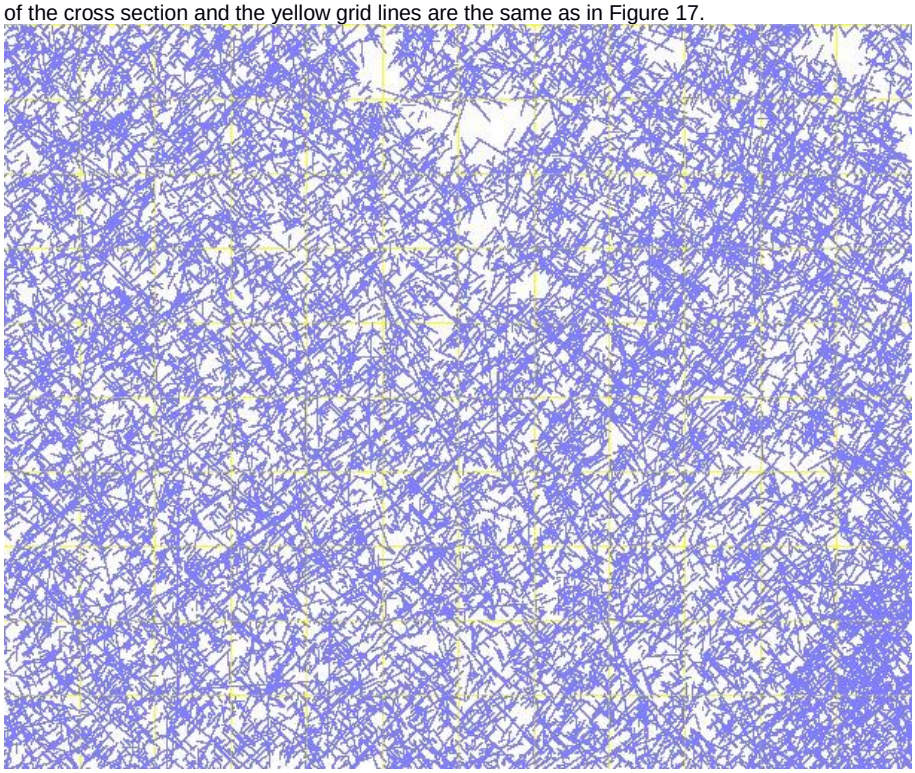

Figure 19: Fracture traces (r > 7 m) in a horizontal section at z = -465 m through one realization of the TCM base case (Calculation case t2, Realization 01). The location and orientation of the cross section and the yellow grid lines are the same as in Figure 17.

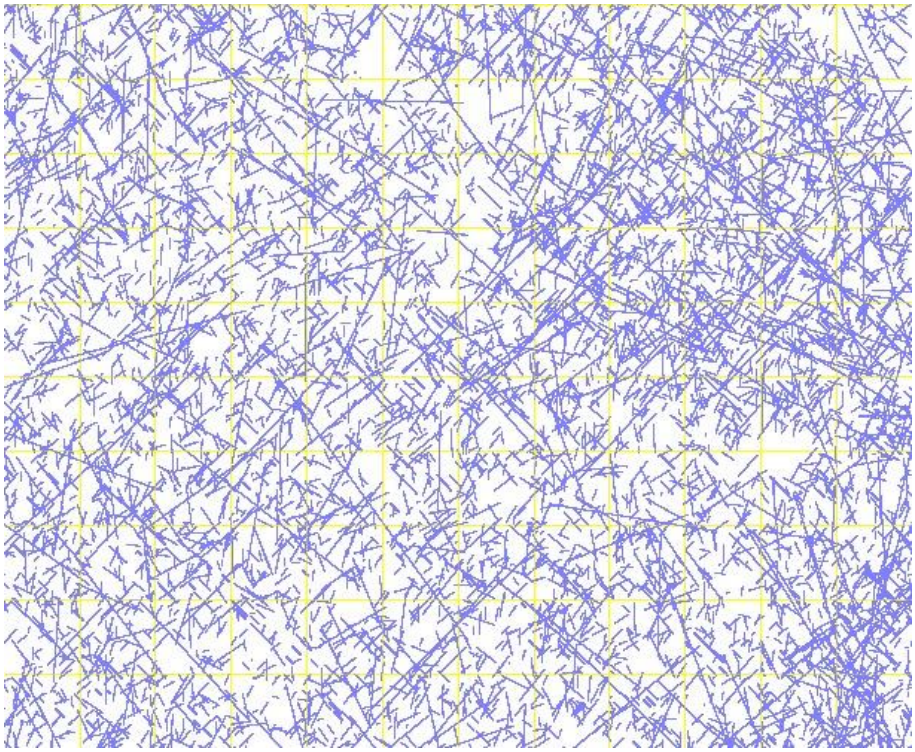

Figure 20: Fracture traces (r > 7 m) in a horizontal section at z = -465 m through one realization of the r_0-fixed, elevated-intensity variant (Calculation case rg2, Realization 01). The location and orientation of the cross section and the yellow grid lines are the same as in Figure 17.

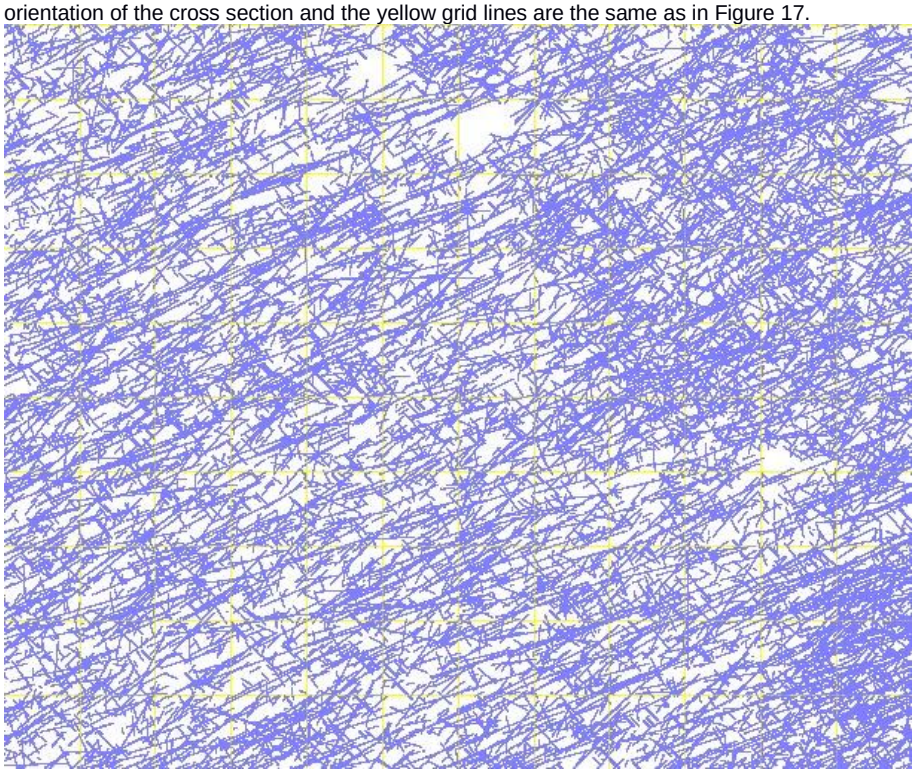

Figure 21: Fracture traces (r > 7 m) in a horizontal section at z = -465 m through one realization of the OSM-TFM elevated-intensity variant (Calculation case og3, Realization 01). The location and orientation of the cross section and the yellow grid lines are the same as in Figure 17.

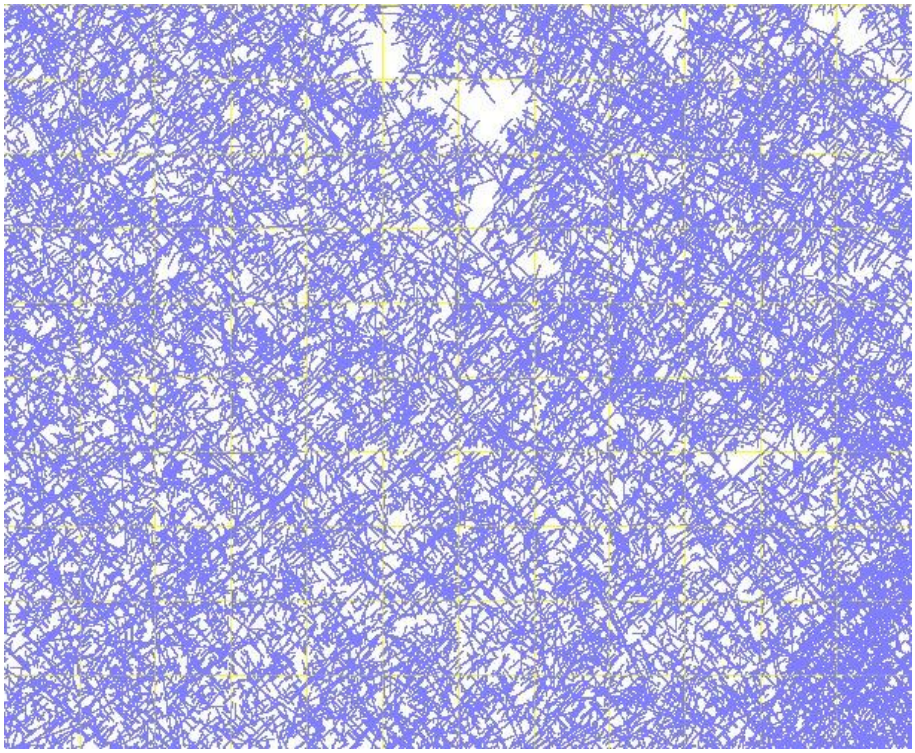

Figure 22: Fracture traces (r > 7 m) in a horizontal section at z = -465 m through one realization of the TCM elevated-intensity variant (Calculation case tg2, Realization 01). The location and orientation of the cross section and the yellow grid lines are the same as in Figure 17.

Fracture intensity as a function of fracture radius within the rock around the repository was checked based on the increments of fracture intensity $P_{32}[r_1,r_2]$ for a given range of fracture radii $[r_1,r_2]$. It is noted that the purpose of this check is simply to confirm that the model reproduces the mathematically defined distributions of the Geo-DFN models that were used by Munier (2010), rather than to confirm that SKB's models reproduce site-characterization data from boreholes.

The realizations for N_{crit} calculations use selective thinning of fractures as a function of fracture radius and distance from the repository horizon. Therefore the check of $P_{32}[r_1,r_2]$ needs to be based on the portion of the model volume within which all (or nearly all) fractures are retained. This has been done by calculating $P_{32}[r_1,r_2]$ just for the volume in the depth range -475 m < z < -460 m, within the area of a minimal polygon that contains the deposition panels in plan view (i.e. the polygon defined in the input file *SDMForsmark468m.sites*). For large fractures that extend above and/or below this depth zone, only the portion of the fracture area that lies in the depth range -475 m < z < -460 m is counted.

The results for fracture domains FFM01 and FFM06, for the base case of each of the three DFN alternative models (r_0-fixed, OSM-TFM, and TFM) are plotted in Figures 23 through 28. In each figure, the top graph shows the expected distribution while the lower two graphs give the simulated results for realizations 01 and 02, respectively. Results for the increased-P_{32} variants (not reproduced here) are similar except for the change in vertical scale to reflect the 25% increase in intensity of each set.

Fractures of $r < 3$ m have been omitted from the stochastic realizations, and the representation of fractures with radius < 10 m is likely to be affected by the discarding (for the N_{crit} calculations) of fractures in the size range from about 3 m to 10 m that cannot possibly form a full-perimeter intersection with the deposition tunnels. The plots of the theoretical distribution take into account the omission of fractures with $r < 3$ m, but do not account for the thinning of the remaining fractures depending on their radius. Therefore some differences are expected particularly for fractures of radius less than 10 m. It can be seen that, for $r \geq 10$ m, there is visually very good agreement both in terms of total fracture intensity and the fracture intensity for individual fracture sets. Very little difference is seen between the two stochastic realizations.

One difference that is difficult to see on the scale of these plots is for r approaching the maximum defined value, $r_{max} = 564.2$ m. This is a function of the discrete nature of the pseudo-random number generator that is used for Monte Carlo simulation of the fracture size distribution, in combination with the minimum radius for these calculation cases ($r_{min} = 3$ m). The pseudo-random number generator based on an algorithm given by Press et al. (1986) produces 714025 discrete values ranging from from 0 to 1. In combination with the algorithm used for generating values of r from a power-law distribution, this leads to an effective maximum radius:

$$r_{max,eff} = r_{min} \cdot exp\left[\frac{-log\left(1-\frac{1}{714025}\right)}{k_r}\right] \qquad \text{Eq. (2.16)}$$

which varies from about 270 to 558 m depending on the value of k_r for a given fracture set. Stochastic effects also become more pronounced for fractures approaching the maximum radius.

An additional check of the generated fracture orientations for each fracture set (Appendix 3) produced good agreement with the specified distributions.

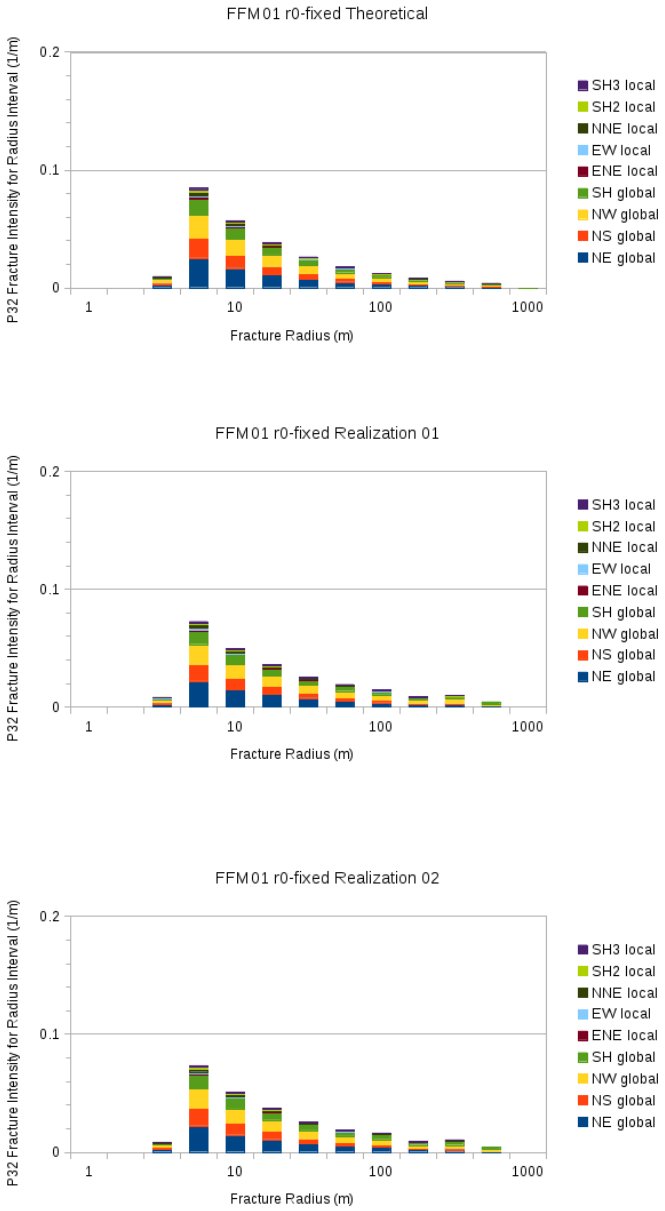

Figure 23: Comparison of theoretical (top plot) and simulated (bottom two plots) increments of P_{32} fracture intensity for each of the fracture sets in fracture domain FFM01, r_0-fixed alternative. The two lower plots represent two different realizations (01 and 02). The bars represent $P_{32}[r_1,r_2]$ for increments of a quarter order of magnitude in fracture radius.

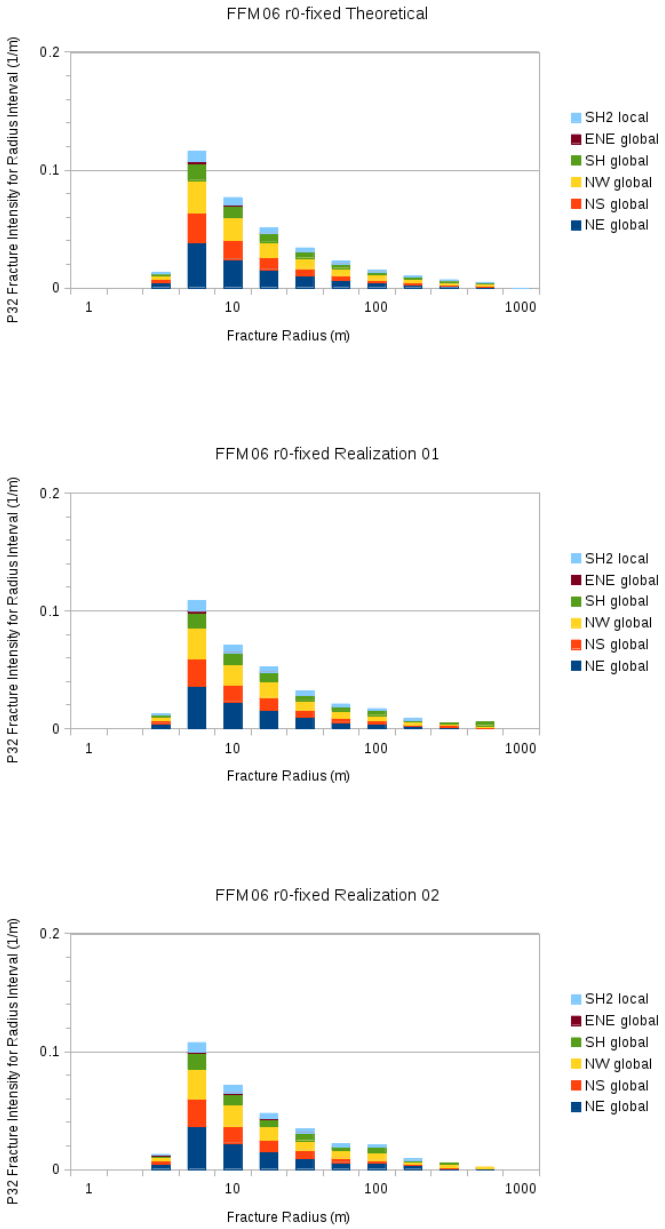

Figure 24: Comparison of theoretical (top plot) and simulated (bottom two plots) increments of P_{32} fracture intensity for each of the fracture sets in fracture domain FFM06, r_0-fixed alternative. The two lower plots represent two different realizations (01 and 02). The bars represent $P_{32}[r_1,r_2]$ for increments of a quarter order of magnitude in fracture radius.

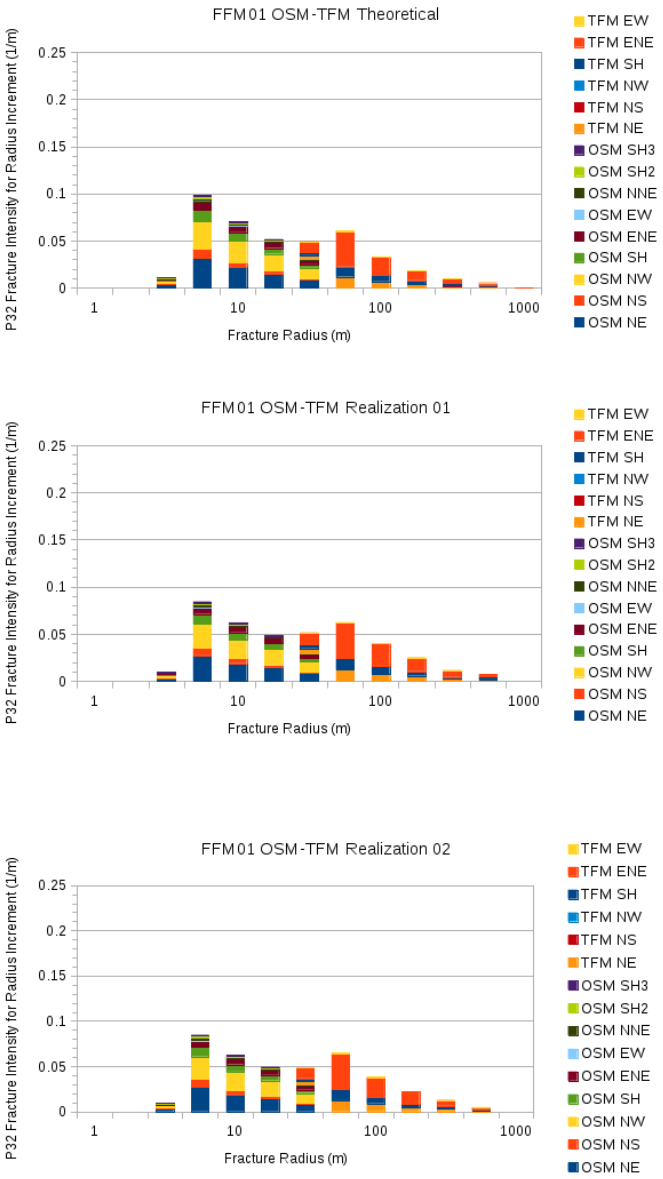

Figure 25: Comparison of theoretical (top plot) and simulated (bottom two plots) increments of P_{32} fracture intensity for each of the fracture sets in fracture domain FFM01, OSM-TFM alternative. The two lower plots represent two different realizations (01 and 02). The bars represent $P_{32}[r_1,r_2]$ for increments of a quarter order of magnitude in fracture radius.

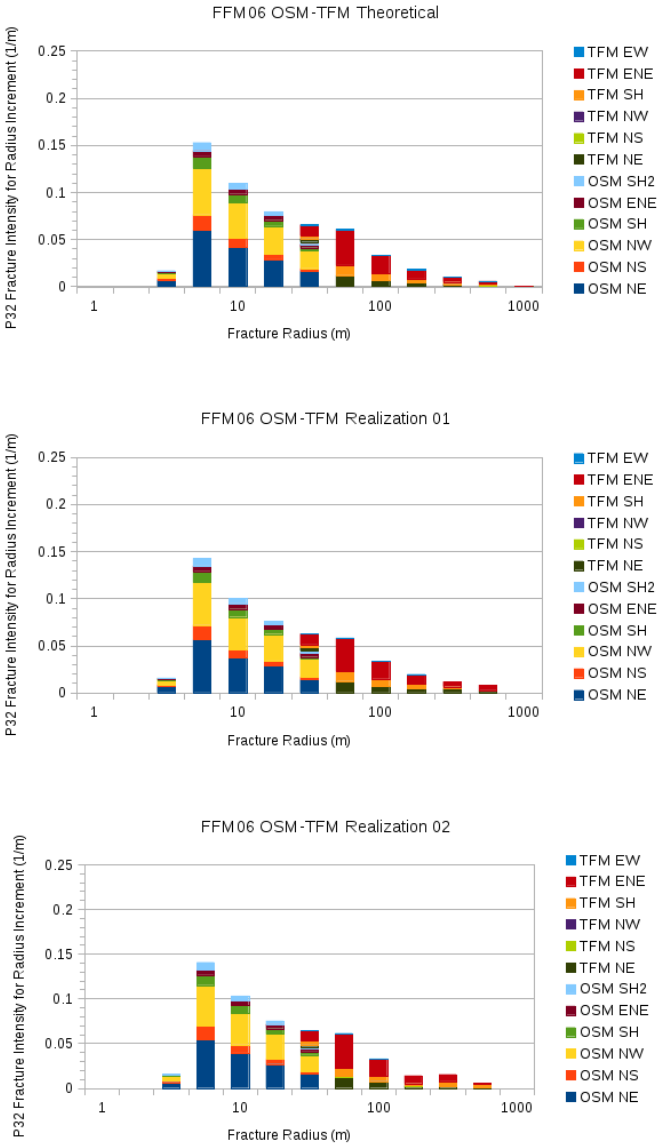

Figure 26: Comparison of theoretical (top plot) and simulated (bottom two plots) increments of P_{32} fracture intensity for each of the fracture sets in fracture domain FFM06, OSM-TFM alternative. The two lower plots represent two different realizations (01 and 02). The bars represent $P_{32}[r_1,r_2]$ for increments of a quarter order of magnitude in fracture radius.

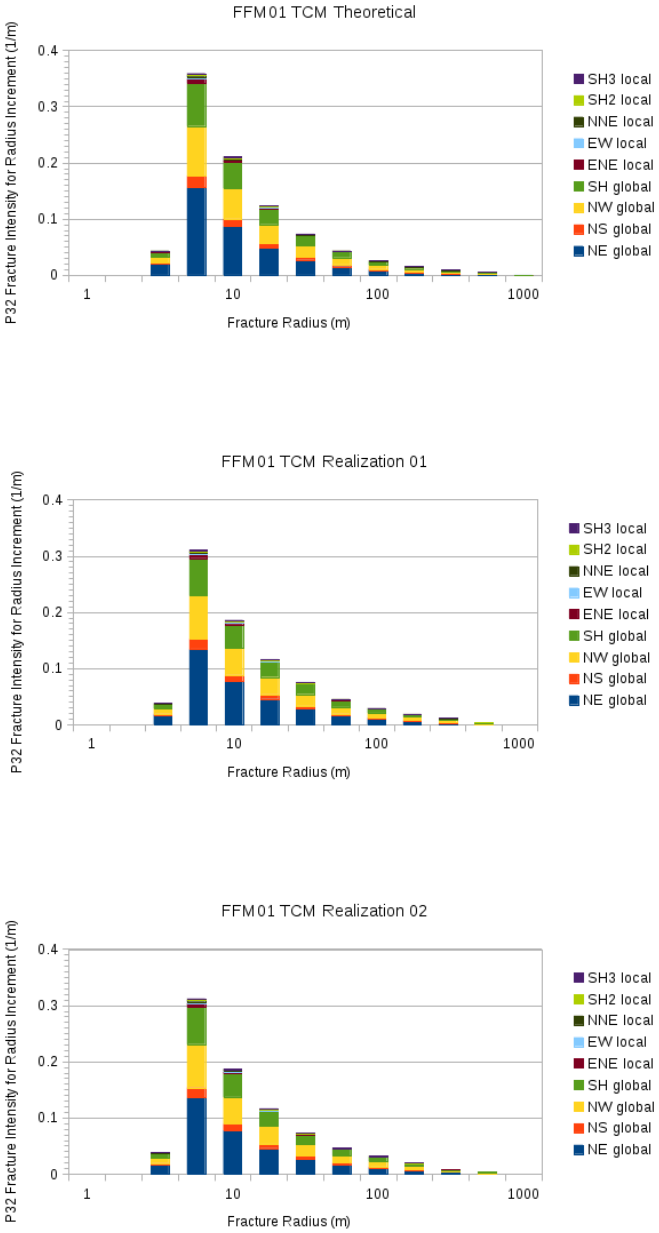

Figure 27: Comparison of theoretical (top plot) and simulated (bottom two plots) increments of P_{32} fracture intensity for each of the fracture sets in fracture domain FFM01, TCM alternative. The two lower plots represent two different realizations (01 and 02). The bars represent $P_{32}[r_1,r_2]$ for increments of a quarter order of magnitude in fracture radius.

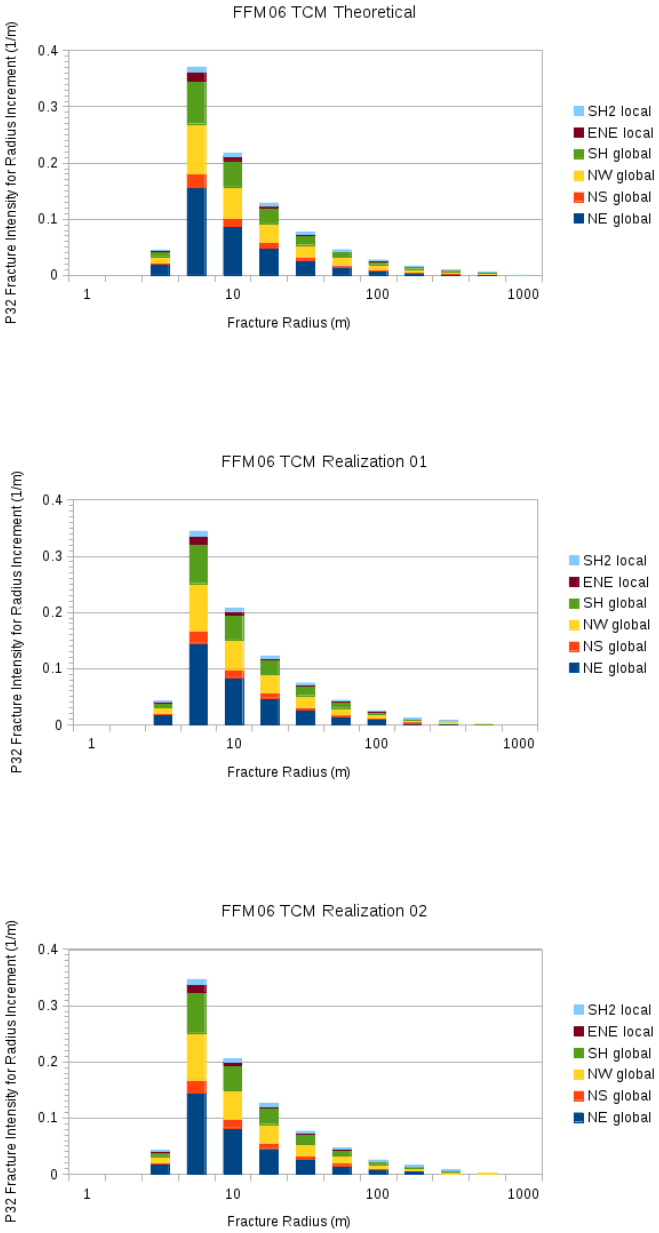

Figure 28: Comparison of theoretical (top plot) and simulated (bottom two plots) increments of P_{32} fracture intensity for each of the fracture sets in fracture domain FFM06, TCM alternative. The two lower plots represent two different realizations (01 and 02). The bars represent $P_{32}[r_1,r_2]$ for increments of a quarter order of magnitude in fracture radius.

Adapted repository layouts and utilization factors

The numbers of canister positions rejected due to FPC and EFPC are shown respectively in Figures 29 and 30.

Calculation of the number canister positions rejected based on FPC is not straightforward. The number of trial positions rejected based on FPC is a function of the step length l_{step} that is used in the simulation of the placement of deposition holes along deposition tunnels. For smaller values of l_{step} there is increasing likelihood that a single FPI fracture will lead to rejection of multiple trial positions, especially for moderately to gently dipping fractures.

Here for the purpose of presentation in Figure 29, when a series of consecutive trial positions in a given deposition tunnel are rejected, these are counted as just one single rejected canister position. This yields a more representative measure of the effect of the FPC on utilization of the available space, versus counting every rejected trial position. However, the relationship to degree-of-utilization is not direct, so this plot should be seen as illustrative rather than strictly quantitative.

In contrast, the count of EFPC rejections as shown in Figure 30 is directly related to utilization. Each EFPC rejection represents a deposition hole that, in an actual repository, would need to be bored before the decision to reject the hole. Such holes would then need to be backfilled, in a plausible construction sequence.

In terms of both measures, the r_0-fixed alternative yields a prediction of significantly fewer rejected canister positions in comparison to the OSM-TFM and TCM alternatives. The effect of a uniform 25% increase in fracture intensity (as indicated by comparing calculation case rg2 vs. r3, og3 vs. o3, and tg2 vs. t2) is comparatively minor.

In terms of FPC rejections the OSM-TFM and TCM alternatives are similar, with significantly less difference between these two alternatives than the effect of a 25% increase in fracture intensity.

Both variants of the TCM produce higher numbers of EFPC rejections than the corresponding variants of the OSM-TFM alternative. The difference between these two alternatives for EFPC rejections is similar in magnitude to the effect of a 25% increase in fracture intensity for either alternative.

A statistical summary of degree-of-utilization *DoU* for the different calculation cases is given in Table 9, and plotted in Figure 31. As discussed previously, the utilization factors obtained from this model are expected to be somewhat higher than would be obtained with a more exact implementation of SKB's criterion for rejecting deposition hole positions based on projected (rather than actual) intersections of FPIs with canister positions.

The r_0-fixed model (base case) yields significantly higher degrees of utilization than either of the other two Geo-DFN models. A 25% increase in P_{32}, in the elevated-intensity variants, results in a decrease of 2.6% to 4.1% in *DoU*. Thus this amount of increase in P_{32} has a minor effect in comparison with the difference of up to 8.3% between different Geo-DFN alternatives (in the base case).

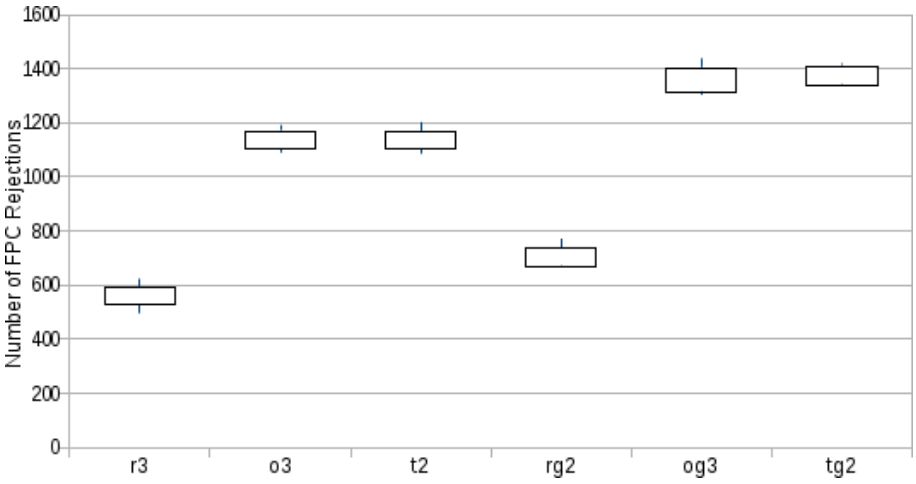

Figure 29: Numbers of positions excluded due to the full-perimeter criterion (FPC) for each of the six calculation cases: (r3) r_0-fixed base case, (o3) OSM-TFM base case, (t2) TCM base case, (rg2) r_0-fixed elevated P_{32} variant, (og3) OSM-TFM elevated P_{32} variant, (tg2) TCM elevated P_{32} variant. Bars show ranges of mean ± one standard deviation; whiskers show ranges from minimum to maximum values.

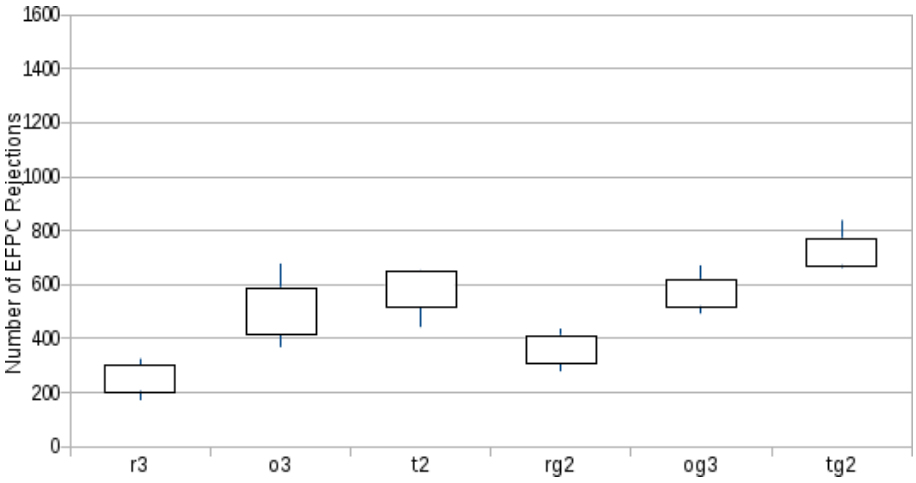

Figure 30: Numbers of positions excluded due to the extended full-perimeter criterion (EFPC) for each of the six calculation cases: (r3) r_0-fixed base case, (o3) OSM-TFM base case, (t2) TCM base case, (rg2) r_0-fixed elevated P_{32} variant, (og3) OSM-TFM elevated P_{32} variant, (tg2) TCM elevated P_{32} variant. Bars show ranges of mean ± one standard deviation; whiskers show ranges from minimum to maximum values.

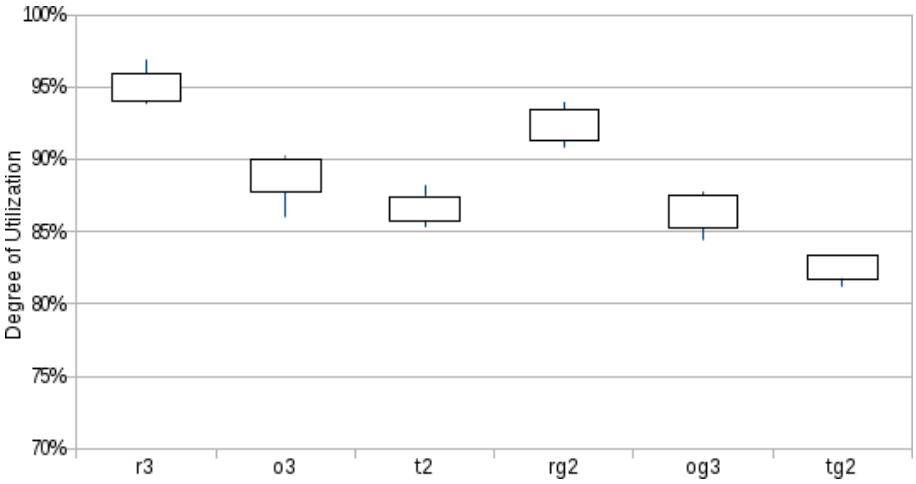

Figure 31: Degree-of-utilization *DoU* when using both FPC and EFPC for each of the six calculation cases: (r3) r_0-fixed base case, (o3) OSM-TFM base case, (t2) TCM base case, (rg2) r_0-fixed elevated P_{32} variant, (og3) OSM-TFM elevated P_{32} variant, (tg2) TCM elevated P_{32} variant. Bars show ranges of mean ± one standard deviation; whiskers show ranges from minimum to maximum values.

Table 9: Statistical summary of degree-of-utilization percentages *DoU* when using both FPC and EFPC for the six calculation cases.

Case	Mean (%)	Std. Dev. (%)	Minimum (%)	Maximum (%)
r_0-fixed base (r3)	94.9	0.9	93.8	95.9
OSM-TFM base (o3)	88.9	1.2	86.0	90.2
TCM base (t2)	86.6	0.9	85.3	88.2
r_0-fixed elevated (rg2)	92.3	1.0	90.8	94.0
OSM-TFM elevated (og3)	86.3	1.1	84.4	87.8
TCM elevated (tg2)	82.5	0.8	81.2	83.3

Numbers of critical fractures per repository with FPC + EFPC

The average numbers of critical fractures per full repository that escape either the FPC alone, or the combined FPC and EFPC, for each of the two categories:

$$\begin{array}{lll} c_{fr}: & r > r_{crit} \text{ but } r_x > r'_{crit} & \text{(full-radius)} \\ C_{rs}: & r > r_{crit} \text{ and } r_x < r'_{crit} & \text{(reduced-slip)} \end{array} \qquad \text{Eq. (2.17)}$$

with respect to each of the seven deformation zones considered, are presented in Tables 10 through 13.

The use of the EFPC in addition to FPC reduces the number of critical fractures in the first category by roughly a factor of 4 to 5. Taking credit for the theoretical reduction in slip near the edges of a circular fracture reduces the number of critical fractures even further (up to a factor of 20 in some cases).

The two calculation cases based on the OSM-TFM alternative give generally higher numbers of critical fractures than variants based on the r_0-fixed and TCM alternatives. The effect of increasing fracture intensity by 25% for either the r_0-fixed or TCM alternative is comparatively slight.

This suggests that uncertainty regarding the details of the fracture size distribution is more important than overall fracture intensity. The main factor that distinguishes the OSM-TFM alternative from the other two alternatives is a relatively high intensity of fractures with radius in the range 50 to 100 m.

In Table 13, the number of critical positions (if added over all of the deformation zones considered for a given Geo-DFN alternative) generally increases when P_{32} increases. However, close inspection of the numbers shows that the number of critical positions for specific fracture zones can sometimes show a slight decrease, for a given Geo-DFN alternative. For the r_0-fixed alternative, this occurs for ZFMENE0060A. For the TCM alternative, this occurs for ZFMENE0062A, ZFMNW1200, ZFMWNW0123, and ZFMA2. For three of these cases the decrease is only 0.1 critical fractures per realization (1 fracture in the 10 realizations). For the other two cases the decrease is just 0.3 critical fractures per realization.

This is believed to be an artefact of stochastic effects in combination with and the limited number of realizations. In some cases, a canister position that would be intersected by a critical fracture in a lower P_{32} realization might be excluded based on an FPI formed by one of the additional fractures that turns out to intersect the same canister position. So although utilization is consistently reduced when P_{32} increases, a few critical positions could be eliminated as a matter of chance.

Table 10: Average number of critical canister positions per repository simulation that escape the FPC and are in the full-radius category c_{fr}: ($r > r_{crit}$ but $r_x > r'_{crit}$) with respect to each of the deformation zones considered, for each of the six calculation cases. Ten realizations were completed for each calculation case.

Calculation case	ZFM ENE 0060A	ZFM ENE 0062A	ZFM NW 0017	ZFM NW 1200	ZFM WNW 0123	ZFM WNW 0809A	ZFM A2
r_0-fixed base (r3)	24.3	12.9	17.1	11.8	21.7	11.0	17.9
OSM-TFM base (o3)	77.1	61.6	65.3	59.5	79.0	54.3	71.9
TCM base (t2)	36.8	16.7	24.7	8.4	31.8	11.6	25.4
r_0-fixed elevated (rg2)	64.9	39.8	57.7	24.7	60.7	27.5	50.3
OSM-TFM elevated (og3)	58.6	26.1	38.6	19.5	54.7	24.3	36.7
TCM elevated (tg2)	54.7	21.3	39.7	19.7	49.4	25.7	31.4

Table 11: Average number of critical canister positions per repository simulation that escape the FPC and are in the reduced-slip category C_{rs}: ($r > r_{crit}$ and $r_x < r'_{crit}$) with respect to each of the deformation zones considered, for each of the six calculation cases. Ten realizations were completed for each calculation case.

Calculation case	ZFM ENE 0060A	ZFM ENE 0062A	ZFM NW 0017	ZFM NW 1200	ZFM WNW 0123	ZFM WNW 0809A	ZFM A2
r_0-fixed base (r3)	13.1	4.4	8.4	6.5	10.5	3.3	7.1
OSM-TFM base (o3)	43.1	17.3	25.2	13.3	34.8	11.0	32.7
TCM base (t2)	15.1	4.7	1.4	0.7	6.6	0.7	6.3
r_0-fixed elevated (rg2)	33.6	13.5	22.8	11.1	27.1	11.9	23.8
OSM-TFM elevated (og3)	31.6	11.8	16.4	9.0	27.0	12.6	17.9
TCM elevated (tg2)	27.1	5.1	7.8	1.9	14.5	4.5	7.9

Table 12: Average number of critical canister positions per repository simulation that escape both FPC and EFPC, and are in the full-radius category c_{fr}: ($r > r_{crit}$ but $r_x > r'_{crit}$) with respect to each of the deformation zones considered, for each of the six calculation cases. Ten realizations were completed for each calculation case.

Calculation case	ZFM ENE 0060A	ZFM ENE 0062A	ZFM NW 0017	ZFM NW 1200	ZFM WNW 0123	ZFM WNW 0809A	ZFM A2
r_0-fixed base (r3)	9.2	4.7	5.5	3.4	6.1	3.7	5.5
OSM-TFM base (o3)	14.1	7.2	8.2	6.3	11.3	5.7	7.9
TCM base (t2)	12.3	5.4	6.6	2.8	10.1	3.3	6.4
r_0-fixed elevated (rg2)	12.2	5.9	9.2	3.3	9.7	4.2	7.6
OSM-TFM elevated (og3)	20.8	9.6	12.6	8.4	15.7	6.7	12.3
TCM elevated (tg2)	13.8	5.4	7.2	4.0	9.9	5.5	6.6

Table 13: Average number of critical canister positions per repository simulation that escape both FPC and EFPC, and are in the reduced-slip category C_{rs}: ($r > r_{crit}$ and $r_x < r'_{crit}$) with respect to each of the deformation zones considered, for each of the six calculation cases. Ten realizations were completed for each calculation case.

Calculation case	ZFM ENE 0060A	ZFM ENE 0062A	ZFM NW 0017	ZFM NW 1200	ZFM WNW 0123	ZFM WNW 0809A	ZFM A2
r_0-fixed base (r3)	4.1	1.0	1.4	0.8	1.6	0.7	1.7
OSM-TFM base (o3)	5.6	1.2	2.1	1.3	2.6	1.0	2.2
TCM base (t2)	3.5	1.0	0.3	0.3	1.3	0.1	0.8
r_0-fixed elevated (rg2)	3.8	1.1	2.0	1.1	2.2	1.3	2.1
OSM-TFM elevated (og3)	8.3	3.3	3.4	2.7	5.4	2.2	3.6
TCM elevated (tg2)	3.6	0.7	0.4	0.2	1.2	0.7	0.7

Examples of critical fractures

Figure 32 shows the deposition-hole positions that are accepted based on the FPC but are intersected by fractures, for Realization 01 of the r_0-fixed model, base case. The categories of intersected positions are distinguished by colour to show if they are accepted or rejected based on the EFPC, and whether they are classed as non-critical intersections or as one of the two classes of critical intersections (c_{fr} = full radius or C_{rs} = reduced-slip) for at least one of the deformation zones.

Four fractures in this realization result in critical positions with respect to at least one of the deformation zones near the repository that SKB judges to be potentially unstable. These are listed in Table 14 and indicated by arrows in Figure 32.

The first three of these critical fractures, and the affected tunnels, are plotted on a more detailed scale as orthogonal views in Figures 33 through 35. All three of these fractures intersect additional tunnels in which they produce FPIs with the tunnel, and thus could be avoided based on the FPC.

All three of these fractures are missed in the deposition tunnels where they produce critical intersections because, although they intersect the floors of these deposition tunnels, these intersections are near the ends of the tunnels and do not intersect the tunnel roofs.

The first example (Fracture 148332) intersects the blind end of tunnel 86, so would not be detected in an access tunnel, but it is detected as an FPI in several neighbouring deposition tunnels. The second and third examples (Fractures 281810 and 186696) intersect the plug ends of two of the tunnels indicated in the table. Hence they would also likely be detected as FPIs if mapping is extended into the main tunnels. Fracture 281810 also produces a series of critical intersections with three deposition holes near the blind end of a tunnel on the opposite side of the access tunnel, but these are rejected based on the EFPC.

The fourth fracture listed in Table 14 (Fracture 218294, not plotted on a detailed scale) intersects the plug end of the deposition tunnel in the floor, but not in the roof. It would be detected as an FPI in at least eight of the neighbouring deposition tunnels, as well as in the access tunnel.

One other fracture (Fracture ID 171786, not presented either in Table 14 or in Figure 32) produces seven consecutive critical intersections in Tunnel 215 that are critical with respect to ZFMENE0060A. However all of these positions would be rejected based on the EFPC. Hence Fracture 171786 is successfully avoided by use of the EFPC.

Table 14: The four fractures and deposition hole positions that produce critical intersections in Realization 01 of the r_0-fixed base case (r3). Note that the first accepted canister position in each tunnel has the number zero rather than one. Critical canister positions that would be rejected based on the EFPC are shown in gray font (rather than black). Critical canister positions that would be accepted based on the EFPC and are in the critical reduced-slip category C_{rs} ($r > r_{crit}$ and $r_x < r'_{crit}$) with respect to at least one of the deformation zones considered are highlighted in bold font.

Fracture ID	Tunnel	Canister Position	EFPC reject?	ZFM ENE 0060A	ZFM ENE 0062A	ZFM NW 0017	ZFM NW 1200	ZFM WNW 0123	ZFM WNW 0809A	ZFM A2
148332	**86**	**41**	**N**	c_{fr}	c_{fr}	**C_{rs}**	c_{fr}	**C_{rs}**	**C_{rs}**	c_{fr}
281810	155	33	Y	c_{fr}	c_{fr}	c_{fr}	c_{fr}	c_{fr}	c_{fr}	c_{fr}
281810	155	34	Y	c_{fr}	c_{fr}	c_{fr}	c_{fr}	c_{fr}	c_{fr}	c_{fr}
281810	155	35	Y	c_{fr}	c_{fr}	c_{fr}	c_{fr}	c_{fr}	c_{fr}	c_{fr}
281810	167	0	N	c_{fr}	c_{fr}	c_{fr}	c_{fr}	c_{fr}	c_{fr}	c_{fr}
281810	167	1	N	c_{fr}	c_{fr}	c_{fr}	c_{fr}	c_{fr}	c_{fr}	c_{fr}
281810	167	2	N	c_{fr}	c_{fr}	c_{fr}	c_{fr}	c_{fr}	c_{fr}	c_{fr}
186696	**183**	**0**	**N**	**C_{rs}**	c_{fr}	c_{fr}	c_{fr}	c_{fr}	c_{fr}	**C_{rs}**
186696	**183**	**1**	**N**	**C_{rs}**	c_{fr}	c_{fr}	c_{fr}	c_{fr}	c_{fr}	**C_{rs}**
186696	**183**	**2**	**N**	**C_{rs}**	c_{fr}	c_{fr}	c_{fr}	c_{fr}	c_{fr}	**C_{rs}**
186696	**184**	**1**	**N**	**C_{rs}**	**C_{rs}**	**C_{rs}**	c_{fr}	**C_{rs}**	c_{fr}	**C_{rs}**
186696	**184**	**2**	**N**	**C_{rs}**	**C_{rs}**	**C_{rs}**	c_{fr}	**C_{rs}**	c_{fr}	**C_{rs}**
186696	185	2	Y	C_{rs}	C_{rs}	C_{rs}	c_{fr}	C_{rs}	c_{fr}	C_{rs}
186696	185	3	Y	C_{rs}	C_{rs}	C_{rs}	c_{fr}	C_{rs}	c_{fr}	C_{rs}
218294	**196**	**0**	**N**	**C_{rs}**	**c_{fr}**	**c_{fr}**		**c_{fr}**		**C_{rs}**

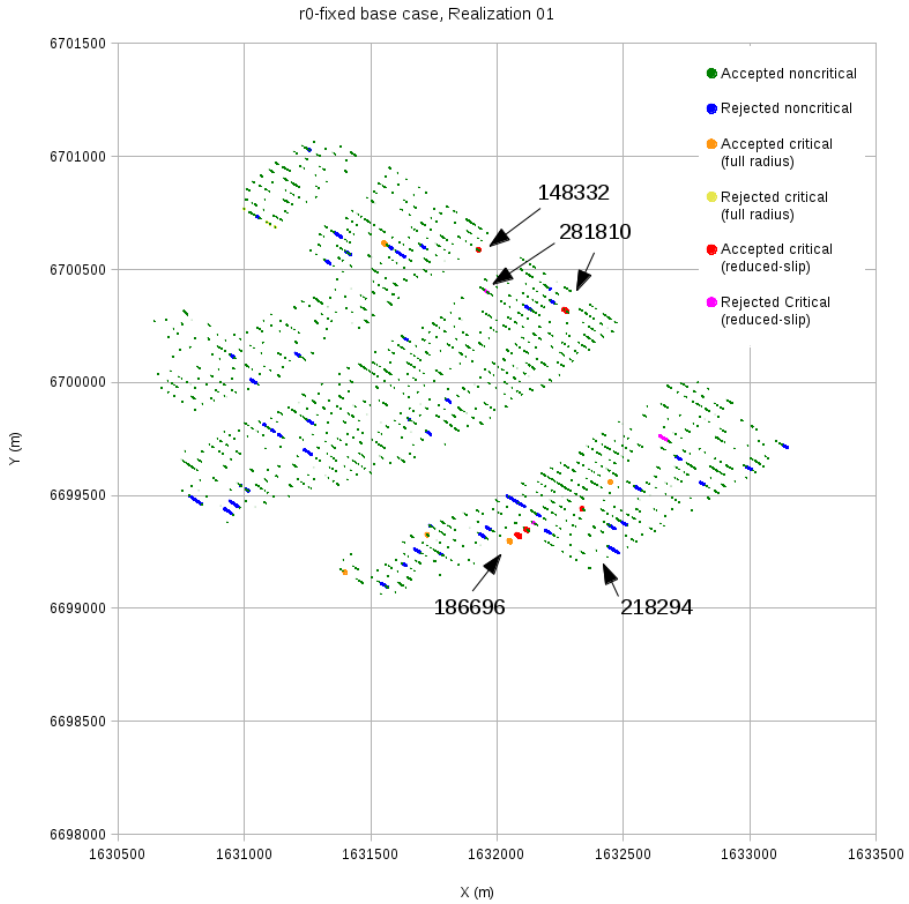

Figure 32: Deposition-hole positions that are accepted based on the FPC but are intersected by fractures, for Realization 01 of the r_0-fixed model, base case. The categories of intersected positions are distinguished by colour to show if they are accepted or rejected based on the EFPC, and whether they are classed as non-critical intersections or as one of the two classes of critical intersections (c_{fr} = full-radius or C_{rs} = reduced-slip) for at least one of the deformation zones. Larger dots are used to indicate the positions of critical fractures that are accepted even with the EFPC. Numbers and arrows point to the critical intersections that are associated with the fractures listed in Table 14. Gaps between dots along a given tunnel may be either locations that were avoided based on the FPC, or (in a small number of cases) deposition holes that are not intersected by any fractures and thus do not appear in the list of intersected holes.

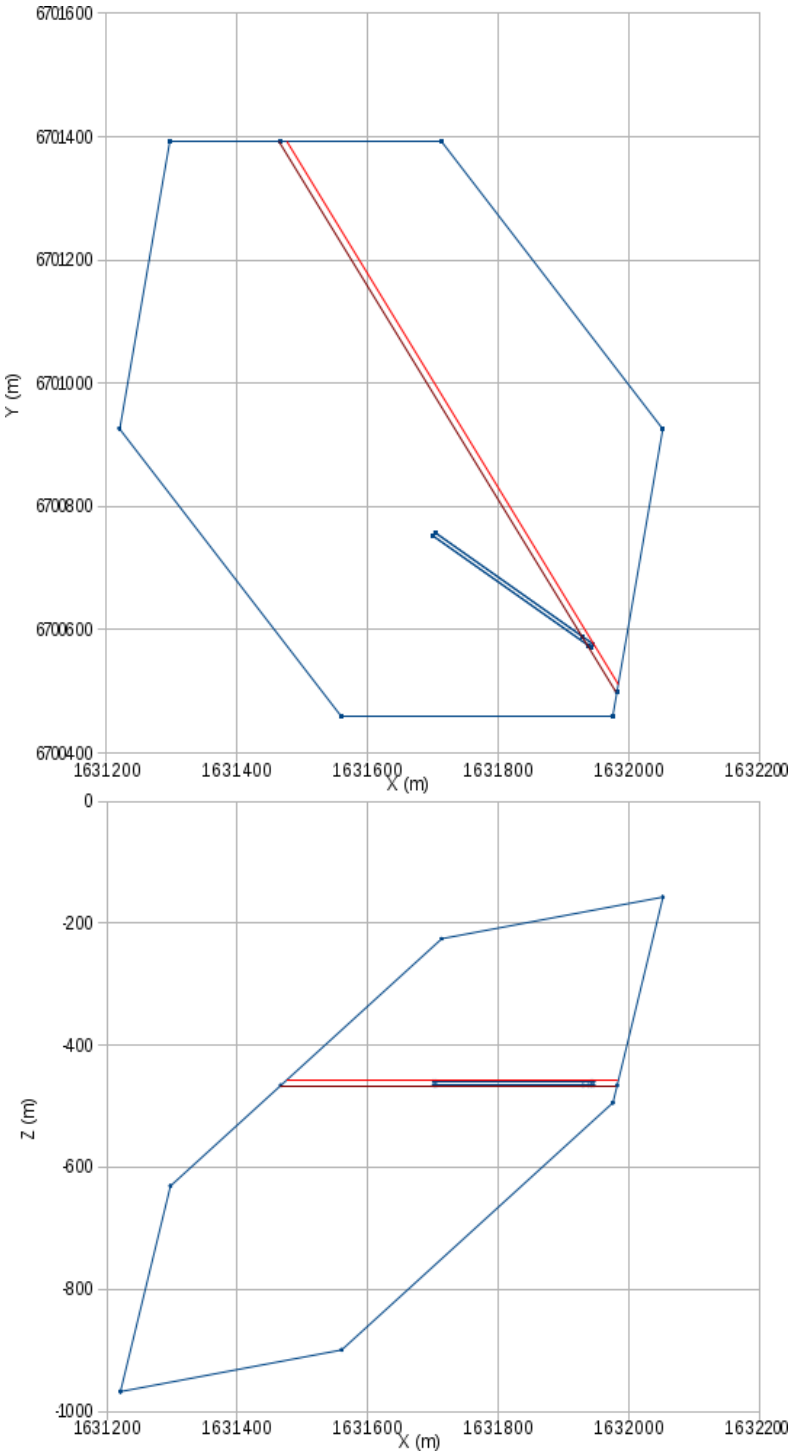

Figure 33: Orthogonal views (plan view in upper plot and elevation view in lower plot) of fracture 148332 and the deposition tunnel 86 with which it produces critical intersections with acceptable canister positions, for Realization 01 of the r_0-fixed base case. The darker red line in each plot shows the line along the strike of the fracture which is at the same depth as (and intersects) the tunnel floor. The brighter red line in each plot shows the line along the strike of the fracture which is at the same depth as the tunnel roof.

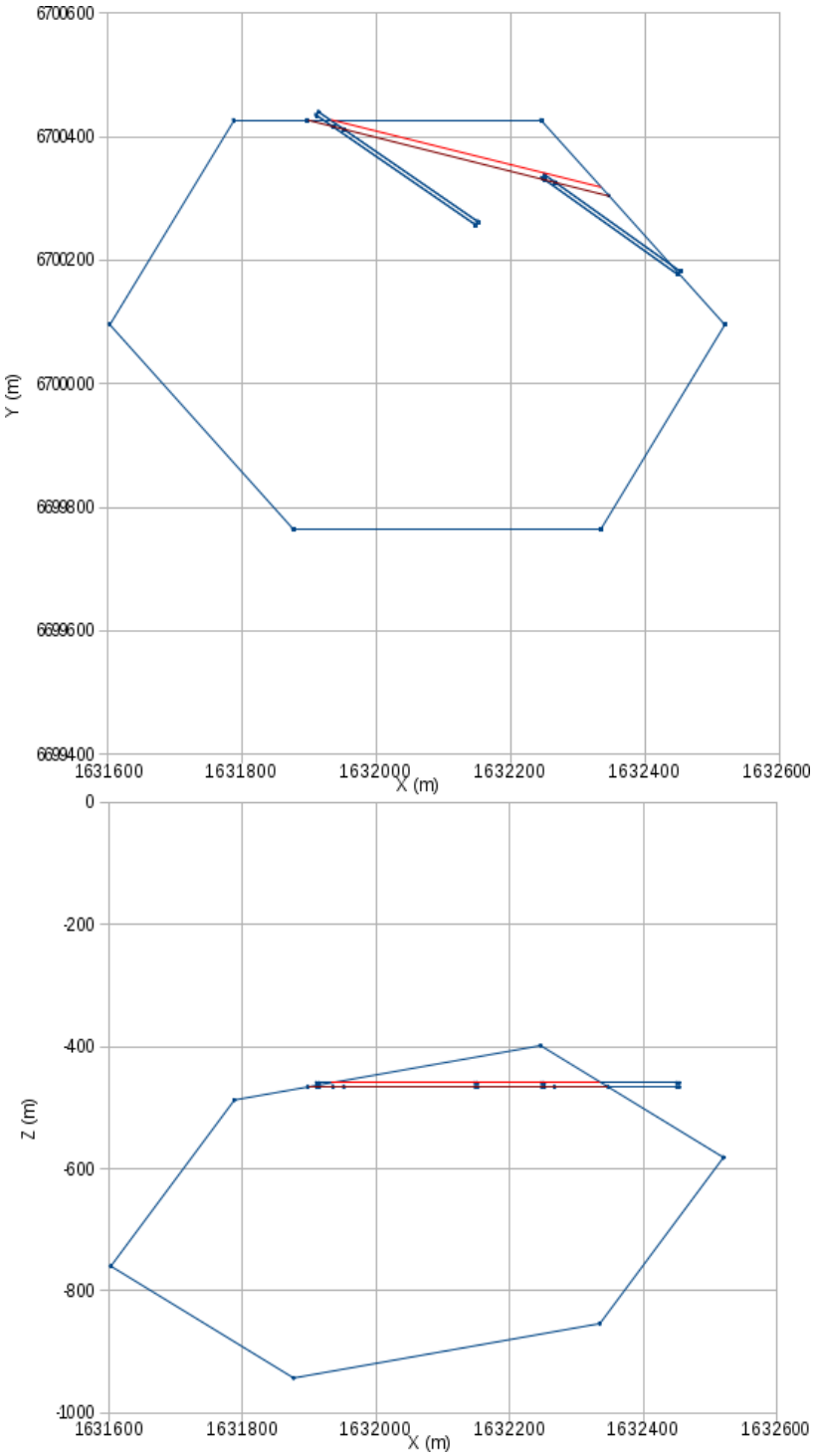

Figure 34: Orthogonal views (plan view in upper plot and elevation view in lower plot) of fracture 281810 and the deposition tunnels 155 and 167 with which it produces critical intersections with canister positions (rejected based on EFPC in tunnel 155 but accepted in tunnel 167), for Realization 01 of the r_0-fixed base case. The darker red line in each plot shows the line along the strike of the fracture which is at the same depth as (and intersects) the tunnel floor. The brighter red line in each plot shows the line along the strike of the fracture which is at the same depth as the tunnel roof.

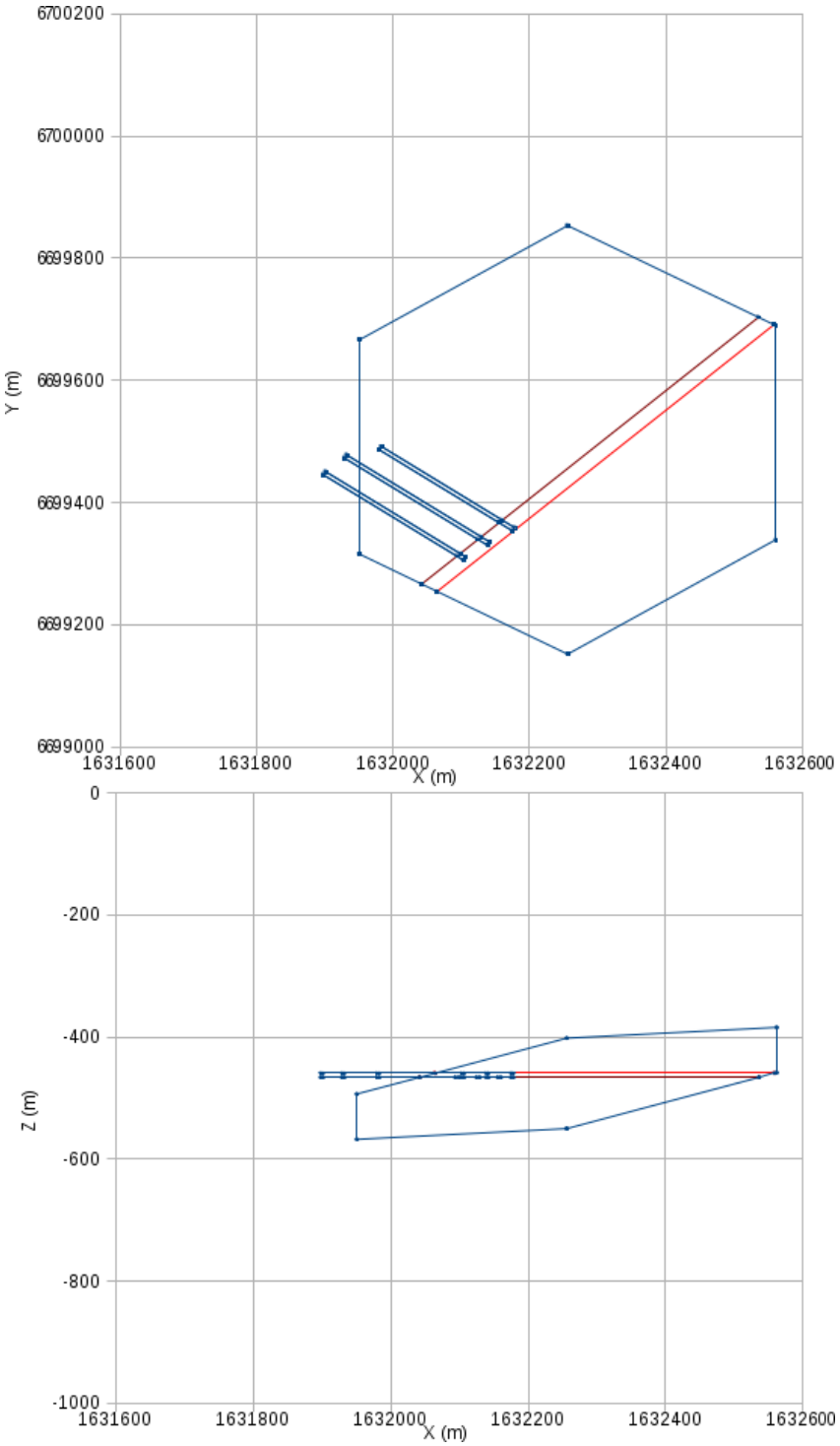

Figure 35: Orthogonal views (plan view in upper plot and elevation view in lower plot) of fracture 186696 and the deposition tunnels 183, 184, and 185 with which it produces critical intersections with canister positions (rejected based on EFPC in tunnel 185 but accepted in tunnels 183 and 184), for Realization 01 of the r_0-fixed base case. The darker red line in each plot shows the line along the strike of the fracture which is at the same depth as (and intersects) the tunnel floor. The brighter red line in each plot shows the line along the strike of the fracture which is at the same depth as the tunnel roof.

2.3.5. Discussion

The results obtained for N_{crit} (reduced-slip category C_{rs}) for the base case of each of the three DFN alternatives are compared with the results of Munier (2010) in Table 15.

Munier (2010) did not report results that are directly comparable for the reduced-slip category, but rather results based on a probabilistic-slip formula. According to Munier (2010) the probabilistic-slip formula yields N_{crit} values that are lower than the values for the reduced-slip formula used here, by about a factor of 4. Therefore for ease of comparison, the values reported by Munier (2010, Appendix 2) have been each been multiplied by a factor of 4 in Table 15.

From the between-models ratios given in Table 15, it can be seen that the present calculations produce N_{crit} values about an order of magnitude higher than SKB's results, for the r_0-fixed and OSM-TFM variants. For the TCM alternative, the two approaches yield results that are within a factor of 2.5.

The much lower between-models ratio for TCM alternative also means that there is a different ranking of the three alternatives in the present study, relative to SKB's results. In the present study the TCM alternative yields the lowest values of N_{crit}, whereas in SKB's calculations this alternative yielded the highest values of N_{crit}. A precise reason for this difference has not been identified; speculatively it could result from differences in the details of how the larger-radius portions of the fracture size distributions are simulated, as well as the systematic differences between SKB's and the present approach which are discussed below.

The between-models ratios for all three alternatives are anomalously high for the case of deformation zone ZFMNW0017. This deformation zone is one of the larger deformation zones, with $L > 5$ km. In relationship to most of the tunnels in the repository layout (as can be seen from Figure 1), it is only slightly farther away than the other NW to WNW striking deformation zones. Therefore it is surprising that SKB's model should yield such anomalously low values of N_{crit} for this deformation zone, up to an order of magnitude less than even the shorter zones with $L < 3$ km. The results from the present calculations indicate that the number of critical fractures in relation to ZFMNW0017 should be close in magnitude to the other deformation zones.

Table 15: Comparison of numbers of critical canister positions per repository simulation for the present calculations, versus the corresponding cases of SKB's calculations as given by Munier (2010). In both cases the numbers represent N_{crit} for fracture/deposition-hole intersections that escape both FPC and EFPC. The numbers listed for the present DFM-calculations are for the reduced-slip category C_{rs} ($r > r_{crit}$ and $r_x < r'_{crit}$). The numbers listed for SKB's calculations, based on Tables A2-1, A2-2, and A2-3 of Munier (2010), are obtained using the probabilistic-slip formula which, according to Munier (2010), yields only about 1/4th as many critical intersections as the reduced-slip formula. Therefore these values have been multiplied by a factor of 4, for ease of comparison to the results of the present study. Munier (2010) did not report N_{crit} values for deformation zones ZFMENE0060A and ZFMENE0062A, which SKB regards as stable for all future stress conditions, so a comparison of results is not given for these two zones.

DFN alternative		ZFM NW 0017	ZFM NW 1200	ZFM WNW 0123	ZFM WNW 0809A	ZFM A2	**Sum**
r_0-fixed	DFM (r3)	1.4	0.8	1.6	0.7	1.7	**6.2**
	SKB x 4	0.020	0.056	0.228	0.027	0.223	**0.554**
	Ratio	*70*	*14*	*7*	*26*	*8*	*11.2*
OSM-TFM	DFM (o3)	2.1	1.3	2.6	1.0	2.2	**9.2**
	SKB x 4	0.003	0.064	0.270	0.035	0.258	**0.630**
	Ratio	*700*	*20*	*10*	*29*	*9*	*14.6*
TCM	DFM (t2)	0.3	0.3	1.3	0.1	0.8	**2.8**
	SKB x 4	0.012	0.122	0.458	0.044	0.484	**1.12**
	Ratio	*15*	*2*	*3*	*2*	*2*	*2.5*

Differences in methodology

Several details of implementation between the present study and the methods of Munier (2010) have been identified:

1. The lengths of deposition tunnels were variable based on the D2 layout, rather than using a fixed tunnel length L_i = 330 m (Munier, 2010, p. 61). This is longer than all tunnels in the D2 layout, which have lengths in the range 109 m $\leq L_i \leq$ 301 m, with a mean L_i = 264 m. Shorter tunnels implies that more tunnels are needed to store a given number of canisters, and hence increases the consequences of tunnel-end effects. Most critical fractures that are missed by the EFPC and FPC occur near the ends of deposition tunnels. The number of tunnel ends in a given repository is inversely proportional to the mean L_i. Thus the more realistic use of shorter tunnels leads to higher values of N_{crit} in the present calculations, compared with the results of Munier (2010), by an estimated factor effect of:

   (330 m) / (264 m) = 1.250 Eq. (2.18)

2. Deposition holes are here only excluded under the FPC if they are actually intersected by the finite, polygonal FPI feature, rather than by its projected

plane. SKB's implementation will result in rejection of some deposition holes that would be accepted by the present implementation, if a FPI fracture terminates just below the tunnel floor without intersecting the canister position. This could increase utilization factors obtained here, relative to a more exact implementation of SKB's criterion. However, this should not affect N_{crit} values, as these FPI fractures do not intersect the canister.

3. Munier (2010, p. 50) assumes that fractures crossing at an angle through the bottom end of a deposition hole, such as the case shown in Figure 4 e), would not be detectable. Here this case is considered to be detectable. This is less conservative than the assumption of Munier (2010), but the effect on N_{crit} is expected to be inconsequential because only a very narrow range of fracture dip angles can produce this type of intersection and also intersect the canister, yet (if large enough to be critical fractures) not be detected as an FPI in the tunnel.

4. SKB's calculations of N_{crit} by Munier (2010) apparently are based on the larger layout with additional tunnels, as illustrated in Figure 14. The main consequence of this larger layout, in terms of N_{crit} calculations, is that it includes a few more tunnels that are relatively close to deformation zone ZFMWNW0809A on the NE side, and to zones ZFMENE0062A, ZFMNW0123, and ZFMA2 on the S side of the repository. This could be expected to increase SKB's calculated values of N_{crit}, to some degree, relative to the smaller layout considered here.

5. The slightly higher value of canister spacing $l_{spacing}$ = 6.8 m for rock domain RFM045 (corresponding to fracture domain FFM06) is not taken into account in the present calculations. Considering that RFM045 accounts for approximately 20% of the rock volume in the repository according to SKB (2009), the utilization factors calculated here will be higher than a simulation that uses a larger minimum spacing in RFM06, by a factor of about:

$$\frac{\frac{L}{6.0m}}{\frac{0.8L}{6.0m}+\frac{0.2L}{6.8m}} = 1.024 \qquad \text{Eq. (2.19)}$$

where L is the total length of deposition tunnels in the repository layout. Thus use of a uniform 6.0 m spacing is expected to increase *DoU* estimates by about 2.4% relative to those calculated by SKB. This does not directly affect N_{crit}. It may have indirect effects resulting from the positions in which canisters are placed, but the consequences when averaged over the full set of realizations are not expected to be significant.

6. The meaning of the critical radius categories ">300 m" and ">>300 m" is not explicit from the exposition by Munier (2010). Here these categories have been treated conservatively as yielding exactly 300 and 400 m respectively. If Munier (2010) assigned larger values of r_{crit} in the numerical implementation of SKB's model, this would tend to produce

lower values of N_{crit}. However the magnitude of this effect cannot be estimated without more quantitative information on SKB's calculations.

The first of these differences (i.e. tunnel length) is judged to be the main systematic difference, among those that have been identified and can be quantified, that could affect N_{crit} calculations. The expected effect is that N_{crit} using actual tunnel lengths should be increased by about a factor of 1.25, in comparison with the results of Munier (2010).

There are likely other differences that have not been identified, due to the general difference in overall approach. The results presented here are based on explicit Monte Carlo simulation of the detailed repository layout, whereas Munier (2010) calculated N_{crit} values for a single tunnel of idealized geometry, and then used mathematical probabilistic arguments to upscale these to a full repository layout. More detailed review of the mathematical assumptions of Munier (2010), alongside of the present model, could perhaps reveal further explanations of the differences.

Conservatism of SKB's approach

Munier (2010) presents three different formulae for critical radius – full-radius, reduced-slip, and probabilistic slip – but presents final results for N_{crit} only in terms of the third one which is the least conservative. The reasoning for this choice is based on numerical modelling of slip on secondary fractures due to earthquakes on deformation zones by Fälth et al. (2010).

Taking credit for decay of slip toward the edge of a fracture is based on an idealized model of fracture as a circular disk, with zero displacement at the circumference. A substantial percentage of the fractures at Forsmark are observed to terminate at other fractures, rather than in intact rock (Fox et al., 2007). For such fractures, the zero-displacement boundary condition assumed by Munier (2010) and Hedin (2011) is not guaranteed.

Munier (2010) follows Hedin (2011) in arguing for a further reduction in the portion of a fracture over which, probabilistically speaking, a critical shear displacement could take place, due to differences in fracture orientation and location relative to the fault tip. This reasoning, again based on the numerical modelling results of Fälth et al. (2010), leads to a "probabilistic" mean critical radius which gives more optimistic results than the assumptions considered here, by a factor of 4.

Evaluation of the modelling results of Fälth et al. (2010) is outside the scope of this assignment, but clearly the reliability of these results, and the scope of uncertainties considered, are key for deciding which of the three definitions of critical radius – full-radius, reduced-slip, or probabilistic-slip – should be regarded as most realistic, or most reasonably conservative.

From comparison of Tables 12 and 13, it can be seen that the full-radius definition of critical radius leads to N_{crit} values that are about an order of magnitude higher than those produced by the reduced-slip definition. The probabilistic-slip definition leads to a further reduction by a factor of 4. Thus the difference between the full-

radius definition and the probabilistic-slip definition of critical radius leads to about 1.5 orders of magnitude difference in estimates of the number of critical positions in the repository.

Effectiveness and efficiency of FPC and EFPC

Depending on the Geo-DFN alternative considered, and the variant with respect to fracture intensity, the basic full-perimeter-intersection criterion (FPC) leads to rejection of 500 to 1400 canister positions. The extended criterion (EFPC), based on rejecting canister positions that are intersected by fractures that are detectable in 5 or more consecutive deposition holes in a given tunnel, leads to rejection of 200 to 800 additional positions.

Overall degree-of-utilization *DoU* when using both FPC and EFPC ranges from about 81% to 96%, depending on the Geo-DFN alternative, P_{32} variant, and realization. Thus the cost of applying these criteria ranges from very small (only 4% less than full utilization) to moderate, assuming that the Geo-DFN alternatives adequately span the range of conditions that could be encountered underground.

The present calculations have not included evaluation of N_{crit} for a repository in which neither the FPC nor the EFPC is applied. Hence the efficiency of the FPC cannot be evaluated, without a comparison to additional repository simulations in which this criterion is switched off.

The effectiveness of the EFPC can be measured by comparing Table 10 versus Table 12 (for N_{crit} based on the full-radius criterion), and Table 11 versus Table 13 (for N_{crit} based on the reduced-slip criterion). In the full-radius case, the EFPC yields reductions by a factor of 3 to 4 depending on the Geo-DFN alternative. In the reduced-slip case, the reductions are by roughly a factor of 5. Thus for a cost ranging from 3% to 12% in terms of number of rejected canister positions, a reduction in N_{crit} by a factor of 3 to 5 is obtained.

3. The Consultant's overall assessment

Results have been presented for the number of critical positions N_{crit} that can be expected in a KBS-3 repository at Forsmark, based on three different Geo-DFN alternatives as developed from surface-based site characterization data by SKB, the interpreted configuration of deformation zones that could potentially host future earthquakes according to SKB's analysis, and the positions of deposition tunnels within the proposed D2 layout. The calculations have explicitly taken account of SKB's full-perimeter intersection criterion (FPC) and extended criterion (EFPC).

The results indicate higher values of N_{crit} than SKB has calculated, by factors ranging from 2.5 to 14 depending on the Geo-DFN alternative. Differences in implementation that have been identified can account for only a small part of this difference. The main identified difference, i.e. tunnel length, can only account for about a 25% increase relative to SKB's estimates of N_{crit}. Therefore further examination of the mathematical assumptions of SKB's model is advisable. In particular, SKB's values of N_{crit} for one of the longer deformation zones, ZFMNW0017, appear to be anomalously low even in comparison with SKB's calculations for other deformation zones.

Among the Geo-DFN alternatives considered, the OSM-TFM alternative yields the highest values of N_{crit} when both FPC and EFPC are used, by roughly a factor of 3 in comparison with the TCM alternative which yields the lowest values. The high values for the OSM-TFM model are thought to be a result of the comparatively large number of fractures with radius on the order of 100 m, and possibly also due to the preferred orientations of the dominant fracture sets with respect to the repository layout.

The critical positions that were found in the present study are mainly proximal to the ends of deposition tunnels. For the cases in which critical positions occur near the plug end of a deposition tunnel, the geometry is frequently such that the fracture would intersect the adjacent access tunnel. For either this case or the case in which critical intersections occur near the blind end of a deposition tunnel, frequently the same fracture would be avoided in neighbouring tunnels based on full-perimeter intersections. Hence the argument advanced by SKB, that many of these fractures could be avoided by making use of information from multiple tunnels, is reasonable at least for the idealized, perfectly planar fractures considered in these models.

The effectiveness of the EFPC can be evaluated in terms of the number of deposition holes that would be abandoned based on this criterion, versus the reduction in N_{crit} that is thus obtained. For a cost ranging from about 3% to 12% in terms of rejected canister positions, a reduction in N_{crit} by a factor of 3 to 5 is obtained. Whether or not this should be regarded as efficient depends on the weight (in terms of economics and/or risk) that is given to these measures.

4. References

Aho, A.V., Kernighan, B.W., and Weinberger, P.J., 1988. The AWK Programming Language. Addison-Wesley, 1988. ISBN 0-201-07981-X.

Dershowitz, 1984. Rock Joint Systems. Ph.D. dissertation, Massachusetts Institute of Technology, Cambridge, Massachusetts.

Dershowitz, W. S., Lee, G., Geier, J., Foxford, T., LaPointe, P., and Thomas, A., 1996. FracMan^{TM}: Interactive discrete feature data analysis, geometric modeling, and exploration simulation: User Documentation, Version 2.5, Golder Associates Inc., Redmond, Washington.

Fox, A., La Pointe, P., Hermanson, J., and Öhman, J., 2007. Statistical geological discrete fracture network model. Forsmark modelling stage 2.2. SKB R-07-46, Swedish Nuclear Fuel and Waste Management Co (SKB).

Fälth, B., Hökmark, H., and Munier, R., 2010. Effects of large earthquakes on a KBS-3 repository. Evaluation of modelling results and their implications for layout and design. SKB Technical Report TR-08-11. Swedish Nuclear Fuel and Waste Management Co (SKB).

Geier, J., 2008. Discrete Feature Model (DFM) User Documentation. SKI Report 08:57, Swedish Nuclear Power Inspectorate (SKI).

Geier, J., 2010. Discrete-feature model implementation of SDM-Site Forsmark. SSM Report 2010:05, Swedish Radiation Safety Authority (SSM).

Geier, J., 2011. Investigation of Discrete-Fracture Network conceptual model uncertainty at Forsmark. SSM Report 2011:13, Swedish Radiation Safety Authority (SSM).

Mardia, K.V., 1972. Statistics of Directional Data, Academic Press, London, 339 p.

Mardia, K.V., Kent, J.T., and Bibby, J.M., 1979. Multivariate Analysis, Academic Press, London, 521 p.

Munier R, 2006. Using observations in deposition tunnels to avoid intersections with critical fractures in deposition holes. SKB R-06-54, Swedish Nuclear Fuel and Waste Management Co (SKB).

Munier, R., 2010. Full perimeter intersection criteria. Definitions and implementations in SR-Site. SKB Technical Report TR-10-21, Swedish Nuclear Fuel and Waste Management Co (SKB).

SKB, 2008. Site description of Forsmark at completion of the site investigation phase. SKB Technical Report TR-08-05. Swedish Nuclear Fuel and Waste Management Co (SKB).

SKB, 2009. Underground Design Forsmark Layout D2. SKB Report R-08-116. Swedish Nuclear Fuel and Waste Management Co (SKB).

SKB, 2010a. Design, construction and initial state of the underground openings. Updated 2013-01, SKB Technical Report TR-10-18, Swedish Nuclear Fuel and Waste Management Co (SKB).

SKB, 2010b.Design, production and initial state of the canister. Updated 2013-10, SKB Technical Report TR-10-14, Swedish Nuclear Fuel and Waste Management Co (SKB).

SKB, 2010c. Data report for the safety assessment SR-Site. Updated 2014-01, SKB Technical Report TR-10-52, Swedish Nuclear Fuel and Waste Management Co (SKB).

SKB, 2011. Long-term safety for the final repository for spent nuclear fuel at Forsmark. Main report of the SR-Site project. Updated 2012-12, SKB Technical Report TR-11-01. Swedish Nuclear Fuel and Waste Management Co (SKB).

Snow, D.T., 1965. *A Parallel Plate Model of Fractured Permeable Media*. Ph.D. dissertation, University of California, Berkeley, 331 pp.

Witherspoon, P.A., Wang, J.S.Y., Iwai, K., and Gale, J.E., 1980. Validity of cubic law for fluid flow in a deformable fracture. *Water Resources Research* v. 16, no. 6, p. 1016-1024.

APPENDIX 1

Coverage of SKB reports

Table 1: SKB reports considered in the present calculations.

Reviewed report	Reviewed sections	Comments
SKB TR-08-05	All	Forsmark site descriptive used as general background for this analysis.
SKB TR-10-21	All	Focus was on understanding the methodology for implementation of an alternative model for calculations, rather than review of the results.
SKB R-06-54	All	Considered as an earlier version of theoretical development for SKB TR-10-21.
SKB R-07-46	DFN tables only	Source of parameters (in addition to TR-10-21) for model implementation.
SKB R-08-11	Skimmed	Used only as background information with respect to SKB TR-10-21.
SKB R-08-116	Skimmed	Focus was on checking description of the D2 layout and underground opening parameters, rather than a full review.

APPENDIX 2

Model setup and post-processing scripts

A2.1 Fracture generation

Fractures for each of the DFN calculation cases were generated using Linux C shell scripts with titles of the form: SRSite_PFC_fracgen_*case* where *case* = {r3, o3, t2, rg2, og3, tg2} depending on the calculation case. These scripts all run the DFM-*fracgen* module:

fracgen (version 2.4.1.1, executable fracgen2411 compiled March 5, 2014)

The script for the r3 calculation case (r0-fixed alternative, base case) is provided as an example. Key input files for this script are listed under separate headings below.

SRSite_PFC_fracgen_r3

```
#!/bin/csh -f
#
# Script used to generate fractures and grid cells for DFM model of
Forsmark
# site based on SKB's SDM-Site site descriptive model, using dense
shells.
#
  set SEED    = $1
  set OUT     = SRGeoPFC_r3_$SEED
  set DOMAINS = "../FractureDomains"
  set LIST    = ""
  set N       = 0

  set SITES   = SDMForsmark468m.sites
  set SHELLS  = Forsmark_Ncrit0.shells

  set DOMSTEM = "FM_reg_v22_basemod_FFM"

  foreach FD ( 01 06 ) # Loop over fracture domains.
     if ( $FD == "01" || $FD == "06" ) then
        set FSETS = $FD
     else if ( $FD == "02" ) then
        set FSETS = "02"
     else
        set FSETS = "03"
     endif
     set SET = "GeoFFM""$FSETS""r0-fixed_r2.sets"
     set DOM = "$DOMAINS/$DOMSTEM$FD"".domain"
     set LIST = "$LIST $SET $DOM"
     # echo $LIST
     @ N ++
  end
```

```
  echo "fracgen2411 -o $OUT -s $SITES $SHELLS 6 $SEED $N $LIST" >
$OUT.log
        fracgen2411 -o $OUT -s $SITES $SHELLS 6 $SEED $N $LIST >>
$OUT.log
```

Fracture set definition files

The following files give the parameters that define each of the fracture sets. There are two files (one for each fracture domain FFM01 and FFM06) for each of the six calculation case. Note that the files with suffix “r2” were used for calculation case r3,

GeoFFM01r0-fixed_r2.sets

```
#
# Forsmark SDM-Site
# GeoDFN fracture sets for FFM01
# Increased r_min to 3.0 m.
#
# Facture geometry statistics (orientation and size distributions) and
global P32 based on:
# SKB TR-21 (Munier, 2010) Appendix 3, Table A3.1 (r0-fixed
alternative).
#
# Fracture transmissivity is set to an arbitrary constant value T =
1e-10 m2/s
# to keep things simple for mechanical calculations.
#
Set 1   # NE global
Transmissivity Constant  1e-10
Storativity    Constant  1e-8
Aperture       CubicLaw
Radius         Powerlaw  3.718 0.039  limits 3.0 564.2
Location       Poisson
Orientation    Fisher    trend 314.9 plunge 1.3  kappa 20.94
Intensity      P32       1.733 unscaled
Set 2   # NS global
Transmissivity Constant  1e-10
Storativity    Constant  1e-8
Aperture       CubicLaw
Radius         Powerlaw  3.745 0.039  limits 3.0 564.2
Location       Poisson
Orientation    Fisher    trend 270.1 plunge 5.3  kappa 21.34
Intensity      P32       1.292 unscaled
Set 3   # NW global
Transmissivity Constant  1e-10
Storativity    Constant  1e-8
Aperture       CubicLaw
Radius         Powerlaw  3.607 0.039  limits 3.0 564.2
Location       Poisson
Orientation    Fisher    trend 230.1  plunge 4.6  kappa 15.7
Intensity      P32       0.948 unscaled
Set 4   # SH global
Transmissivity Constant  1e-10
Storativity    Constant  1e-8
Aperture       CubicLaw
Radius         Powerlaw  3.579 0.039  limits 3.0 564.2
Location       Poisson
Orientation    Fisher    trend 0.8 plunge 87.3 kappa 17.42
Intensity      P32       0.624 unscaled
Set 5  # ENE local
Transmissivity Constant  1e-10
Storativity    Constant  1e-8
Aperture       CubicLaw
Radius         Powerlaw  3.972 0.039  limits 3.0 564.2
```

```
Location       Poisson
Orientation    Fisher    trend 157.5 plunge 3.1 kappa 34.11
Intensity      P32       0.256 unscaled
Set 6   # EW local
Transmissivity Constant  1e-10
Storativity    Constant  1e-8
Aperture       CubicLaw
Radius         Powerlaw  3.930 0.039  limits 3.0 564.2
Location       Poisson
Orientation    Fisher    trend 0.4 plunge 11.9 kappa 13.89
Intensity      P32       0.169 unscaled
Set 7  # NNE local
Transmissivity Constant  1e-10
Storativity    Constant  1e-8
Aperture       CubicLaw
Radius         Powerlaw  4.000 0.039  limits 3.0 564.2
Location       Poisson
Orientation    Fisher    trend 293.8 plunge 0.0 kappa 21.79
Intensity      P32       0.658 unscaled
Set 8  # SH2 local
Transmissivity Constant  1e-10
Storativity    Constant  1e-8
Aperture       CubicLaw
Radius         Powerlaw  3.610 0.039  limits 3.0 564.2
Location       Poisson
Orientation    Fisher    trend 164.0 plunge 52.6 kappa 35.43
Intensity      P32       0.081 unscaled
Set 9  # SH3 local
Transmissivity Constant  1e-10
Storativity    Constant  1e-8
Aperture       CubicLaw
Radius         Powerlaw  3.610 0.039  limits 3.0 564.2
Location       Poisson
Orientation    Fisher    trend 337.9 plunge 52.9 kappa 17.08
Intensity      P32       0.067 unscaled
```

GeoFFM06r0-fixed_r2.sets

```
#
# Forsmark SDM-Site
# GeoDFN fracture sets for FFM06
# Increased r_min to 3 m.
#
# Facture geometry statistics (orientation and size distributions) and
global P32 based on:
# SKB TR-21 (Munier, 2010) Appendix 3, Table A3.1 (r0-fixed
alternative).
#
# Corrected power-law exponent for Set 2 (NS global) and Set 5 (ENE
local).
#
# Fracture transmissivity is set to an arbitrary constant value T =
1e-10 m2/s
# to keep things simple for mechanical calculations.
#
Set 1   # NE global
Transmissivity Constant  1e-10
Storativity    Constant  1e-8
Aperture       CubicLaw
Radius         Powerlaw  3.785 0.039  limits 3.0 564.2
Location       Poisson
Orientation    Fisher    trend 125.7 plunge 10.10  kappa 45.05
Intensity      P32       3.299 unscaled
Set 2   # NS global
Transmissivity Constant  1e-10
Storativity    Constant  1e-8
Aperture       CubicLaw
Radius         Powerlaw  3.780 0.039  limits 3.0 564.2
Location       Poisson
```

```
Orientation    Fisher    trend  91.0 plunge 4.1  kappa 19.49
Intensity      P32       2.150 unscaled
Set 3   # NW global
Transmissivity Constant  1e-10
Storativity    Constant  1e-8
Aperture       CubicLaw
Radius         Powerlaw  3.662 0.039  limits 3.0 564.2
Location       Poisson
Orientation    Fisher    trend  34.1  plunge 0.8  kappa 16.13
Intensity      P32       1.608 unscaled
Set 4   # SH global
Transmissivity Constant  1e-10
Storativity    Constant  1e-8
Aperture       CubicLaw
Radius         Powerlaw  3.582 0.039  limits 3.0 564.2
Location       Poisson
Orientation    Fisher    trend 84.3 plunge 71.3 kappa 10.78
Intensity      P32       0.640 unscaled
Set 5  # ENE local
Transmissivity Constant  1e-10
Storativity    Constant  1e-8
Aperture       CubicLaw
Radius         Powerlaw  3.865 0.039  limits 3.0 564.2
Location       Poisson
Orientation    Fisher    trend 155.4 plunge 8.3 kappa 20.83
Intensity      P32       0.194 unscaled
Set 6  # SH2 local
Transmissivity Constant  1e-10
Storativity    Constant  1e-8
Aperture       CubicLaw
Radius         Powerlaw  3.610 0.039  limits 3.0 564.2
Location       Poisson
Orientation    Fisher    trend   0.0 plunge 47.5 kappa 12.71
Intensity      P32       0.429 unscaled
```

GeoFFM01r0-fixed_rg2.sets

```
#
# Forsmark SDM-Site
# GeoDFN fracture sets for FFM01
#
# Facture geometry statistics (orientation and size distributions) and
global P32 based on:
# SKB TR-21 (Munier, 2010) Appendix 3, Table A3.1 (r0-fixed
alternative).
#
# P32 values have been increased by 25% to test sensitivity to
uncertainty and heterogeneity of DFN.
# Original P32 values are retained for comparison, following the #
symbol.
# The minimum fracture radius has been increased to 3.0 m.
#
# Fracture transmissivity is set to an arbitrary constant value T =
1e-10 m2/s
# to keep things simple for mechanical calculations.
#
Set 1   # NE global
Transmissivity Constant  1e-10
Storativity    Constant  1e-8
Aperture       CubicLaw
Radius         Powerlaw  3.718 0.039  limits 3.0 564.2
Location       Poisson
Orientation    Fisher    trend 314.9 plunge 1.3  kappa 20.94
Intensity      P32       2.166 unscaled # 1.733 unscaled
Set 2   # NS global
Transmissivity Constant  1e-10
Storativity    Constant  1e-8
Aperture       CubicLaw
Radius         Powerlaw  3.745 0.039  limits 3.0 564.2
```

```
Location       Poisson
Orientation    Fisher    trend 270.1 plunge 5.3  kappa 21.34
Intensity      P32       1.615 unscaled # 1.292 unscaled
Set 3   # NW global
Transmissivity Constant  1e-10
Storativity    Constant  1e-8
Aperture       CubicLaw
Radius         Powerlaw  3.607 0.039  limits 3.0 564.2
Location       Poisson
Orientation    Fisher    trend 230.1  plunge 4.6  kappa 15.7
Intensity      P32       1.185 unscaled # 0.948 unscaled
Set 4   # SH global
Transmissivity Constant  1e-10
Storativity    Constant  1e-8
Aperture       CubicLaw
Radius         Powerlaw  3.579 0.039  limits 3.0 564.2
Location       Poisson
Orientation    Fisher    trend 0.8 plunge 87.3 kappa 17.42
Intensity      P32       0.780 unscaled # 0.624 unscaled
Set 5  # ENE local
Transmissivity Constant  1e-10
Storativity    Constant  1e-8
Aperture       CubicLaw
Radius         Powerlaw  3.972 0.039  limits 3.0 564.2
Location       Poisson
Orientation    Fisher    trend 157.5 plunge 3.1 kappa 34.11
Intensity      P32       0.320 unscaled # 0.256 unscaled
Set 6   # EW local
Transmissivity Constant  1e-10
Storativity    Constant  1e-8
Aperture       CubicLaw
Radius         Powerlaw  3.930 0.039  limits 3.0 564.2
Location       Poisson
Orientation    Fisher    trend 0.4 plunge 11.9 kappa 13.89
Intensity      P32       0.211 unscaled # 0.169 unscaled
Set 7  # NNE local
Transmissivity Constant  1e-10
Storativity    Constant  1e-8
Aperture       CubicLaw
Radius         Powerlaw  4.000 0.039  limits 3.0 564.2
Location       Poisson
Orientation    Fisher    trend 293.8 plunge 0.0 kappa 21.79
Intensity      P32       0.823 unscaled # 0.658 unscaled
Set 8  # SH2 local
Transmissivity Constant  1e-10
Storativity    Constant  1e-8
Aperture       CubicLaw
Radius         Powerlaw  3.610 0.039  limits 3.0 564.2
Location       Poisson
Orientation    Fisher    trend 164.0 plunge 52.6 kappa 35.43
Intensity      P32       0.101 unscaled # 0.081 unscaled
Set 9  # SH3 local
Transmissivity Constant  1e-10
Storativity    Constant  1e-8
Aperture       CubicLaw
Radius         Powerlaw  3.610 0.039  limits 3.0 564.2
Location       Poisson
Orientation    Fisher    trend 337.9 plunge 52.9 kappa 17.08
Intensity      P32       0.084 unscaled # 0.067 unscaled
```

GeoFFM06r0-fixed_rg2.sets

```
#
# Forsmark SDM-Site
# GeoDFN fracture sets for FFM06
#
# Facture geometry statistics (orientation and size distributions) and
global P32 based on:
```

```
# SKB TR-21 (Munier, 2010) Appendix 3, Table A3.1 (r0-fixed
alternative).
#
# P32 values have been increased by 25% to test sensitivity to
uncertainty and heterogeneity.
# The original P32 values have been retained for reference following
the # symbols.
#
# Corrected power-law exponent for Set 2 (NS global) and Set 5 (ENE
local).
# The minimum fracture radius has been increased to 3.0 m.
#
# Fracture transmissivity is set to an arbitrary constant value T =
1e-10 m2/s
# to keep things simple for mechanical calculations.
#
Set 1   # NE global
Transmissivity Constant  1e-10
Storativity    Constant  1e-8
Aperture       CubicLaw
Radius         Powerlaw  3.785 0.039  limits 3.0 564.2
Location       Poisson
Orientation    Fisher    trend 125.7 plunge 10.10  kappa 45.05
Intensity      P32       4.124 unscaled # 3.299 unscaled
Set 2   # NS global
Transmissivity Constant  1e-10
Storativity    Constant  1e-8
Aperture       CubicLaw
Radius         Powerlaw  3.780 0.039  limits 3.0 564.2
Location       Poisson
Orientation    Fisher    trend  91.0 plunge 4.1  kappa 19.49
Intensity      P32       2.688 unscaled # 2.150 unscaled
Set 3   # NW global
Transmissivity Constant  1e-10
Storativity    Constant  1e-8
Aperture       CubicLaw
Radius         Powerlaw  3.662 0.039  limits 3.0 564.2
Location       Poisson
Orientation    Fisher    trend  34.1  plunge 0.8  kappa 16.13
Intensity      P32       2.010 unscaled # 1.608 unscaled
Set 4   # SH global
Transmissivity Constant  1e-10
Storativity    Constant  1e-8
Aperture       CubicLaw
Radius         Powerlaw  3.582 0.039  limits 3.0 564.2
Location       Poisson
Orientation    Fisher    trend 84.3 plunge 71.3 kappa 10.78
Intensity      P32       0.800 unscaled # 0.640 unscaled
Set 5  # ENE local
Transmissivity Constant  1e-10
Storativity    Constant  1e-8
Aperture       CubicLaw
Radius         Powerlaw  3.865 0.039  limits 3.0 564.2
Location       Poisson
Orientation    Fisher    trend 155.4 plunge 8.3 kappa 20.83
Intensity      P32       0.243 unscaled # 0.194 unscaled
Set 6  # SH2 local
Transmissivity Constant  1e-10
Storativity    Constant  1e-8
Aperture       CubicLaw
Radius         Powerlaw  3.610 0.039  limits 3.0 564.2
Location       Poisson
Orientation    Fisher    trend   0.0 plunge 47.5 kappa 12.71
Intensity      P32       0.536 unscaled # 0.429 unscaled
```

GeoFFM01_osm_tfm_o3.sets

```
#
# Forsmark SDM-Site
# GeoDFN fracture sets for FFM01
#
# Fracture geometry statistics (orientation and size distributions)
and global P32 based on:
# SKB TR-21 (Munier, 2010, Update 2013-12) Appendix 3, Table A3.1
(OSM+TCM alternative).
#
# Fracture transmissivity is set to an arbitrary constant value T =
1e-10 m2/s
# to keep things simple for mechanical calculations.
#
Set 1   # OSM NE global
Transmissivity Constant  1e-10
Storativity    Constant  1e-8
Aperture       CubicLaw
Radius         Powerlaw  3.640 0.0385  limits 3.0 28
Location       Poisson
Orientation    Fisher    trend 314.9 plunge 1.3  kappa 20.943
Intensity      P32       0.0800  # 1.709425143 unscaled
Set 2   # OSM NS global
Transmissivity Constant  1e-10
Storativity    Constant  1e-8
Aperture       CubicLaw
Radius         Powerlaw  3.900 0.0385  limits 3.0 28
Location       Poisson
Orientation    Fisher    trend 270.1 plunge 5.3  kappa 21.33938
Intensity      P32       0.0222  # 1.289614635 unscaled
Set 3   # OSM NW global
Transmissivity Constant  1e-10
Storativity    Constant  1e-8
Aperture       CubicLaw
Radius         Powerlaw  3.440 0.0385  limits 3.0 28
Location       Poisson
Orientation    Fisher    trend 230.1  plunge 4.6  kappa 15.70056
Intensity      P32       0.0827  # 0.898302275 unscaled
Set 4   # OSM SH global
Transmissivity Constant  1e-10
Storativity    Constant  1e-8
Aperture       CubicLaw
Radius         Powerlaw  3.610 0.0385  limits 3.0 28
Location       Poisson
Orientation    Fisher    trend 0.8 plunge 87.3 kappa 17.4185
Intensity      P32       0.0321  # 0.615018629 unscaled
Set 5  # OSM ENE local
Transmissivity Constant  1e-10
Storativity    Constant  1e-8
Aperture       CubicLaw
Radius         Powerlaw  3.200 0.0385  limits 3.0 28
Location       Poisson
Orientation    Fisher    trend 157.5 plunge 3.1 kappa 34.11
Intensity      P32       0.0283  # 0.187727553 unscaled
Set 6   # OSM EW local
Transmissivity Constant  1e-10
Storativity    Constant  1e-8
Aperture       CubicLaw
Radius         Powerlaw  4.060 0.0385  limits 3.0 28
Location       Poisson
Orientation    Fisher    trend 0.4 plunge 11.9 kappa 13.89333
Intensity      P32       0.0015  # 0.168460531 unscaled
Set 7  # OSM NNE local
Transmissivity Constant  1e-10
Storativity    Constant  1e-8
Aperture       CubicLaw
Radius         Powerlaw  4.000 0.0385  limits 3.0 28
Location       Poisson
Orientation    Fisher    trend 293.8 plunge 0.0 kappa 21.79
```

```
Intensity      P32       0.0075  # 0.657340071 unscaled
Set 8  # OSM SH2 local
Transmissivity Constant  1e-10
Storativity    Constant  1e-8
Aperture       CubicLaw
Radius         Powerlaw  3.610 0.0385  limits 3.0 28
Location       Poisson
Orientation    Fisher    trend 164.0 plunge 52.6 kappa 35.43
Intensity      P32       0.0042  # 0.080216867 unscaled
Set 9  # OSM SH3 local
Transmissivity Constant  1e-10
Storativity    Constant  1e-8
Aperture       CubicLaw
Radius         Powerlaw  3.610 0.0385 limits 3.0 28
Location       Poisson
Orientation    Fisher    trend 337.9 plunge 52.6 kappa 17.075
Intensity      P32       0.0034  # 0.065706661 unscaled
Set 10  # TFM NE global
Transmissivity Constant  1e-10
Storativity    Constant  1e-8
Aperture       CubicLaw
Radius         Powerlaw  4.000 28 limits 28 564.2
Location       Poisson
Orientation    Fisher    trend 315.3 plunge  1.8 kappa 27.02333
Intensity      P32       0.028510638
Set 11  # TFM NS global
Transmissivity Constant  1e-10
Storativity    Constant  1e-8
Aperture       CubicLaw
Radius         Powerlaw  3.200 28 limits 28 564.2
Location       Poisson
Orientation    Fisher    trend  92.7 plunge  1.2 kappa 30.685
Intensity      P32       0.000338626
Set 12  # TFM NW global
Transmissivity Constant  1e-10
Storativity    Constant  1e-8
Aperture       CubicLaw
Radius         Powerlaw  3.060 28 limits 28 564.2
Location       Poisson
Orientation    Fisher    trend  47.6 plunge  4.4 kappa 19.672
Intensity      P32       0.000255553
Set 13  # TFM SH global
Transmissivity Constant  1e-10
Storativity    Constant  1e-8
Aperture       CubicLaw
Radius         Powerlaw  3.830 28 limits 28 564.2
Location       Poisson
Orientation    Fisher    trend 347.4 plunge 85.6 kappa 23.24625
Intensity      P32       0.028611802
Set 14  # TFM ENE global
Transmissivity Constant  1e-10
Storativity    Constant  1e-8
Aperture       CubicLaw
Radius         Powerlaw  4.140 28 limits 28 564.2
Location       Poisson
Orientation    Fisher    trend 157.9 plunge  4.0 kappa 53.18143
Intensity      P32       0.08706543
Set 15  # TFM EW global
Transmissivity Constant  1e-10
Storativity    Constant  1e-8
Aperture       CubicLaw
Radius         Powerlaw  3.850 28 limits 28 564.2
Location       Poisson
Orientation    Fisher    trend 186.3 plunge  4.3 kappa 34.2325
Intensity      P32       0.001383161
```

GeoFFM06_osm_tfm_o3.sets

```
#
# Forsmark SDM-Site
# GeoDFN fracture sets for FFM06
#
# Fracture geometry statistics (orientation and size distributions)
and global P32 based on:
# SKB TR-21 (Munier, 2010, Update 2013-12) Appendix 3, Table A3.1
(OSM+TCM alternative).
#
# Fracture transmissivity is set to an arbitrary constant value T =
1e-10 m2/s
# to keep things simple for mechanical calculations.
#
Set 1   # OSM NE global
Transmissivity Constant  1e-10
Storativity    Constant  1e-8
Aperture       CubicLaw
Radius         Powerlaw  3.640 0.0385  limits 3.0 28
Location       Poisson
Orientation    Fisher    trend 125.7 plunge 10.10  kappa 45.05
Intensity      P32       0.1523  # 3.251854064 unscaled
Set 2   # OSM NS global
Transmissivity Constant  1e-10
Storativity    Constant  1e-8
Aperture       CubicLaw
Radius         Powerlaw  3.900 0.0385  limits 3.0 28
Location       Poisson
Orientation    Fisher    trend  91.0 plunge 4.1  kappa 19.48667
Intensity      P32       0.0369  # 2.145881617 unscaled
Set 3   # OSM NW global
Transmissivity Constant  1e-10
Storativity    Constant  1e-8
Aperture       CubicLaw
Radius         Powerlaw  3.440 0.0385  limits 3.0 28
Location       Poisson
Orientation    Fisher    trend  34.1  plunge 0.8  kappa 16.13
Intensity      P32       0.1401  # 1.52189537 unscaled
Set 4   # OSM SH global
Transmissivity Constant  1e-10
Storativity    Constant  1e-8
Aperture       CubicLaw
Radius         Powerlaw  3.610 0.0385  limits 3.0 28
Location       Poisson
Orientation    Fisher    trend 84.3 plunge 71.3 kappa 10.77667
Intensity      P32       0.0329  # 0.630457605 unscaled
Set 5  # OSM ENE local
Transmissivity Constant  1e-10
Storativity    Constant  1e-8
Aperture       CubicLaw
Radius         Powerlaw  3.200 0.0385  limits 3.0 28
Location       Poisson
Orientation    Fisher    trend 155.4 plunge 8.3 kappa 20.83
Intensity      P32       0.0214  # 0.142109985 unscaled
Set 6  # OSM SH2 local
Transmissivity Constant  1e-10
Storativity    Constant  1e-8
Aperture       CubicLaw
Radius         Powerlaw  3.610 0.0385  limits 3.0 28
Location       Poisson
Orientation    Fisher    trend   0.0 plunge 47.5 kappa 12.71
Intensity      P32       0.0221  # 0.422914502 unscaled
Set 7  # TFM NE global
Transmissivity Constant  1e-10
Storativity    Constant  1e-8
Aperture       CubicLaw
Radius         Powerlaw  4.000 28 limits 28 564.2
Location       Poisson
Orientation    Fisher    trend 315.3 plunge  1.8 kappa 27.02333
```

```
Intensity      P32       0.028510638
Set 8  # TFM NS global
Transmissivity Constant  1e-10
Storativity    Constant  1e-8
Aperture       CubicLaw
Radius         Powerlaw  3.200 28 limits 28 564.2
Location       Poisson
Orientation    Fisher    trend  92.7 plunge  1.2 kappa 30.685
Intensity      P32       0.000338626
Set 9  # TFM NW global
Transmissivity Constant  1e-10
Storativity    Constant  1e-8
Aperture       CubicLaw
Radius         Powerlaw  3.060 28 limits 28 564.2
Location       Poisson
Orientation    Fisher    trend  47.6 plunge  4.4 kappa 19.672
Intensity      P32       0.000255553
Set 10  # TFM SH global
Transmissivity Constant  1e-10
Storativity    Constant  1e-8
Aperture       CubicLaw
Radius         Powerlaw  3.830 28 limits 28 564.2
Location       Poisson
Orientation    Fisher    trend 347.4 plunge 85.6 kappa 23.24625
Intensity      P32       0.028611802
Set 11  # TFM ENE global
Transmissivity Constant  1e-10
Storativity    Constant  1e-8
Aperture       CubicLaw
Radius         Powerlaw  4.140 28 limits 28 564.2
Location       Poisson
Orientation    Fisher    trend 157.9 plunge  4.0 kappa 53.18143
Intensity      P32       0.08706543
Set 12  # TFM EW global
Transmissivity Constant  1e-10
Storativity    Constant  1e-8
Aperture       CubicLaw
Radius         Powerlaw  3.850 28 limits 28 564.2
Location       Poisson
Orientation    Fisher    trend 186.3 plunge  4.3 kappa 34.2325
Intensity      P32       0.001383161
```

GeoFFM01_osm_tfm_og3.sets

```
#
# Forsmark SDM-Site
# GeoDFN fracture sets for FFM01
#
# Fracture geometry statistics (orientation and size distributions)
and global P32 based on:
# SKB TR-21 (Munier, 2010, Update 2013-12) Appendix 3, Table A3.1
(OSM+TCM alternative).
# Fracture intensity of all sets increased by 25%.
# P32 corrected for increase of rmin to 3.0 m.
#
# Fracture transmissivity is set to an arbitrary constant value T =
1e-10 m2/s
# to keep things simple for mechanical calculations.
#
Set 1   # OSM NE global
Transmissivity Constant  1e-10
Storativity    Constant  1e-8
Aperture       CubicLaw
Radius         Powerlaw  3.640 0.0385  limits 3.0 28
Location       Poisson
Orientation    Fisher    trend 314.9 plunge 1.3  kappa 20.943
Intensity      P32       0.1001 # increased from 0.0800 ( 1.709425143
unscaled )
Set 2   # OSM NS global
```

```
Transmissivity Constant  1e-10
Storativity    Constant  1e-8
Aperture       CubicLaw
Radius         Powerlaw  3.900 0.0385  limits 3.0 28
Location       Poisson
Orientation    Fisher    trend 270.1 plunge 5.3  kappa 21.33938
Intensity      P32       0.0277 # 0.0222  ( 1.289614635 unscaled )
Set 3   # OSM NW global
Transmissivity Constant  1e-10
Storativity    Constant  1e-8
Aperture       CubicLaw
Radius         Powerlaw  3.440 0.0385  limits 3.0 28
Location       Poisson
Orientation    Fisher    trend 230.1  plunge 4.6  kappa 15.70056
Intensity      P32       0.1034 # 0.0827  ( 0.898302275 unscaled )
Set 4   # OSM SH global
Transmissivity Constant  1e-10
Storativity    Constant  1e-8
Aperture       CubicLaw
Radius         Powerlaw  3.610 0.0385  limits 3.0 28
Location       Poisson
Orientation    Fisher    trend 0.8 plunge 87.3 kappa 17.4185
Intensity      P32       0.0401 # 0.0321  ( 0.615018629 unscaled )
Set 5  # OSM ENE local
Transmissivity Constant  1e-10
Storativity    Constant  1e-8
Aperture       CubicLaw
Radius         Powerlaw  3.200 0.0385  limits 3.0 28
Location       Poisson
Orientation    Fisher    trend 157.5 plunge 3.1 kappa 34.11
Intensity      P32       0.0354 # 0.0283  ( 0.187727553 unscaled )
Set 6   # OSM EW local
Transmissivity Constant  1e-10
Storativity    Constant  1e-8
Aperture       CubicLaw
Radius         Powerlaw  4.060 0.0385  limits 3.0 28
Location       Poisson
Orientation    Fisher    trend 0.4 plunge 11.9 kappa 13.89333
Intensity      P32       0.0019 # 0.0015  ( 0.168460531 unscaled )
Set 7  # OSM NNE local
Transmissivity Constant  1e-10
Storativity    Constant  1e-8
Aperture       CubicLaw
Radius         Powerlaw  4.000 0.0385  limits 3.0 28
Location       Poisson
Orientation    Fisher    trend 293.8 plunge 0.0 kappa 21.79
Intensity      P32       0.0094 # 0.0075  ( 0.657340071 unscaled )
Set 8  # OSM SH2 local
Transmissivity Constant  1e-10
Storativity    Constant  1e-8
Aperture       CubicLaw
Radius         Powerlaw  3.610 0.0385  limits 3.0 28
Location       Poisson
Orientation    Fisher    trend 164.0 plunge 52.6 kappa 35.43
Intensity      P32       0.0052 # 0.0042  ( 0.080216867 unscaled )
Set 9  # OSM SH3 local
Transmissivity Constant  1e-10
Storativity    Constant  1e-8
Aperture       CubicLaw
Radius         Powerlaw  3.610 0.0385 limits 3.0 28
Location       Poisson
Orientation    Fisher    trend 337.9 plunge 52.6 kappa 17.075
Intensity      P32       0.0043 # 0.0034  ( 0.065706661 unscaled )
Set 10  # TFM NE global
Transmissivity Constant  1e-10
Storativity    Constant  1e-8
Aperture       CubicLaw
Radius         Powerlaw  4.000 28 limits 28 564.2
Location       Poisson
```

```
Orientation    Fisher    trend 315.3 plunge  1.8 kappa 27.02333
Intensity      P32       0.03564 # 0.028510638
Set 11  # TFM NS global
Transmissivity Constant  1e-10
Storativity    Constant  1e-8
Aperture       CubicLaw
Radius         Powerlaw  3.200 28 limits 28 564.2
Location       Poisson
Orientation    Fisher    trend  92.7 plunge  1.2 kappa 30.685
Intensity      P32       0.000423 # 0.000338626
Set 12  # TFM NW global
Transmissivity Constant  1e-10
Storativity    Constant  1e-8
Aperture       CubicLaw
Radius         Powerlaw  3.060 28 limits 28 564.2
Location       Poisson
Orientation    Fisher    trend  47.6 plunge  4.4 kappa 19.672
Intensity      P32       0.000319 # 0.000255553
Set 13  # TFM SH global
Transmissivity Constant  1e-10
Storativity    Constant  1e-8
Aperture       CubicLaw
Radius         Powerlaw  3.830 28 limits 28 564.2
Location       Poisson
Orientation    Fisher    trend 347.4 plunge 85.6 kappa 23.24625
Intensity      P32       0.03576 # 0.028611802
Set 14  # TFM ENE global
Transmissivity Constant  1e-10
Storativity    Constant  1e-8
Aperture       CubicLaw
Radius         Powerlaw  4.140 28 limits 28 564.2
Location       Poisson
Orientation    Fisher    trend 157.9 plunge  4.0 kappa 53.18143
Intensity      P32       0.10883 # 0.08706543
Set 15  # TFM EW global
Transmissivity Constant  1e-10
Storativity    Constant  1e-8
Aperture       CubicLaw
Radius         Powerlaw  3.850 28 limits 28 564.2
Location       Poisson
Orientation    Fisher    trend 186.3 plunge  4.3 kappa 34.2325
Intensity      P32       0.001729 # 0.001383161
```

GeoFFM06_osm_tfm_og3.sets

```
#
# Forsmark SDM-Site
# GeoDFN fracture sets for FFM06
#
# Fracture geometry statistics (orientation and size distributions)
and global P32 based on:
# SKB TR-21 (Munier, 2010, Update 2013-12) Appendix 3, Table A3.1
(OSM+TCM alternative).
# Fracture intensity for all sets increased by 25%.
# P32 corrected for change of rmin to 3.0 m (from 1.5 m).
#
# Fracture transmissivity is set to an arbitrary constant value T =
1e-10 m2/s
# to keep things simple for mechanical calculations.
#
Set 1   # OSM NE global
Transmissivity Constant  1e-10
Storativity    Constant  1e-8
Aperture       CubicLaw
Radius         Powerlaw  3.640 0.0385  limits 3.0 28
Location       Poisson
Orientation    Fisher    trend 125.7 plunge 10.10  kappa 45.05
Intensity      P32       0.1903 # 0.1523  ( 3.251854064 unscaled )
Set 2   # OSM NS global
```

```
Transmissivity Constant  1e-10
Storativity    Constant  1e-8
Aperture       CubicLaw
Radius         Powerlaw  3.900 0.0385  limits 3.0 28
Location       Poisson
Orientation    Fisher    trend  91.0 plunge 4.1  kappa 19.48667
Intensity      P32       0.0461 # 0.0369  ( 2.145881617 unscaled )
Set 3   # OSM NW global
Transmissivity Constant  1e-10
Storativity    Constant  1e-8
Aperture       CubicLaw
Radius         Powerlaw  3.440 0.0385  limits 3.0 28
Location       Poisson
Orientation    Fisher    trend  34.1  plunge 0.8  kappa 16.13
Intensity      P32       0.1751 # 0.1401  ( 1.52189537 unscaled )
Set 4   # OSM SH global
Transmissivity Constant  1e-10
Storativity    Constant  1e-8
Aperture       CubicLaw
Radius         Powerlaw  3.610 0.0385  limits 3.0 28
Location       Poisson
Orientation    Fisher    trend 84.3 plunge 71.3 kappa 10.77667
Intensity      P32       0.0411 # 0.0329  ( 0.630457605 unscaled )
Set 5  # OSM ENE local
Transmissivity Constant  1e-10
Storativity    Constant  1e-8
Aperture       CubicLaw
Radius         Powerlaw  3.200 0.0385  limits 3.0 28
Location       Poisson
Orientation    Fisher    trend 155.4 plunge 8.3 kappa 20.83
Intensity      P32       0.0268 # 0.0214  ( 0.142109985 unscaled )
Set 6  # OSM SH2 local
Transmissivity Constant  1e-10
Storativity    Constant  1e-8
Aperture       CubicLaw
Radius         Powerlaw  3.610 0.0385  limits 3.0 28
Location       Poisson
Orientation    Fisher    trend   0.0 plunge 47.5 kappa 12.71
Intensity      P32       0.0276 # 0.0221  ( 0.422914502 unscaled )
Set 7  # TFM NE global
Transmissivity Constant  1e-10
Storativity    Constant  1e-8
Aperture       CubicLaw
Radius         Powerlaw  4.000 28 limits 28 564.2
Location       Poisson
Orientation    Fisher    trend 315.3 plunge  1.8 kappa 27.02333
Intensity      P32       0.03564 # 0.028510638
Set 8  # TFM NS global
Transmissivity Constant  1e-10
Storativity    Constant  1e-8
Aperture       CubicLaw
Radius         Powerlaw  3.200 28 limits 28 564.2
Location       Poisson
Orientation    Fisher    trend  92.7 plunge  1.2 kappa 30.685
Intensity      P32       0.000423 # 0.000338626
Set 9  # TFM NW global
Transmissivity Constant  1e-10
Storativity    Constant  1e-8
Aperture       CubicLaw
Radius         Powerlaw  3.060 28 limits 28 564.2
Location       Poisson
Orientation    Fisher    trend  47.6 plunge  4.4 kappa 19.672
Intensity      P32       0.0003194 # 0.000255553
Set 10  # TFM SH global
Transmissivity Constant  1e-10
Storativity    Constant  1e-8
Aperture       CubicLaw
Radius         Powerlaw  3.830 28 limits 28 564.2
Location       Poisson
```

```
Orientation    Fisher    trend 347.4 plunge 85.6 kappa 23.24625
Intensity      P32       0.03576 # 0.028611802
Set 11  # TFM ENE global
Transmissivity Constant  1e-10
Storativity    Constant  1e-8
Aperture       CubicLaw
Radius         Powerlaw  4.140 28 limits 28 564.2
Location       Poisson
Orientation    Fisher    trend 157.9 plunge  4.0 kappa 53.18143
Intensity      P32       0.1088 # 0.08706543
Set 12  # TFM EW global
Transmissivity Constant  1e-10
Storativity    Constant  1e-8
Aperture       CubicLaw
Radius         Powerlaw  3.850 28 limits 28 564.2
Location       Poisson
Orientation    Fisher    trend 186.3 plunge  4.3 kappa 34.2325
Intensity      P32       0.00173 # 0.001383161
```

GeoFFM01_tcm_t2.sets

```
#
# Forsmark SDM-Site
# GeoDFN fracture sets for FFM01
#
# Fracture geometry statistics (orientation and size distributions)
and global P32 based on:
# SKB TR-21 (Munier, 2010) Appendix 3, Table A3.1 (TCM alternative).
#
# the number of fractures to a manageable level. The minimum fracture
radius that can produce
# an FPI with a 4.2 m x 4.8 m deposition tunnel is:
#          r_min = sqrt((2.1 m)^2 + (2.4 m)^2) ~ 3.189 m
#
# Fracture transmissivity is set to an arbitrary constant value T =
1e-10 m2/s
# to keep things simple for mechanical calculations.
#
Set 1   # NE global
Transmissivity Constant  1e-10
Storativity    Constant  1e-8
Aperture       CubicLaw
Radius         Powerlaw  4.020 0.659171  limits 3.0 564.2
Location       Poisson
Orientation    Fisher    trend 314.9 plunge 1.3  kappa 20.943
Intensity      P32       1.733229012 unscaled
Set 2   # NS global
Transmissivity Constant  1e-10
Storativity    Constant  1e-8
Aperture       CubicLaw
Radius         Powerlaw  3.780 0.059256  limits 3.0 564.2
Location       Poisson
Orientation    Fisher    trend 270.1 plunge 5.3  kappa 21.33938
Intensity      P32       1.292080834 unscaled
Set 3   # NW global
Transmissivity Constant  1e-10
Storativity    Constant  1e-8
Aperture       CubicLaw
Radius         Powerlaw  3.850 0.59368  limits 3.0 564.2
Location       Poisson
Orientation    Fisher    trend 230.1  plunge 4.6  kappa 15.70056
Intensity      P32       0.947802313 unscaled
Set 4   # SH global
Transmissivity Constant  1e-10
Storativity    Constant  1e-8
Aperture       CubicLaw
Radius         Powerlaw  3.850 0.816285  limits 3.0 564.2
Location       Poisson
Orientation    Fisher    trend 0.8 plunge 87.3 kappa 17.4185
```

```
Intensity      P32       0.623883816 unscaled
Set 5  # ENE local
Transmissivity Constant  1e-10
Storativity    Constant  1e-8
Aperture       CubicLaw
Radius         Powerlaw  4.250 0.32488  limits 3.0 564.2
Location       Poisson
Orientation    Fisher    trend 157.5 plunge 3.1 kappa 34.11
Intensity      P32       0.256333102 unscaled
Set 6   # EW local
Transmissivity Constant  1e-10
Storativity    Constant  1e-8
Aperture       CubicLaw
Radius         Powerlaw  4.100 0.17  limits 3.0 564.2
Location       Poisson
Orientation    Fisher    trend 0.4 plunge 11.9 kappa 13.89333
Intensity      P32       0.168594082 unscaled
Set 7  # NNE local
Transmissivity Constant  1e-10
Storativity    Constant  1e-8
Aperture       CubicLaw
Radius         Powerlaw  4.000 0.0385  limits 3.0 564.2
Location       Poisson
Orientation    Fisher    trend 293.8 plunge 0.0 kappa 21.79
Intensity      P32       0.658245158 unscaled
Set 8  # SH2 local
Transmissivity Constant  1e-10
Storativity    Constant  1e-8
Aperture       CubicLaw
Radius         Powerlaw  3.610 0.0385  limits 3.0 564.2
Location       Poisson
Orientation    Fisher    trend 164.0 plunge 52.6 kappa 35.43
Intensity      P32       0.081168411 unscaled
Set 9  # SH3 local
Transmissivity Constant  1e-10
Storativity    Constant  1e-8
Aperture       CubicLaw
Radius         Powerlaw  3.610 0.0385  limits 3.0 564.2
Location       Poisson
Orientation    Fisher    trend 337.9 plunge 52.9 kappa 17.075
Intensity      P32       0.066908499 unscaled
```

GeoFFM06_tcm_t2.sets

```
#
# Forsmark SDM-Site
# GeoDFN fracture sets for FFM06
#
# Fracture geometry statistics (orientation and size distributions)
and global P32 based on:
# SKB TR-21 (Munier, 2010) Appendix 3, Table A3.1 (TCM alternative).
#
# the number of fractures to a manageable level. The minimum fracture
radius that can produce
# an FPI with a 4.2 m x 4.8 m deposition tunnel is:
#          r_min = sqrt((2.1 m)^2 + (2.4 m)^2) ~ 3.189 m
#
# Fracture transmissivity is set to an arbitrary constant value T =
1e-10 m2/s
# to keep things simple for mechanical calculations.
#
Set 1   # NE global
Transmissivity Constant  1e-10
Storativity    Constant  1e-8
Aperture       CubicLaw
Radius         Powerlaw  4.020 0.350908  limits 3.0 564.2
Location       Poisson
Orientation    Fisher    trend 125.7 plunge 10.10  kappa 45.05
Intensity      P32       3.298729012 unscaled
```

```
Set 2   # NS global
Transmissivity Constant  1e-10
Storativity    Constant  1e-8
Aperture       CubicLaw
Radius         Powerlaw  3.780 0.0385  limits 3.0 564.2
Location       Poisson
Orientation    Fisher    trend  91.0 plunge 4.1  kappa 19.48667
Intensity      P32       2.150388557 unscaled
Set 3   # NW global
Transmissivity Constant  1e-10
Storativity    Constant  1e-8
Aperture       CubicLaw
Radius         Powerlaw  3.850 0.319266  limits 3.0 564.2
Location       Poisson
Orientation    Fisher    trend  34.1  plunge 0.8  kappa 16.13
Intensity      P32       1.607802313 unscaled
Set 4   # SH global
Transmissivity Constant  1e-10
Storativity    Constant  1e-8
Aperture       CubicLaw
Radius         Powerlaw  3.850 0.792852  limits 3.0 564.2
Location       Poisson
Orientation    Fisher    trend 84.3 plunge 71.3 kappa 10.77667
Intensity      P32       0.639583816 unscaled
Set 5  # ENE local
Transmissivity Constant  1e-10
Storativity    Constant  1e-8
Aperture       CubicLaw
Radius         Powerlaw  4.250 0.74  limits 3.0 564.2
Location       Poisson
Orientation    Fisher    trend 155.4 plunge 8.3 kappa 20.83
Intensity      P32       0.194005885 unscaled
Set 6  # SH2 local
Transmissivity Constant  1e-10
Storativity    Constant  1e-8
Aperture       CubicLaw
Radius         Powerlaw  3.610 0.0385  limits 3.0 564.2
Location       Poisson
Orientation    Fisher    trend   0.0 plunge 47.5 kappa 12.71
Intensity      P32       0.429411556 unscaled
```

GeoFFM01_tcm_tg2.sets

```
#
# Forsmark SDM-Site
# GeoDFN fracture sets for FFM01
#
# Fracture geometry statistics (orientation and size distributions)
and global P32 based on:
# SKB TR-21 (Munier, 2010) Appendix 3, Table A3.1 (TCM alternative).
#
# the number of fractures to a manageable level. The minimum fracture
radius that can produce
# an FPI with a 4.2 m x 4.8 m deposition tunnel is:
#          r_min = sqrt((2.1 m)^2 + (2.4 m)^2) ~ 3.189 m
#
# Fracture transmissivity is set to an arbitrary constant value T =
1e-10 m2/s
# to keep things simple for mechanical calculations.
#
Set 1   # NE global
Transmissivity Constant  1e-10
Storativity    Constant  1e-8
Aperture       CubicLaw
Radius         Powerlaw  4.020 0.659171  limits 3.0 564.2
Location       Poisson
Orientation    Fisher    trend 314.9 plunge 1.3  kappa 20.943
Intensity      P32       2.1665 unscaled # 1.733229012 unscaled
Set 2   # NS global
```

```
Transmissivity Constant  1e-10
Storativity    Constant  1e-8
Aperture       CubicLaw
Radius         Powerlaw  3.780 0.059256  limits 3.0 564.2
Location       Poisson
Orientation    Fisher    trend 270.1 plunge 5.3  kappa 21.33938
Intensity      P32       1.6151 unscaled # 1.292080834 unscaled
Set 3   # NW global
Transmissivity Constant  1e-10
Storativity    Constant  1e-8
Aperture       CubicLaw
Radius         Powerlaw  3.850 0.59368  limits 3.0 564.2
Location       Poisson
Orientation    Fisher    trend 230.1  plunge 4.6  kappa 15.70056
Intensity      P32       1.1848 unscaled # 0.947802313 unscaled
Set 4   # SH global
Transmissivity Constant  1e-10
Storativity    Constant  1e-8
Aperture       CubicLaw
Radius         Powerlaw  3.850 0.816285  limits 3.0 564.2
Location       Poisson
Orientation    Fisher    trend 0.8 plunge 87.3 kappa 17.4185
Intensity      P32       0.7799 unscaled # 0.623883816 unscaled
Set 5  # ENE local
Transmissivity Constant  1e-10
Storativity    Constant  1e-8
Aperture       CubicLaw
Radius         Powerlaw  4.250 0.32488  limits 3.0 564.2
Location       Poisson
Orientation    Fisher    trend 157.5 plunge 3.1 kappa 34.11
Intensity      P32       0.3204 unscaled # 0.256333102 unscaled
Set 6   # EW local
Transmissivity Constant  1e-10
Storativity    Constant  1e-8
Aperture       CubicLaw
Radius         Powerlaw  4.100 0.17  limits 3.0 564.2
Location       Poisson
Orientation    Fisher    trend 0.4 plunge 11.9 kappa 13.89333
Intensity      P32       0.2107 unscaled # 0.168594082 unscaled
Set 7  # NNE local
Transmissivity Constant  1e-10
Storativity    Constant  1e-8
Aperture       CubicLaw
Radius         Powerlaw  4.000 0.0385  limits 3.0 564.2
Location       Poisson
Orientation    Fisher    trend 293.8 plunge 0.0 kappa 21.79
Intensity      P32       0.8228 unscaled # 0.658245158 unscaled
Set 8  # SH2 local
Transmissivity Constant  1e-10
Storativity    Constant  1e-8
Aperture       CubicLaw
Radius         Powerlaw  3.610 0.0385  limits 3.0 564.2
Location       Poisson
Orientation    Fisher    trend 164.0 plunge 52.6 kappa 35.43
Intensity      P32       0.1015 unscaled # 0.081168411 unscaled
Set 9  # SH3 local
Transmissivity Constant  1e-10
Storativity    Constant  1e-8
Aperture       CubicLaw
Radius         Powerlaw  3.610 0.0385  limits 3.0 564.2
Location       Poisson
Orientation    Fisher    trend 337.9 plunge 52.9 kappa 17.075
Intensity      P32       0.0836 unscaled # 0.066908499 unscaled
```

GeoFFM06_tcm_tg2.sets

```
#
# Forsmark SDM-Site
# GeoDFN fracture sets for FFM06
```

```
#
# Fracture geometry statistics (orientation and size distributions)
and global P32 based on:
# SKB TR-21 (Munier, 2010) Appendix 3, Table A3.1 (TCM alternative).
#
# the number of fractures to a manageable level. The minimum fracture
radius that can produce
# an FPI with a 4.2 m x 4.8 m deposition tunnel is:
#          r_min = sqrt((2.1 m)^2 + (2.4 m)^2) ~ 3.189 m
#
# Fracture transmissivity is set to an arbitrary constant value T =
1e-10 m2/s
# to keep things simple for mechanical calculations.
#
Set 1   # NE global
Transmissivity Constant  1e-10
Storativity    Constant  1e-8
Aperture       CubicLaw
Radius         Powerlaw  4.020 0.350908  limits 3.0 564.2
Location       Poisson
Orientation    Fisher    trend 125.7 plunge 10.10  kappa 45.05
Intensity      P32       4.1234 unscaled # 3.298729012 unscaled
Set 2   # NS global
Transmissivity Constant  1e-10
Storativity    Constant  1e-8
Aperture       CubicLaw
Radius         Powerlaw  3.780 0.0385  limits 3.0 564.2
Location       Poisson
Orientation    Fisher    trend  91.0 plunge 4.1  kappa 19.48667
Intensity      P32       2.6880 unscaled # 2.150388557 unscaled
Set 3   # NW global
Transmissivity Constant  1e-10
Storativity    Constant  1e-8
Aperture       CubicLaw
Radius         Powerlaw  3.850 0.319266  limits 3.0 564.2
Location       Poisson
Orientation    Fisher    trend  34.1  plunge 0.8  kappa 16.13
Intensity      P32       2.0098 unscaled # 1.607802313 unscaled
Set 4   # SH global
Transmissivity Constant  1e-10
Storativity    Constant  1e-8
Aperture       CubicLaw
Radius         Powerlaw  3.850 0.792852  limits 3.0 564.2
Location       Poisson
Orientation    Fisher    trend 84.3 plunge 71.3 kappa 10.77667
Intensity      P32       0.7995 unscaled # 0.639583816 unscaled
Set 5  # ENE local
Transmissivity Constant  1e-10
Storativity    Constant  1e-8
Aperture       CubicLaw
Radius         Powerlaw  4.250 0.74  limits 3.0 564.2
Location       Poisson
Orientation    Fisher    trend 155.4 plunge 8.3 kappa 20.83
Intensity      P32       0.2425 unscaled # 0.194005885 unscaled
Set 6  # SH2 local
Transmissivity Constant  1e-10
Storativity    Constant  1e-8
Aperture       CubicLaw
Radius         Powerlaw  3.610 0.0385  limits 3.0 564.2
Location       Poisson
Orientation    Fisher    trend   0.0 plunge 47.5 kappa 12.71
Intensity      P32       0.5368 unscaled # 0.429411556 unscaled
```

Fracture generation site file

This file gives coordinates of the polygon enclosing the repository panels, used for selective thinning of fractures depending on distance from the repository. The coordinates are listed on a single line in the file, but are broken into separate lines here for formatting reasons.

SDMForsmark468m.sites

```
1 1631494.491 6699011.951 -468.0 1632390.638 6699162.226 -468.0
1633001.496 6699569.101 -468.0 1633073.362 6699616.969 -468.0
1633109.295 6699640.903 -468.0 1633176.199 6699692.145 -468.0
1633062.694 6699969.140 -468.0 1631820.032 6700899.004 -468.0
1631507.288 6701011.570 -468.0 1631340.565 6701070.368 -468.0
1631256.586 6701077.247 -468.0 1631207.877 6701061.226 -468.0
1631034.488 6700935.516 -468.0 1631007.275 6700905.522 -468.0
1630610.101 6700316.385 -468.0 1630593.079 6700272.255 -468.0
1630596.044 6700118.369 -468.0 1630605.622 6700053.116 -468.0
1630620.532 6699951.544 -468.0 1630631.915 6699874.000 -468.0
1630639.640 6699835.132 -468.0 1630665.494 6699705.050 -468.0
1630720.592 6699560.636 -468.0 1630766.921 6699439.206 -468.0
1630898.672 6699310.317 -468.0 1631430.264 6699017.822 -468.0
```

Fracture generation shells file

This file lists threshold values of fracture radius and transmissivity for the fracture generation shells, used for used for selective thinning of fractures depending on distance from the repository.

Forsmark_Ncrit0.shells

```
Shell 1 50000 10000   1e+10
Shell 2   500   100   1e-12
Shell 3   200    50   1e-12
Shell 4   100    20   1e-12
Shell 5    50    10   1e-12
Shell 6    20     5   1e-12
Shell 7    10     2.5 1e-12
Shell 8     5     1.5 1e-12
```

Check of fracture intensities

The check of fracture intensities makes use of the script calc_zone_p32.awk, as listed below. This and other scripts with the suffix ".awk" are written in the AWK programming language (Aho et al., 1988), and executed using GNU Awk Version 3.1.8 (www.gnu.org, 2010).

calc_zone_p32_pdf.awk

```
function acos( x,    c )
{
   if( x == 0 )
      c = PI/2;
   else
   {
      c = sqrt( 1-x*x )/x;
      c = atan2( c,1 );
      if( x < 0 ) c = PI + c;
   }
   return( c );
}
function atan( x )
{
   return( atan2( x,1 ) );
}
function asin( x )
{
   return( PI_2 - acos( x ) );
}
#
# Calculate the area of the segment of a circle of radius r, and cut
off from the rest of the
# circle by a chord which is a distance r-h from the center of the
circle. Note that this formula
# works for h>r up to a value of h = 2r.
#
function area_circle_segment( r,h,   a,theta )
{
   if( h>=2*r )
      a = PI*r*r;
   else if( h>0 )
   {
      theta = 2*acos( (r-h)/r );
      a = 0.5*( theta - sin( theta ) )*r*r;
   }
   else
      a = 0;
   return( a );
}
function disk_area_below( z,zm,r,H,   A )
{
   if( z<zm ) # Disk center is below zm.
   {
      A = PI*r*r;
      if( z+H > zm ) # Note that this excludes the case z = 0.
      {
         h = z+H - zm; # Find how far disk sticks up above zm.
         h *= r/H;     # Correct for dip angle.
         A -= area_circle_segment( r,h );
      }
   }
   else if( z-H < zm )
   {
      h = zm - (z-H); # Find how far disk sticks down below zm.
      h *= r/H;     # Correct for dip angle.
      A = area_circle_segment( r,h );
```

```
   }
   return( A );
}
function find_bin( r,   i )
{
   for( i=0; i<nbins; i++ )
      if( r<rbin[i] ) return( i );
   return( nbins );
}
BEGIN {
   PI_2 = atan2(1,0);
   PI   = 2*PI_2;
   zmin = -475;
   zmax = -460;
   V    = AREA * ( zmax-zmin );
   bin_factor = sqrt( sqrt( 10 ) );
   nbins = 0;
   for( r=0.01; r<=1000; r *= bin_factor )
   {
      rbin[nbins] = r;
      Abin[nbins] = 0;
      nbins++;
   }
   rbin[nbins] = 10000;
   Abin[nbins] = 0;
}
{
   z = $4;
   r = $5;
   dip = $10;
   H = r * sin( dip * PI/180 );        # Half of the disk height after
accounting for tilt.
   if( z+H <= zmin || z-H >= zmax )    # Disk is entirely below zmin
or entirely above zmax.
      A = 0;
   else
   {
      A = disk_area_below( z,zmax,r,H );
      if( A>0 )
         A -= disk_area_below( z,zmin,r,H );
   }
#  printf( "%7.3f %9.3f %7.3f %7.3f %5.1f\n",r,A,H,z,dip );
   nbin = find_bin( r );
   Abin[nbin] += A;
}
END {
   printf( "r_min(m) r_max(m)    P32(m2/m3)\n" );
   for( i=1; i<=nbins; i++ )
      printf( "%8.2f %8.2f  %12.6f\n",rbin[i-1],rbin[i],Abin[i]/V );
}
```

A2.2 Repository simulation

Repository simulations were produced for each calculation case and realization by running the Linux C shell script "SRGeoPFC_repository_v4" as listed below. The script takes two command-line arguments: (1) the calculation case (r3, o3, t2, rg2, og3, or tg2), and (2) the realization number (01, 02, …, 10). The script runs the DFM-*repository* module:

> *repository* (version 2.4.1.1, executable repository2411 compiled February 17, 2014)

The key input files are the tunnel-parameters file SRGeoPFCv2.tunnelpars as listed below, and the tunnel axes coordinates ForsmarkD2.tunnels (too long to list here).

SRGeoPFC_repository_v4

```
#!/bin/csh -f
 nohup
 if( "blank$2" == "blank" ) then
    echo "Syntax: SRSite_repository opt seed"
    echo "where"
    echo "   opt = v1|..."
    echo "   seed= 01,02,...
    exit
 endif
 set STEM = "SRGeoPFC_${1}_${2}"
 repository2411 -lp ../FMcritical3/${STEM}_fracs.pan -wp
${STEM}_repos.pan -rx ${STEM}.fxd SRGeoPFCv2.tunnelpars
ForsmarkD2.tunnels 4 1e-6 1 > $STEM.repos_log
```

SRGeoPFCv2.tunnelpars

```
# Tunnel system parameters:
Scale  1 m
Origin 0 0
Tunnel sides 4
Tunnel floor -465 m
# Tunnel system parameters based on SR-Can for access tunnels, and
Munier (2010) Figure 7-1 for deposition tunnels:
Access tunnel height 7 m
Access tunnel width  7 m
# Deposition tunnel nominal dimensions checked vs. TR-10-18, Figure 2-
2, p. 24, and TR-10-21 Figure 7-1, p. 62.
Deposition tunnel width  4.2 m
Deposition tunnel height 4.8 m
Deposition tunnel spacing 40 m  # NOT USED
# The following DRZ parameters do not affect Ncrit calculations;
relevant only for DFM model construction.
DRZ thickness      1 m
DRZ transmissivity 1e-08 m2/s   # Reference design assumption.
DRZ storativity    1e-08        # Arbitrary value not used.
DRZ aperture       2e-05 m      # Arbitrary value; adjust if needed
for transport.
# Deposition hole parameters checked vs. TR-10-21, Figure 7-1, p. 62.
Deposition hole sides  6     # Relevant only for DFM model
construction.
Deposition hole radius 0.875 # TR-10-18, Figure 2-1, p. 23 gives
deposition hole diameter = 1.75 m.
Deposition hole depth  7.833 # Consistent with TR-10-18 Fig 2-1 & 5-2,
if bottom plate thickness is included.
Canister radius        0.525 # TR-10-52, Figure 4-1, p. 124 gives
canister diameter = 1.050 m.
```

```
Canister length        4.835 # Length of copper shell portion in TR-
10-14 Table 3-6; note implied TR-10-18 Fig 2-1 dimension of 4.48 m not
consistent.
Canister top           2.75  # TR-10-18 notch dimensions in Fig 5.2
(1.25 m deep) plus buffer thickness above canister in Table 2-2 (1.5
m).
#                            Note that this is increased from value
of 2.5 m for SR-Can.
# Deposition hole criteria as for SR-Can, spacing based on Munier
(2010) p. 62:
Utilization fraction      1
Distance between holes    6.0    # Value for RD 29 per TR-10-21 p.62;
note value given by same reference for RD 45 is 6.8.
#                                # Parameters concerning tunnel ends
are based on TR-10-21 Figure 4-9.
Distance from drift end   15     # Note this is less than value of 20
m used for SR-Can.
Distance from drift start 18.5   # Includes additional 3.5 m at start
of tunnel since DFM tunnel coordinates start at access tunnel axis.
Minimum step distance     1      # Step size of 1 m judged to be
"adequate" (TR-10-21, p. 44, Section 5.10)
Pilot hole transmissivity 1 m2/s # Value higher than higher than any
possible fracture transmissivity used to disable pilot-hole criterion.
Pilot hole diameter       0.05   # NOT USED
Pilot hole seepage        1e-06  # NOT USED
Pilot hole bradius        5      # NOT USED
Pilot hole bhead          20     # NOT USED
Maximum intersected holes 4      # If 5 or more trial positions are
intersected by a deposition hole, reject all of these with canister
intersections.
EFPC detections strict           # EFPC fractures are detectable only
if they make a full FPI with deposition hole
EFPC intersections canister      # Only exclude hole positions
intersected by EFPC fracture if canister is intersected.
FPI intersections canister       # Only exclude hole positions
intersected by FPI fracture if canister is intersected; corresponds to
TR-10-21 Fig 3-1b.
```

A2.3 Calculation of critical fracture intersections

Distances from fracture-deposition hole intersections to deformation zones

The Linux C shell script SRGeoPFC_calcdists_v3 was used to set up and run the DFM-*pancalc* module:

> *pancalc* (version 2.4.1.1, executable pancalc2411 compiled February 17, 2014)

to find the 3D distance from each fracture-deposition hole intersection (as listed in the fxd file for the calculation case and realization) to each of the seven deformation zones considered as structures that could potentially host earthquakes. This script is listed below, followed by three subordinate scripts:

> condense_fxd.awk
> extract_distances.awk
> append_distances.awk

which are written in the AWK programming language.

SRGeoPFC_calcdists_v3

```
#!/bin/csh -f
 nohup
 if( "blank$2" == "blank" ) then
    echo "Syntax: SRGeoPFC_calcdists_v3 opt seed"
    echo "where"
    echo "   opt = v1|..."
    echo "   seed= 01,02,..."
    exit
 endif
 set STEM = "SRGeoPFC_${1}_${2}"
 set FXD  = "../FMcrit_repo3/${STEM}.fxd"
 if ( -f $FXD ) then
    awk -f condense_fxd.awk $FXD | sort | uniq > $STEM.pts
    set FILES
    foreach DZ (ENE0060A ENE0062A NW0017 NW1200 WNW0123 WNW0809A A2 )
       set DZFILE="DZs/ZFM${DZ}.pan"
       set DIST="Distances/${STEM}_${DZ}.dists"
       if( -f $DZFILE ) then
          if( !( -f $DIST ) ) then
             pancalc2411 $DZFILE ${STEM}.pts > $DIST
          endif
          awk -f extract_distances.awk -v DZ=$DZ $DIST > ${DZ}.tmp
          set FILES="$FILES ${DZ}.tmp"
       else
          echo "$DZFILE not found."
          exit
       endif
    end
    paste $FILES > distances.tmp
    awk -f append_distances.awk distances.tmp
../FMcrit_repo3/${STEM}.fxd > $STEM.fxdd
    rm -f ${STEM}.pts
    rm *.tmp
 endif
```

condense_fxd.awk

```
BEGIN {
   pan0 = 0;
}
{
   if( NR>1 )
   {
      pan = $1;
      if( pan != pan0 )
      {
         printf( "%s %s %s %s\n",$1,$4,$5,$6 );
      }
      pan0 = pan;
   }
}
```

extract_distances.awk

```
BEGIN {
   TRUE = 0==0;
   FALSE=!TRUE;
   reading_header = TRUE;
   print "Panel " DZ;
}
{
   if( reading_header )
   {
   #  print "Reading header line" $0;
      if( $1 == "ID" ) reading_header = FALSE;
   }
   else
      print $1 " " $5;
}
```

append_distances.awk

```
BEGIN {
   TRUE = 0==0;
   FALSE=!TRUE;
   reading_distances = TRUE;
}
{
   if( FNR==NR ) # Reading distances.
   {
      if( NR==1 )
      {
         nzones = NF/2;
         for( i=0; i<nzones; i++ ) zone_name[i] = $(2*i+2);
      }
      else
      {
         pan = $1;
         for( i=0; i<nzones; i++ ) distance[pan,i] = $(2*i+2);
      }
   }
   else
   {
      if( FNR==1 )
      {
         printf( "%s",$0 );
         for( i=0; i<nzones; i++ ) printf( " %8s",zone_name[i] );
         printf( "\n" );
      }
      else
      {
         pan = $1;
         printf( "%s",$0 );
         for( i=0; i<nzones; i++ ) printf( " %8s",distance[pan,i] );
         printf( "\n" );
      }
   }
}
```

Identification of critical fractures

Critical fractures are identified by running the Linux script *idfracs_all* which automatically sets up and runs the AWK language script, *identify_critical_fractures.awk* to classify intersections in terms of the categories specified by Munier (2010). These two scripts are listed below.

idfracs_all

```
#!/bin/csh -f
#
foreach CASE ( r3 o3 t2 rg2 og3 tg2 )
   rm -f ncritical_${CASE}.prn
   if ( $CASE == "o3" || $CASE == "og3" ) then
      set TITLE = "Case: OSM-TFM ($CASE)"
   else if ( $CASE == "r3" || $CASE == "rg2" ) then
      set TITLE = "Case: r0-fixed ($CASE)"
   else if ( $CASE == "t2" || $CASE == "tg2" ) then
      set TITLE = "Case: TFM ($CASE)"
   endif
   foreach N ( 01 02 03 04 05 06 07 08 09 10 )
      awk -f identify_critical_fractures.awk SRGeoPFC_${CASE}_$N.fxdd
> SRGeoPFC_${CASE}_$N.cfs
      echo "$TITLE Realization $N"
      echo "$TITLE Realization $N"    >> ncritical_${CASE}.prn
      tail -5 SRGeoPFC_${CASE}_$N.cfs
      tail -5 SRGeoPFC_${CASE}_$N.cfs >> ncritical_${CASE}.prn
   end
end
```

identify_critical_fractures.awk

```
function acos( x,    c )
{
   if( x == 0 )
      c = PI/2;
   else
   {
      c = sqrt( 1-x*x )/x;
      c = atan2( c,1 );
      if( x < 0 ) c = PI + c;
   }
   return( c );
}
function distance_between_points( a,b,     i,d,rr )
{
   rr = 0;
   for( i=0; i<3; i++ )
   {
      d = a[i] - b[i];
      rr += d*d;
   }
   return( sqrt( rr ) );
}
function set_length_categories()
{
   length_category["ZFMENE0060A"] = 3; # Note always stable per TR-10-
21 Figure 7-3.
   length_category["ZFMENE0062A"] = 3; # Note always stable per TR-10-
21 Figure 7-3.
   length_category["ZFMNW0017"]   = 5;
   length_category["ZFMNW1200"]   = 3;
   length_category["ZFMWNW0123"]  = 5;
   length_category["ZFMWNW0809A"] = 3;
   length_category["ZFMA2"]       = 3;
}
```

```
function critical_radius( length_cat,dip,distance,   rc )
{
#  Lookup function based on Table 7-2 of SKB TR-10-21.
#
#  printf( "\nDEBUG: length_cat %d dip %2d distance
%9.3f\n",length_cat,dip,distance );
#
   if( length_cat==5 ) # Deformation zone longer than 5 km.
   {
      if( dip<55 ) # Dip angle in range 0-55 degrees
      {
         if( distance<100 )      # This should never happen if layout
avoids deformation zones.
            rc = 0;
         else if( distance<200 ) # >5 0-55 100-200 62.5
            rc = 62.5;
         else if( distance<400 ) # >5 0-55 200-400 125
            rc = 125;
         else if( distance<600 ) # >5 0-55 400-600 160
            rc = 160;
         else                    # >5 0-55 >600 225
            rc = 225;
      }
      else         # Dip angle in range 55-90 degrees.
      {
         if( distance<100 )      # This should never happen if layout
avoids deformation zones.
            rc = 0;
         else if( distance<200 ) # >5 55-90 100-200 85
            rc = 85;
         else if( distance<400 ) # >5 55-90 200-400 170
            rc = 170;
         else if( distance<600 ) # >5 55-90 400-600 215
            rc = 215;
         else                    # >5 55-90 >600 >300
            rc = 300;
      }
   }
   else if( length_cat==3 ) # Deformation zone in 3-5 km range.
   {
      if( dip<55 ) # Dip angle in range 0-55 degrees
      {
         if( distance<100 )      # This should never happen if layout
avoids deformation zones.
            rc = 0;
         else if( distance<200 ) # 3-5 0-55 100-200 75
            rc = 75;
         else if( distance<400 ) # 3-5 0-55 200-400 150
            rc = 150;
         else if( distance<600 ) # 3-5 0-55 400-600 235
            rc = 235;
         else                    # 3-5 0-55 >600 >300
            rc = 300;
      }
      else         # Dip angle in range 55-90 degrees.
      {
         if( distance<100 )      # This should never happen if layout
avoids deformation zones.
            rc = 0;
         else if( distance<200 ) # 3-5 55-90 100-200 100
            rc = 100;
         else if( distance<400 ) # 3-5 55-90 200-400 200
            rc = 200;
         else if( distance<600 ) # 3-5 55-90 400-600 >300
            rc = 300;
         else                    # 3-5 55-90 >600 >>300
            rc = 400;            # Unclear how large value should be.
      }
   }
```

```
   else if( length_cat==1 ) # Deformation zone is always stable.
      rc = 1000;
   else
   {
      printf( "ERROR: Length category %d not recognized.",length_cat
);
      rc = 0;
   }
#  printf( "DEBUG: rc %9.3f\n",rc );
   return( rc );
}
BEGIN {
   TRUE = 0==0;
   FALSE=!TRUE;
   PI = 2*atan2(1,0);
   set_length_categories();
   zfloor = -465;           # Z coordinate of tunnel floor (m).
   lcan   =  4.835;         # Length of canister (m).
   cantop =  zfloor-2.75;   # Canister top (m), allowing for 1.25 m
bevel plus 1.5 m bentonite above can.
   canbot =  cantop-lcan;   # Canister bottom (m).
}
{
   if( NR==1 ) # Parse deformation zone column labels from header line
and initialize tallies of critical fractures.
   {
      print $0;
      nzones = 0;
      for( i=30; i<=NF; i++ )
         zone_name[nzones++] = "ZFM" $i;
#
      for( i=0; i<nzones; i++ )
      {
         nCrit[i]  = 0; # Count of critical fractures for this zone
using modified-radius criterion.
         nCritX[i] = 0; # Count of such fractures that would be
rejected using EFPC.
         ncrit[i]  = 0; # Count of critical fractures for this zone
based on strict criterion.
         ncritX[i] = 0; # Count of such fractures that would be
rejected using EFPC.
      }
   }
   else
   {
      id   = $1;  # Panel ID (which can be related directly to
fracture ID, and indirectly to fracture domain).
      R    = $3;  # Use Equiv R column (equivalent fracture radius) as
the effective radius of the fracture.
      c[0] = $4;  # X, Y, and Z coordinates of the fracture centroid
are stored as the vector c[].
      c[1] = $5;
      c[2] = $6;
      nz   = $9;  # Z component of the fracture normal vector which is
needed to calculate the fracture dip angle.
      EFPC = $11; # KEEP or RJCT
      x[0] = $16; # X, Y, and Z coordinates of the intersection
between the fracture and the deposition-hole axis are stored as x[].
      x[1] = $17;
      x[2] = $18;
#
      printf( "%s",$0 ); # Print a copy of the line.
#
      if( x[2]<=cantop && x[2]>=canbot ) # Feature crosses canister
axis within length of canister.
      {
         r    = distance_between_points( c,x ); # Calculate the
distance from the fracture's centroid to its intersection with the
deposition hole.
```

```
         if( nz<0 ) nz = -nz;                    # Get absolute value
of z component of the fracture normal vector.
         dip  = acos( nz )*180/PI;               # Calculate dip angle
in degrees from this component.
         reject = EFPC=="RJCT"
#
         for( i=0; i<nzones; i++ )               # Loop over each of
the fracture zones.
         {
#           printf( "\nDEBUG: Zone %s\n",zone_name[i] );
            distance = $(19+i);
            lc = length_category[zone_name[i]];
            Rc = critical_radius( lc,dip,distance );
            if( R>Rc )
            {
               Rcp = sqrt( R*R - Rc*Rc ); # Modified fracture radius
according to TR-10-21 Eq. 28, p. 53.
               if( r>Rcp )                # Intersection with
deposition hole is outside the radius at which displacement d>dcrit
can theoretically occur.
                  printf( " c" );         # Identifies critical
position but only for stricter criterion.
               else
               {
                  printf( " C" );         # Identifies position that
is critical even based on modified radius.
                  nCrit[i]++;             # Increment count of
critical fractures for this zone using modified-radius criterion.
                  if( reject ) nCritX[i]++;  # Increment if fracture
would be rejected using EFPC.
               }
               ncrit[i]++;                # Increment count of
critical fractures for this zone based on strict criterion.
               if( reject ) ncritX[i]++;  # Increment if fracture
would be rejected using EFPC.
            }
            else
               printf( "  " );            # Spacer.
         }
      }
      printf( "\n" );
   }
}
END {
   printf( "\nCritical fractures by category   :" );
   for( i=0; i<nzones; i++ ) printf( " %11s",zone_name[i] );
   printf( "\nncritical (escaped FPI)          :" );
   for( i=0; i<nzones; i++ ) printf( " %11d",ncrit[i] );
   printf( "\nncritical (escaped FPI+EFPC)     :" );
   for( i=0; i<nzones; i++ ) printf( " %11d",ncrit[i]-ncritX[i] );
   printf( "\nnCritical (escaped FPI) reduced R:" );
   for( i=0; i<nzones; i++ ) printf( " %11d",nCrit[i] );
   printf( "\nnCritical (escaped FPI+EFPC)     :" );
   for( i=0; i<nzones; i++ ) printf( " %11d",nCrit[i]-nCritX[i] );
   printf( "\n" );
}
```

APPENDIX 3

Quality check of simulated fracture orientations

The simulated fracture orientation distributions were confirmed both quantitatively by statistical measures, and qualitatively by equal-area stereonet plots for individual fracture sets.

The consistency of the fitted Fisher mean poles (mean pole trend and plunge in degrees, as given in parentheses) and concentration parameters κ in the following listing have been checked against the same parameters for the same fracture sets as listed in Tables 2 through 7. For the sake of efficiency and also to base the comparison on a larger sample, the Fisher mean poles have been fitted to the composite dataset for all 10 realizations of each calculation case.

The mean pole directions, as listed below, are generally in very close agreement, usually within a fraction of a degree. Values of the Fisher concentration κ, as also listed below, generally agree with the specified values within 5%.

Supplementary to these quantitative checks, stereonet plots were also produced for graphical inspection, mainly to confirm that the distributions reproduced have appropriate radial symmetry (as the mean orientations and concentration about the mean are checked by quantitative measures). These are shown for calculation case r3 in Figures A3.1a through A3.1c, for calculation case o3 in Figures A3.2a through A3.2e, and for calculation case t2 in Figures A3.3a through A3.3c. Figures A3.4 through A3.6 are provided to show visual comparisons between the base case for each DFN alternative and the corresponding elevated-P_{32} variant.

The very close agreement of the quantitative statistical estimates of mean directions and Fisher concentrations with the specified values, along with the visual checks of radial symmetry based on the plots, give high confidence that the orientation distributions for each fracture set are accurately simulated. The only exceptions are a few fracture sets (for example Sets 12 and 24 in the OSM-TFM model, as seen in Figure A3.2b and A3.2d, respectively) for which the number of fractures simulated per base case realization is less than 25. The stereonet plots for the corresponding sets in the elevated-P_{32} variants (Figures A3.4a and A3.4b) show that the sets become more regular with a larger sample.

The following is a printout of the results of fitting Fisher distribution parameters to the fracture poles for each fracture set in each of the 10 realizations of each calculation case.

The sets are numbered in the same order as they are listed in Tables 2 through 7, and as they appear in the stereonet plots. For each fracture set, there are three lines of data. The first line gives the specified mean orientation and Fisher concentration parameter are given for comparison with the values estimated based on the realizations. The second and third lines give the results of the statistical fitting for the base case and the elevated-intensity variants, respectively, in the following format:

Column 1: Set #
Column 2: Number of fractures in this set (N = …)
Columns 3-5: Fitted mean pole expressed as a unit vector in Cartesian (x,y,z) coordinates
Columns 6-8: Fitted mean pole (trend, plunge) +/- spherical standard error
Column 9: 95% confidence cone in degrees
Column 10: Estimated Fisher concentration parameter κ

r_0-fixed alternative (base case r3 and elevated-intensity variant rg2)

Fracture domain FFM01:

Set 1 NE global specified mean orientation: (314.9 1.3) κ 20.94
Set 1 (N = 678761) -0.705229 -0.708644 -0.021797 (314.86, 1.25) +/- 0.000382 95% cone 0.038° κ 21.16
Set 1 (N = 847779) -0.705292 -0.708583 -0.021754 (314.87, 1.25) +/- 0.000342 95% cone 0.034° κ 21.14

Set 2 NS global specified mean orientation: (270.1 5.3) κ 21.34
Set 2 (N = 454496) -0.004514 -0.995815 -0.091284 (270.26, 5.24) +/- 0.000464 95% cone 0.046° κ 21.48
Set 2 (N = 570512) -0.003908 -0.995801 -0.091463 (270.22, 5.25) +/- 0.000414 95% cone 0.041° κ 21.48

Set 3 NW global specified mean orientation: (230.1 4.6) κ 15.70
Set 3 (N = 531304) 0.642049 -0.762541 -0.079397 (229.90, 4.55) +/- 0.000506 95% cone 0.050° κ 15.70
Set 3 (N = 659392) 0.641584 -0.762905 -0.079664 (229.94, 4.57) +/- 0.000454 95% cone 0.045° κ 15.72

Set 4 SH global specified mean orientation: (0.8 87.3) κ 17.42
Set 4 (N = 318614) -0.049160 0.000664 -0.998791 (0.77,87.18) +/- 0.000633 95% cone 0.063° κ 16.70
Set 4 (N = 400033) -0.049850 0.000425 -0.998757 (0.49,87.14) +/- 0.000565 95% cone 0.056° κ 16.68

Set 5 ENE local specified mean orientation: (157.5 3.1) κ 34.11
Set 5 (N = 37760) 0.923026 0.380753 -0.055235 (157.58, 3.17) +/- 0.001266 95% cone 0.126° κ 34.03
Set 5 (N = 47934) 0.923595 0.379736 -0.052657 (157.65, 3.02) +/- 0.001126 95% cone 0.112° κ 33.89

Set 6 EW local specified mean orientation: (0.4 11.9) κ 13.89

Set 6 (N = 30092) -0.979523 0.007022 -0.201211 (0.41,11.61) +/- 0.002249 95% cone 0.223° κ 14.14
Set 6 (N = 37610) -0.979019 0.005743 -0.203689 (0.34,11.75) +/- 0.002025 95% cone 0.201° κ 13.97

Set 7 NNE local specified mean orientation: (293.8 0.0) κ 21.79
Set 7 (N = 90355) 0.403272 0.915080 -0.000679 (113.78, 0.04) +/- 0.001028 95% cone 0.102° κ 21.95
Set 7 (N = 112951) 0.403973 0.914771 -0.000027 (113.83, 0.00) +/- 0.000920 95% cone 0.091° κ 21.93

Set 8 SH2 local specified mean orientation: (164.0 52.6) κ 35.43
Set 8 (N = 41671) 0.588140 0.167966 -0.791125 (164.06,52.29) +/- 0.001182 95% cone 0.117° κ 35.37
Set 8 (N = 51746) 0.588602 0.168598 -0.790647 (164.02,52.25) +/- 0.001058 95% cone 0.105° κ 35.51

Set 9 SH3 local specified mean orientation: (337.9 52.9) κ 17.08
Set 9 (N = 34155) -0.567059 -0.230869 -0.790660 (337.85,52.25) +/- 0.001908 95% cone 0.189° κ 17.08
Set 9 (N = 43417) -0.567622 -0.230882 -0.790253 (337.87,52.21) +/- 0.001694 95% cone 0.168° κ 17.04

Fracture domain FFM06:
Set 10 NE global specified mean orientation: (125.7 10.1) κ 45.05
Set 10 (N = 237787) 0.574454 0.799670 -0.174728 (125.69,10.06) +/- 0.000437 95% cone 0.043° κ 45.11
Set 10 (N = 296977) 0.574464 0.799580 -0.175106 (125.70,10.08) +/- 0.000390 95% cone 0.039° κ 45.17

Set 11 NS global specified mean orientation: (91.0 4.1) κ 19.49
Set 11 (N = 161169) 0.014638 0.997496 -0.069189 (90.84, 3.97) +/- 0.000814 95% cone 0.081° κ 19.71
Set 11 (N = 200352) 0.014973 0.997355 -0.071130 (90.86, 4.08) +/- 0.000732 95% cone 0.073° κ 19.65

Set 12 NW global specified mean orientation: (34.1 0.8) κ 16.13
Set 12 (N = 183822) -0.827474 0.561319 -0.014441 (34.15, 0.83) +/- 0.000844 95% cone 0.084° κ 16.28
Set 12 (N = 231173) -0.827744 0.560958 -0.012878 (34.13, 0.74) +/- 0.000753 95% cone 0.075° κ 16.25

Set 13 SH global specified mean orientation: (84.3 71.3) κ 10.78
Set 13 (N = 82169) -0.031323 0.333609 -0.942191 (84.64,70.42) +/- 0.001606 95% cone 0.159° κ 10.44
Set 13 (N = 101858) -0.033478 0.333414 -0.942186 (84.27,70.42) +/- 0.001445 95% cone 0.143° κ 10.42

Set 14 ENE local specified mean orientation: (155.4 8.3) κ 20.83
Set 14 (N = 10478) 0.900075 0.411721 -0.142655 (155.42, 8.20) +/- 0.003114 95% cone 0.309° κ 20.69

Set 14 (N = 13143) 0.900489 0.411547 -0.140530 (155.44, 8.08) +/- 0.002785 95% cone 0.276° κ 20.63

Set 15 SH2 local specified mean orientation: (0.0 47.5) κ 12.71
Set 15 (N = 52623) -0.684451 -0.000341 -0.729059 (359.97,46.81) +/- 0.001802 95% cone 0.179° κ 12.69
Set 15 (N = 66421) -0.685894 0.000467 -0.727701 (0.04,46.69) +/- 0.001602 95% cone 0.159° κ 12.72

OSM-TCM alternative (base case o3 and elevated-intensity variant og3)

Fracture domain FFM01:
Set 1 OSM NE global specified mean orientation: (314.9 1.3) κ 20.94
Set 1 (N = 845699) -0.705183 -0.708692 -0.021750 (314.86, 1.25) +/- 0.000343 95% cone 0.034° κ 21.14
Set 1 (N =1057562) -0.705299 -0.708574 -0.021832 (314.87, 1.25) +/- 0.000306 95% cone 0.030° κ 21.15

Set 2 OSM NS global specified mean orientation: (270.1 5.3) κ 21.34
Set 2 (N = 248700) -0.004694 -0.995789 -0.091559 (270.27, 5.25) +/- 0.000626 95% cone 0.062° κ 21.53
Set 2 (N = 311946) -0.003625 -0.995825 -0.091213 (270.21, 5.23) +/- 0.000559 95% cone 0.055° κ 21.49

Set 3 OSM NW global specified mean orientation: (230.1 4.6) κ 15.70
Set 3 (N = 810063) 0.641687 -0.762859 -0.079270 (229.93, 4.55) +/- 0.000410 95% cone 0.041° κ 15.72
Set 3 (N = 1011029) 0.641473 -0.763031 -0.079350 (229.95, 4.55) +/- 0.000367 95% cone 0.036° κ 15.72

Set 4 OSM SH global specified mean orientation: (0.8 87.3) κ 17.42
Set 4 (N = 275318) -0.049549 0.000848 -0.998771 (0.98,87.16) +/- 0.000681 95% cone 0.068° κ 16.66
Set 4 (N = 344168) -0.049698 0.000841 -0.998764 (0.97,87.15) +/- 0.000609 95% cone 0.060° κ 16.68

Set 5 OSM ENE local specified mean orientation: (157.5 3.1) κ 34.11
Set 5 (N = 256042) 0.922773 0.381534 -0.054057 (157.54, 3.10) +/- 0.000487 95% cone 0.048° κ 34.00
Set 5 (N = 322075) 0.922905 0.381203 -0.054131 (157.56, 3.10) +/- 0.000434 95% cone 0.043° κ 34.02

Set 6 OSM EW local specified mean orientation: (0.4 11.9) κ 13.89
Set 6 (N = 17424) -0.979165 0.003150 -0.203041 (0.18,11.71) +/- 0.002989 95% cone 0.296° κ 13.85
Set 6 (N = 22085) -0.979451 0.006716 -0.201568 (0.39,11.63) +/- 0.002644 95% cone 0.262° κ 13.95

Set 7 OSM NNE local specified mean orientation: (293.8 0.0) κ 21.79

Set 7 (N = 86985) 0.404098 0.914715 -0.000359 (113.83, 0.02) +/- 0.001049 95% cone 0.104° κ 21.90
Set 7 (N = 109127) -0.403699 -0.914891 -0.000701 (293.81, 0.04) +/- 0.000937 95% cone 0.093° κ 21.88

Set 8 OSM SH2 local specified mean orientation: (164.0 52.6) κ 35.43
Set 8 (N = 39643) 0.588683 0.168428 -0.790623 (164.03,52.24) +/- 0.001211 95% cone 0.120° κ 35.43
Set 8 (N = 48997) 0.589206 0.169303 -0.790046 (163.97,52.19) +/- 0.001091 95% cone 0.108° κ 35.27

Set 9 OSM SH3 local specified mean orientation: (337.9 52.9) κ 17.08
Set 9 (N = 32346) -0.572600 -0.230025 -0.786904 (338.11,51.90) +/- 0.001955 95% cone 0.194° κ 17.17
Set 9 (N = 40573) -0.572165 -0.232279 -0.786558 (337.90,51.87) +/- 0.001751 95% cone 0.174° κ 17.07

Set 10 TFM NE global specified mean orientation: (315.3 1.8) κ 27.02
Set 10 (N = 37667) -0.710290 -0.703230 -0.030920 (315.29, 1.77) +/- 0.001425 95% cone 0.141° κ 27.13
Set 10 (N = 47188) -0.708910 -0.704565 -0.032169 (315.18, 1.84) +/- 0.001272 95% cone 0.126° κ 27.21

Set 11 TFM NS global specified mean orientation: (92.7 1.2) κ 30.69
Set 11 (N = 299) 0.034771 0.998698 -0.037323 (91.99, 2.14) +/- 0.014877 95% cone 1.475° κ 31.25
Set 11 (N = 383) 0.055502 0.997776 -0.036923 (93.18, 2.12) +/- 0.013477 95% cone 1.337° κ 29.69

Set 12 TFM NW global specified mean orientation: (47.6 4.4) κ 19.67
Set 12 (N = 216) -0.666728 0.743692 -0.048944 (48.12, 2.81) +/- 0.022510 95% cone 2.233° κ 19.33
Set 12 (N = 251) -0.657644 0.748318 -0.086747 (48.69, 4.98) +/- 0.020575 95% cone 2.041° κ 19.91

Set 13 TFM SH global specified mean orientation: (347.4 85.6) κ 17.42
Set 13 (N = 29685) -0.077573 -0.015878 -0.996860 (348.43,85.46) +/- 0.001777 95% cone 0.176° κ 22.34
Set 13 (N = 36924) -0.078741 -0.016725 -0.996755 (348.01,85.38) +/- 0.001590 95% cone 0.158° κ 22.43

Set 14 TFM ENE global specified mean orientation: (157.9 4.0) κ 53.18
Set 14 (N = 119868) 0.924501 0.374682 -0.070083 (157.94, 4.02) +/- 0.000566 95% cone 0.056° κ 53.08
Set 14 (N = 148993) 0.924507 0.374733 -0.069732 (157.94, 4.00) +/- 0.000508 95% cone 0.050° κ 52.93

Set 15 TFM EW global specified mean orientation: (186.3 4.3) κ 34.23
Set 15 (N = 1741) 0.990884 -0.114530 -0.070936 (186.59, 4.07) +/- 0.005835 95% cone 0.579° κ 34.74
Set 15 (N = 2087) 0.991284 -0.109990 -0.072518 (186.33, 4.16) +/- 0.005282 95% cone 0.524° κ 35.35

Fracture domain FFM06:

Set 16 OSM NE global specified mean orientation: (125.7 10.1) κ 45.05
Set 16 (N = 378089) 0.574444 0.799601 -0.175076 (125.69,10.08) +/- 0.000346 95% cone 0.034° κ 45.12
Set 16 (N = 470302) 0.574215 0.799914 -0.174400 (125.67,10.04) +/- 0.000311 95% cone 0.031° κ 44.99

Set 17 OSM NS global specified mean orientation: (91.0 4.1) κ 19.49
Set 17 (N = 100156) 0.015386 0.997322 -0.071492 (90.88, 4.10) +/- 0.001034 95% cone 0.103° κ 19.67
Set 17 (N = 125711) 0.014638 0.997356 -0.071182 (90.84, 4.08) +/- 0.000925 95% cone 0.092° κ 19.58

Set 18 OSM NW global specified mean orientation: (34.1 0.8) κ 16.13
Set 18 (N = 335453) -0.827596 0.561166 -0.013311 (34.14, 0.76) +/- 0.000625 95% cone 0.062° κ 16.26
Set 18 (N = 421141) -0.827280 0.561635 -0.013185 (34.17, 0.76) +/- 0.000557 95% cone 0.055° κ 16.31

Set 19 OSM SH global specified mean orientation: (84.3 71.3) κ 10.78
Set 19 (N = 71357) -0.035402 0.333759 -0.941994 (83.95,70.39) +/- 0.001727 95% cone 0.171° κ 10.41
Set 19 (N = 89483) -0.034168 0.333058 -0.942287 (84.14,70.44) +/- 0.001542 95% cone 0.153° κ 10.41

Set 20 OSM ENE local specified mean orientation: (155.4 8.3) κ 20.83
Set 20 (N = 46681) 0.900738 0.409585 -0.144606 (155.55, 8.31) +/- 0.001472 95% cone 0.146° κ 20.77
Set 20 (N = 58869) 0.900915 0.409168 -0.144684 (155.57, 8.32) +/- 0.001313 95% cone 0.130° κ 20.72

Set 21 OSM SH2 local specified mean orientation: (0.0 47.5) κ 12.71
Set 21 (N = 51250) -0.687385 -0.001011 -0.726292 (359.92,46.58) +/- 0.001832 95% cone 0.182° κ 12.62
Set 21 (N = 64185) -0.685883 0.002722 -0.727707 (0.23,46.69) +/- 0.001633 95% cone 0.162° κ 12.68

Set 22 TFM NE global specified mean orientation: (315.3 1.8) κ 20.94
Set 22 (N = 8334) -0.712495 -0.700898 -0.033055 (315.47, 1.89) +/- 0.003007 95% cone 0.298° κ 27.54
Set 22 (N = 10638) -0.711175 -0.702204 -0.033748 (315.36, 1.93) +/- 0.002673 95% cone 0.265° κ 27.32

Set 23 TFM NS global specified mean orientation: (92.7 1.2) κ 21.34
Set 23 (N = 92) -0.034670 -0.999284 -0.015118 (271.99, 0.87) +/- 0.027781 95% cone 2.756° κ 29.28
Set 23 (N = 115) 0.050100 0.998438 -0.024734 (92.87, 1.42) +/- 0.023433 95% cone 2.324° κ 32.69

Set 24 TFM NW global specified mean orientation: (47.6 4.4) κ 15.70

Set 24 (N = 48) -0.657356 0.753580 -0.000181 (48.90, 0.01) +/- 0.050781 95% cone 5.042° κ 17.14
Set 24 (N = 84) -0.655938 0.751162 -0.074168 (48.87, 4.25) +/- 0.035738 95% cone 3.546° κ 19.59

Set 25 TFM SH global specified mean orientation: (347.4 85.6) κ 17.42
Set 25 (N = 6523) -0.082247 -0.013266 -0.996524 (350.84,85.22) +/- 0.003800 95% cone 0.377° κ 22.22
Set 25 (N = 8051) -0.070530 -0.014919 -0.997398 (348.06,85.87) +/- 0.003415 95% cone 0.339° κ 22.29

Set 26 TFM ENE global specified mean orientation: (157.9 4.0) κ 53.18
Set 26 (N = 26425) 0.924141 0.375846 -0.068576 (157.87, 3.93) +/- 0.001204 95% cone 0.119° κ 53.25
Set 26 (N = 33290) 0.924385 0.375094 -0.069397 (157.91, 3.98) +/- 0.001077 95% cone 0.107° κ 52.84

Set 27 TFM EW global specified mean orientation: (186.3 4.3) κ 34.23
Set 27 (N = 354) 0.991331 -0.110231 -0.071496 (186.34, 4.10) +/- 0.013301 95% cone 1.319° κ 32.92
Set 27 (N = 523) 0.991061 -0.114049 -0.069216 (186.56, 3.97) +/- 0.010845 95% cone 1.076° κ 33.48

TCM alternative (base case t2 and elevated-intensity variant tg2)

Fracture domain FFM01:

Set 1 NE global specified mean orientation: (314.9 1.3) κ 20.94
Set 1 (N =3916209) -0.705182 -0.708680 -0.022166 (314.86, 1.27) +/- 0.000159 95% cone 0.016° κ 21.14
Set 1 (N =4895952) -0.705223 -0.708638 -0.022173 (314.86, 1.27) +/- 0.000142 95% cone 0.014° κ 21.14

Set 2 NS global specified mean orientation: (270.1 5.3) κ 21.34
Set 2 (N = 557826) -0.003853 -0.995766 -0.091845 (270.22, 5.27) +/- 0.000418 95% cone 0.041° κ 21.55
Set 2 (N = 697594) -0.003659 -0.995769 -0.091822 (270.21, 5.27) +/- 0.000374 95% cone 0.037° κ 21.49

Set 3 NW global specified mean orientation: (230.1 4.6) κ 15.70
Set 3 (N =2275313) 0.641253 -0.763247 -0.079052 (229.96, 4.53) +/- 0.000244 95% cone 0.024° κ 15.74
Set 3 (N =2845218) 0.641262 -0.763218 -0.079255 (229.96, 4.55) +/- 0.000218 95% cone 0.022° κ 15.74

Set 4 SH global specified mean orientation: (0.8 87.3) κ 17.42
Set 4 (N =1636454) -0.049096 0.000540 -0.998794 (0.63,87.19) +/- 0.000279 95% cone 0.028° κ 16.70
Set 4 (N =2042884) -0.049062 0.000694 -0.998795 (0.81,87.19) +/- 0.000250 95% cone 0.025° κ 16.69

Set 5 ENE local specified mean orientation: (157.5 3.1) κ 34.11
Set 5 (N = 180173) 0.923122 0.380757 -0.053566 (157.59, 3.07) +/- 0.000581 95% cone 0.058° κ 33.93
Set 5 (N = 225271) 0.922793 0.381406 -0.054607 (157.54, 3.13) +/- 0.000518 95% cone 0.051° κ 34.11

Set 6 EW local specified mean orientation: (0.4 11.9) κ 13.89
Set 6 (N = 77401) -0.979338 0.006664 -0.202120 (0.39,11.66) +/- 0.001404 95% cone 0.139° κ 14.12
Set 6 (N = 97422) -0.979508 0.006428 -0.201304 (0.38,11.61) +/- 0.001252 95% cone 0.124° κ 14.08

Set 7 NNE local specified mean orientation: (293.8 0.0) κ 21.79
Set 7 (N = 89097) -0.403335 -0.915052 -0.000629 (293.79, 0.04) +/- 0.001034 95% cone 0.103° κ 21.99
Set 7 (N = 111788) 0.403522 0.914970 -0.000231 (113.80, 0.01) +/- 0.000923 95% cone 0.092° κ 22.01

Set 8 SH2 local specified mean orientation: (164.0 52.6) κ 35.43
Set 8 (N = 40986) 0.588540 0.168525 -0.790708 (164.02,52.25) +/- 0.001187 95% cone 0.118° κ 35.62
Set 8 (N = 51401) 0.588963 0.167795 -0.790549 (164.10,52.24) +/- 0.001063 95% cone 0.105° κ 35.41

Set 9 SH3 local specified mean orientation: (337.9 52.9) κ 17.08
Set 9 (N = 34536) -0.568273 -0.231820 -0.789510 (337.81,52.14) +/- 0.001901 95% cone 0.188° κ 17.04
Set 9 (N = 41683) -0.568345 -0.229564 -0.790117 (338.01,52.20) +/- 0.001729 95% cone 0.171° κ 17.05

Fracture domain FFM06:

Set 10 NE global specified mean orientation: (125.7 10.1) κ 45.05
Set 10 (N = 919599) 0.574358 0.799748 -0.174688 (125.68,10.06) +/- 0.000222 95% cone 0.022° κ 45.03
Set 10 (N =1150911) 0.574288 0.799761 -0.174859 (125.68,10.07) +/- 0.000199 95% cone 0.020° κ 45.03

Set 11 NS global specified mean orientation: (91.0 4.1) κ 19.49
Set 11 (N = 160247) 0.014231 0.997367 -0.071113 (90.82, 4.08) +/- 0.000819 95% cone 0.081° κ 19.61
Set 11 (N = 200545) 0.014423 0.997309 -0.071876 (90.83, 4.12) +/- 0.000731 95% cone 0.073° κ 19.66

Set 12 NW global specified mean orientation: (34.1 0.8) κ 16.13
Set 12 (N = 559310) -0.827893 0.560735 -0.012987 (34.11, 0.74) +/- 0.000482 95% cone 0.048° κ 16.36
Set 12 (N = 699340) -0.827597 0.561156 -0.013663 (34.14, 0.78) +/- 0.000432 95% cone 0.043° κ 16.30

Set 13 SH global specified mean orientation: (84.3 71.3) κ 10.78

Set 13 (N = 414104) -0.033715 0.333990 -0.941974 (84.24,70.39) +/- 0.000717 95% cone 0.071° κ 10.39
Set 13 (N = 517799) -0.033584 0.333415 -0.942182 (84.25,70.42) +/- 0.000641 95% cone 0.064° κ 10.42

Set 14 ENE local specified mean orientation: (155.4 8.3) κ 20.83
Set 14 (N = 91755) 0.900397 0.410785 -0.143322 (155.48, 8.24) +/- 0.001049 95% cone 0.104° κ 20.81
Set 14 (N = 115390) 0.900386 0.410658 -0.143754 (155.48, 8.27) +/- 0.000935 95% cone 0.093° κ 20.81

Set 15 SH2 local specified mean orientation: (0.0 47.5) κ 12.71
Set 15 (N = 53426) -0.686081 0.001703 -0.727523 (0.14,46.68) +/- 0.001786 95% cone 0.177° κ 12.73
Set 15 (N = 66668) -0.686842 -0.000773 -0.726806 (359.94,46.62) +/- 0.001602 95% cone 0.159° κ 12.68

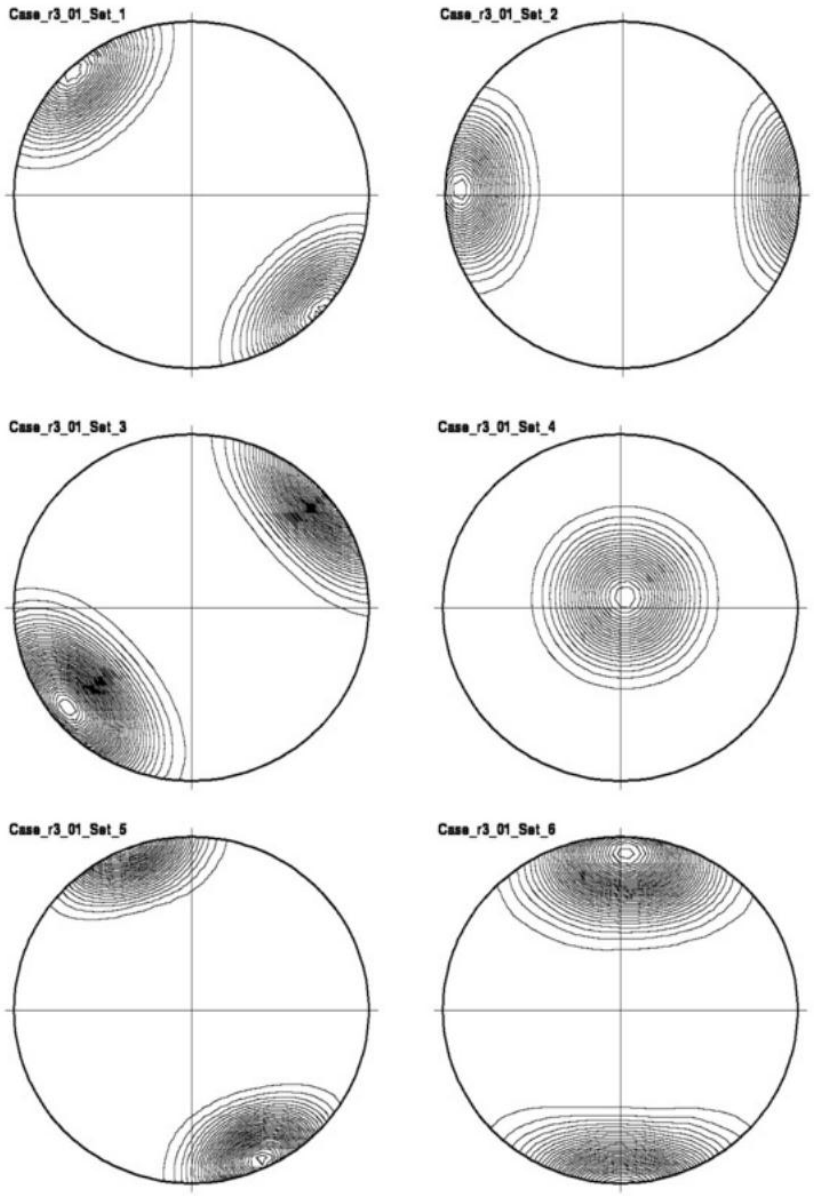

Figure A3.1a. Equal-area stereonet plots of simulated fracture pole directions for the first six fracture sets in fracture domain FFM01, r0-fixed model: (1) NE global, (2) NS global, (3) NW global, (4) SH global, (5) ENE local, and (6) EW local.

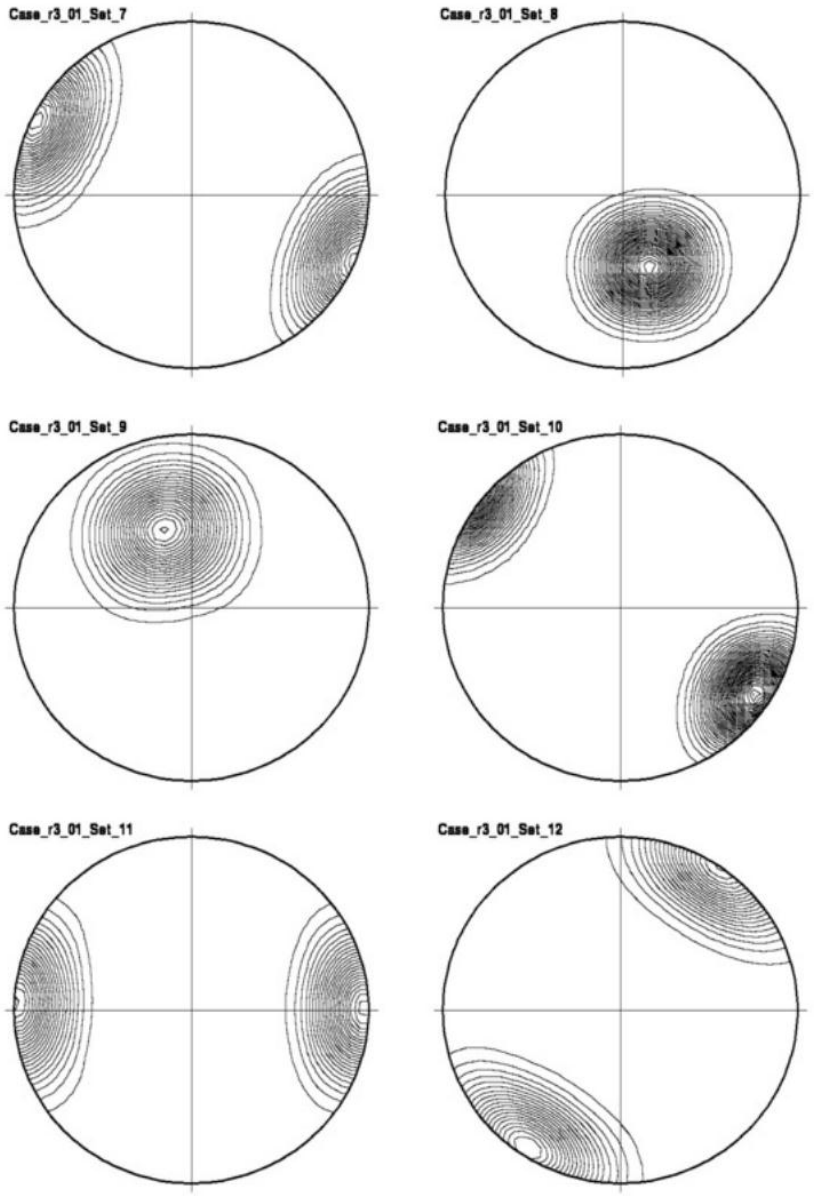

Figure A3.1b. Equal-area stereonet plots of simulated fracture pole directions for the last three fracture sets in fracture domain FFM01, r0-fixed model: (7) NNE local, (8) SH2 local, (9) SH3 local; plus the first three sets of FFM06: (10) NE global, (11) NS global, and (12) NW global.

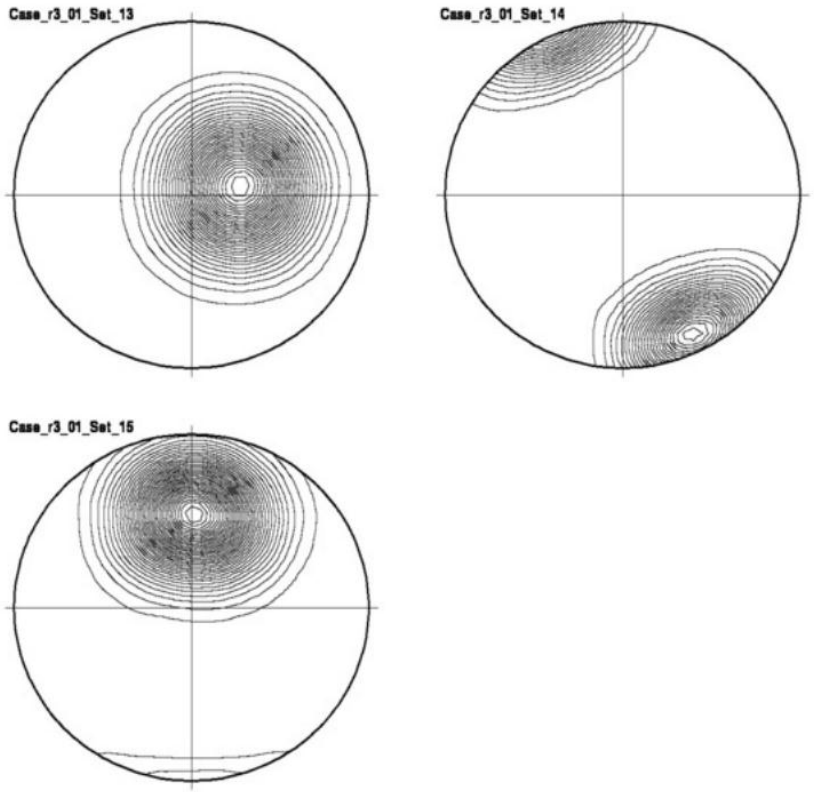

Figure A3.1c. Equal-area stereonet plots of simulated fracture pole directions for the last three fracture sets in fracture domain FFM06: (13) SH global, (14) ENE local, and (15) SH2 local.

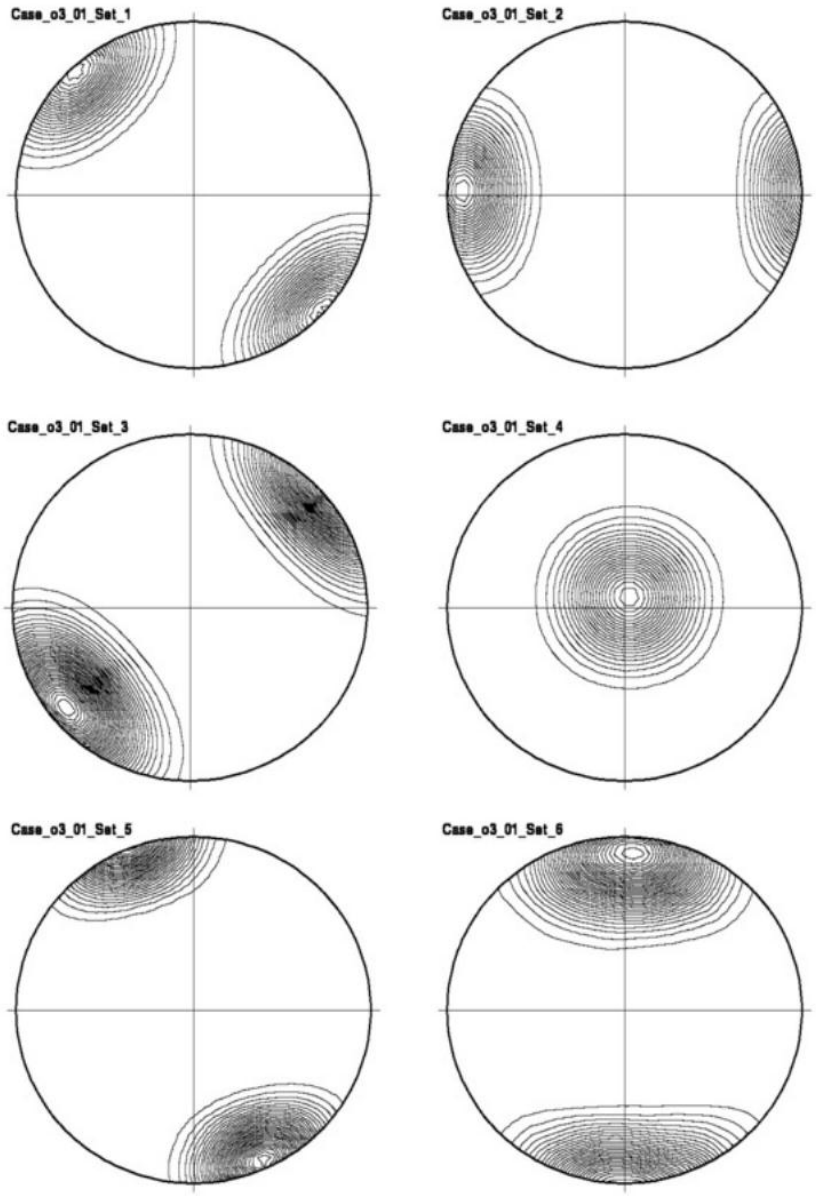

Figure A3.2a. Equal-area stereonet plots of simulated fracture pole directions for the first six fracture sets in fracture domain FFM01, OSM model: (1) NE global, (2) NS global, (3) NW global, (4) SH global, (5) ENE local, and (6) EW local.

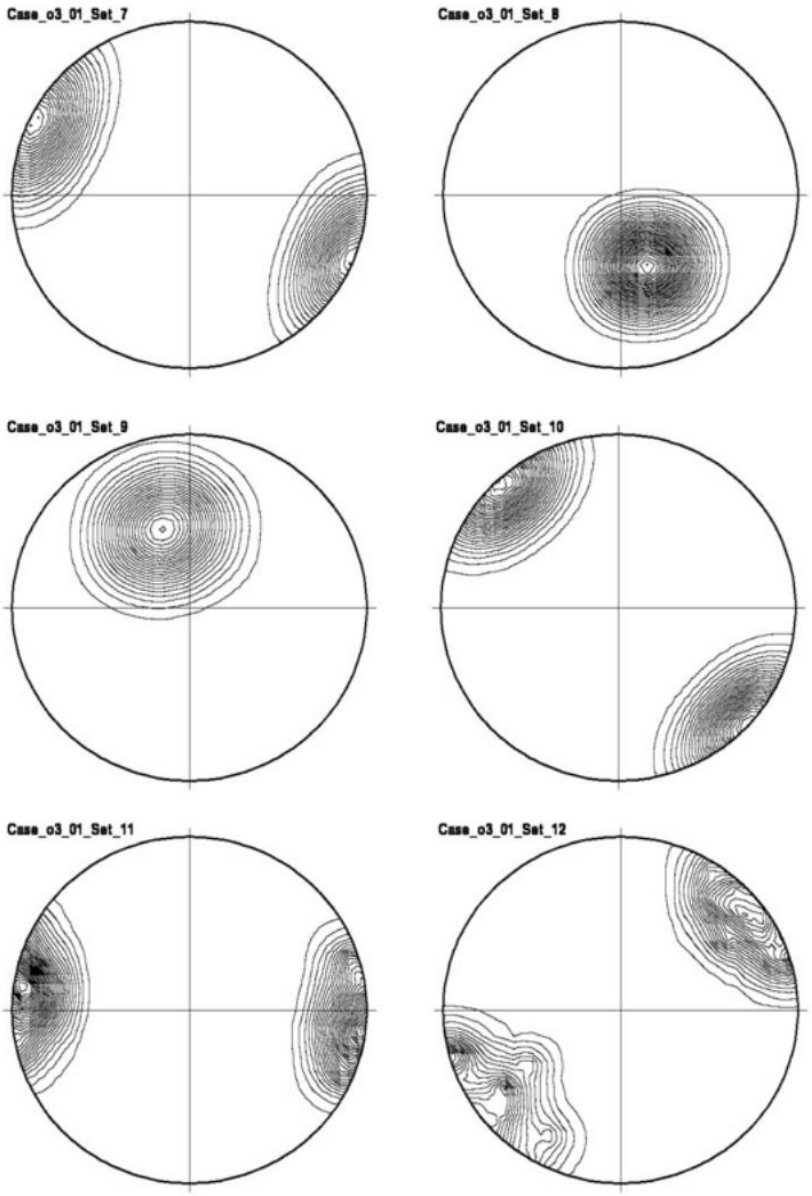

Figure A3.2b. Equal-area stereonet plots of simulated fracture pole directions for the last three fracture sets in fracture domain FFM01, OSM model: (7) NNE local, (8) SH2 local, (9) SH3 local; plus the first three TFM sets: (10) NE global, (11) NS global, and (12) NW global.

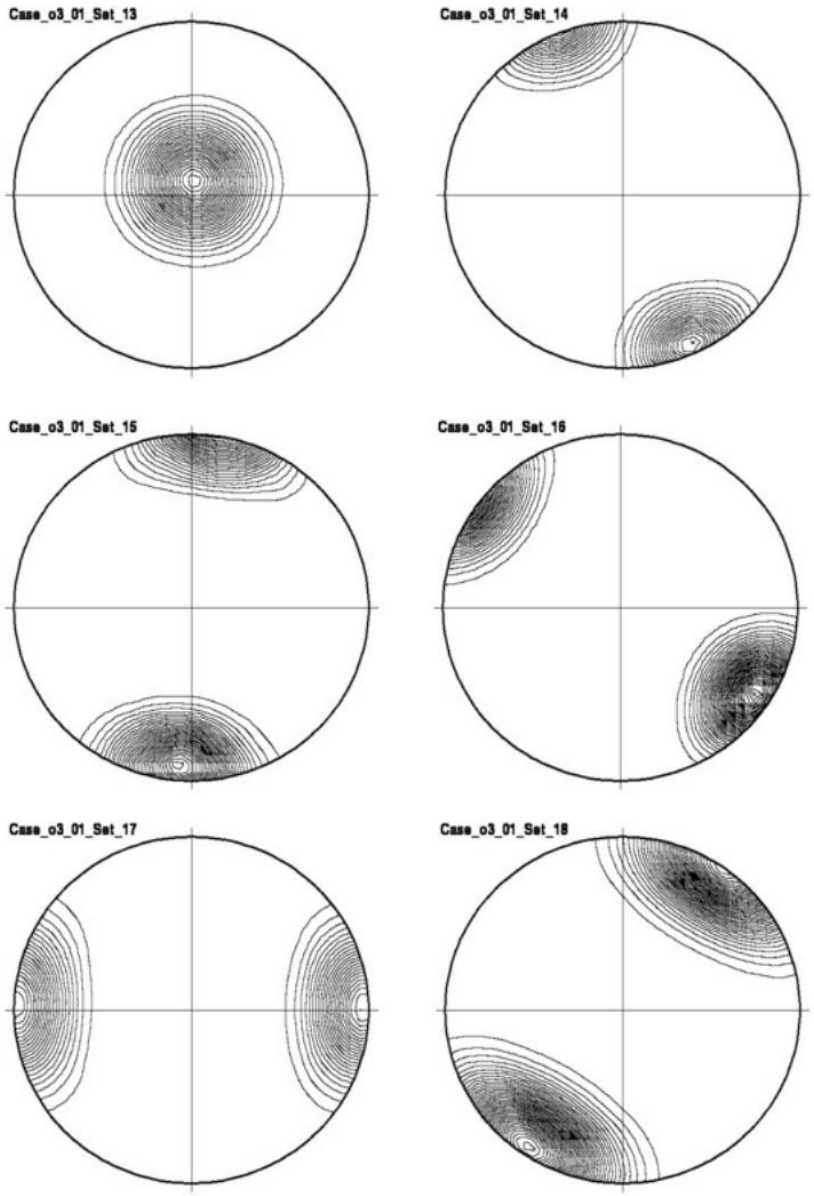

Figure A3.2c. Equal-area stereonet plots of simulated fracture pole directions for the last three fracture sets in fracture domain FFM01, TFM model: (13) SH global, (14) ENE global, (15) EW global; plus the first three sets of FFM06, OSM model: (16) NE global, (17) NS global, and (18) NW global.

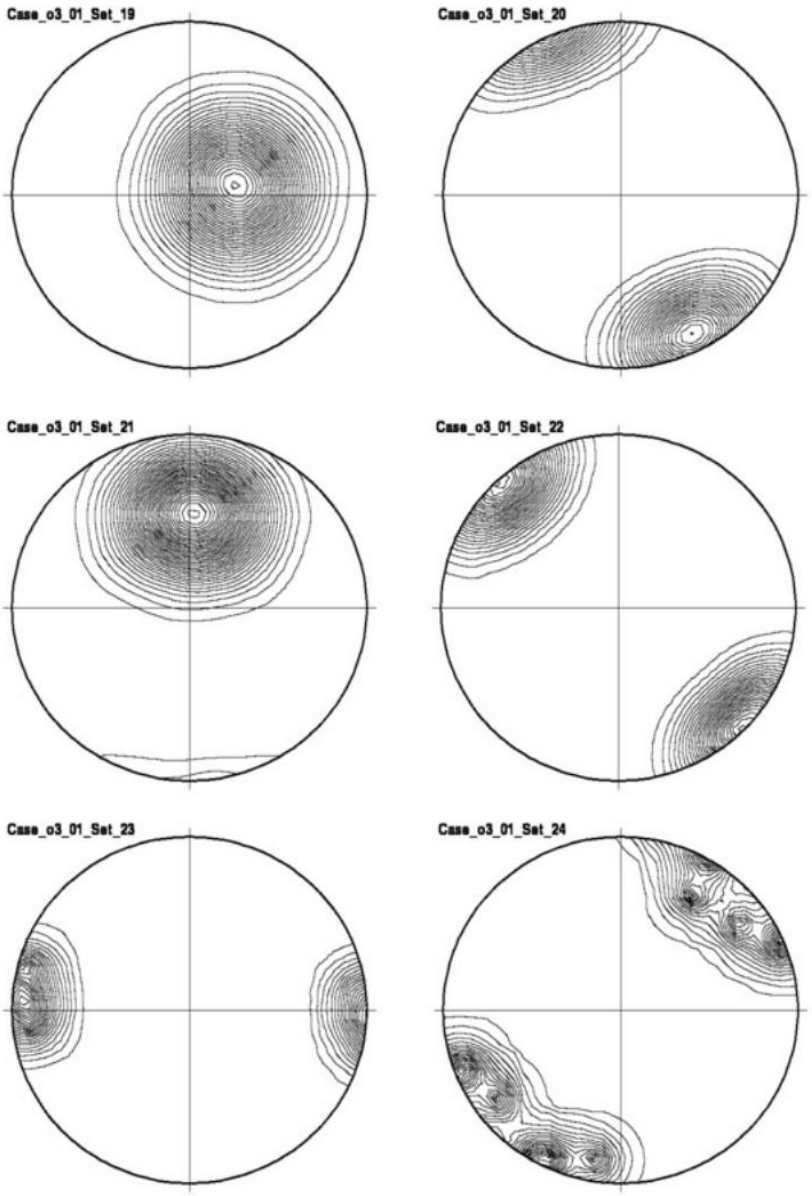

Figure A3.2d. Equal-area stereonet plots of simulated fracture pole directions for the last three fracture sets in fracture domain FFM06, OSM model: 19) SH global, (20) ENE local, (21) SH2 local; plus the first three TFM sets: (22) NE global, (23) NS global, and (24) NW global.

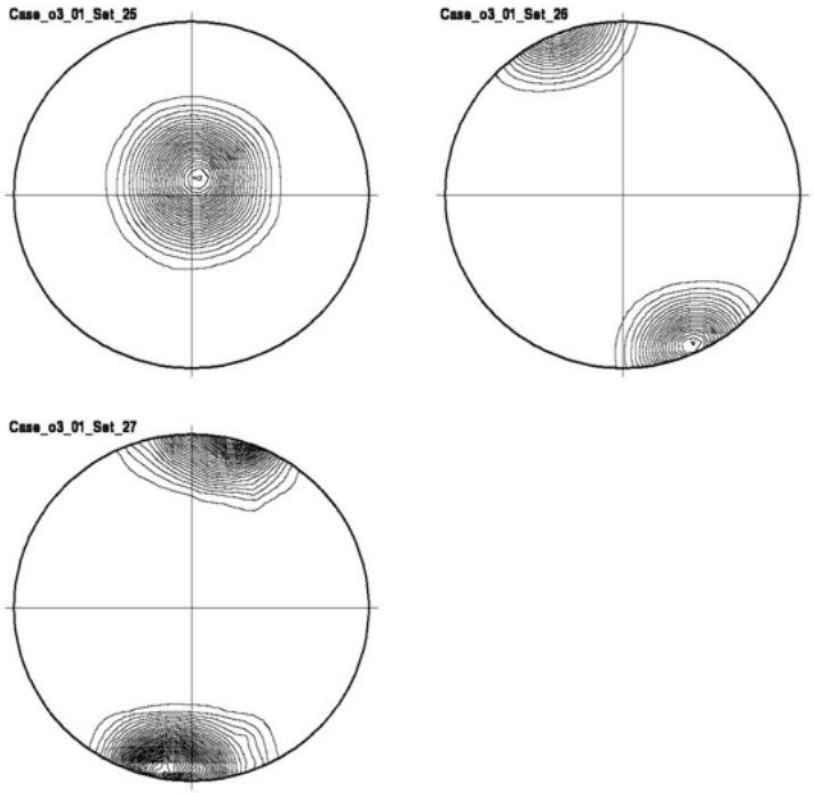

Figure A3.2e. Equal-area stereonet plots of simulated fracture pole directions for the last three fracture sets in fracture domain FFM06, TFM model: (25) SH global, (26) ENE local, and (27) EW global.

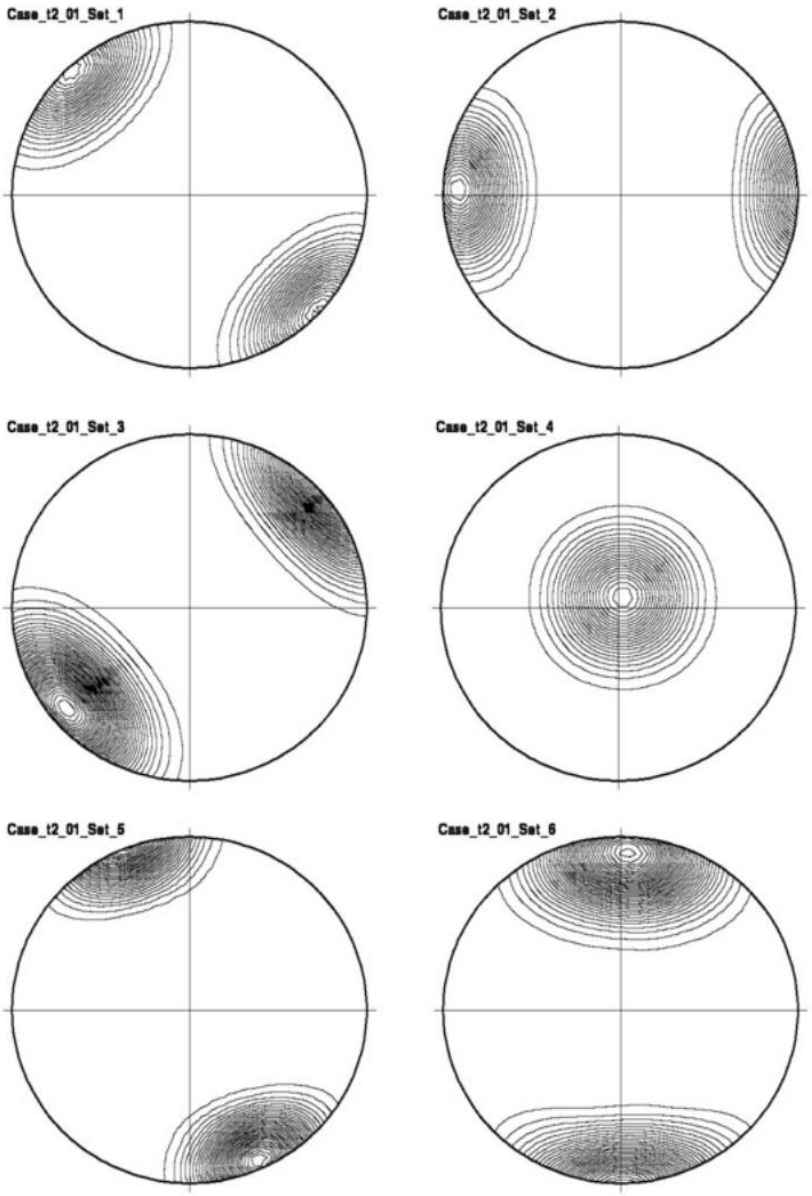

Figure A3.3a. Equal-area stereonet plots of simulated fracture pole directions for the first six fracture sets in fracture domain FFM01, TCM model: (1) NE global, (2) NS global, (3) NW global, (4) SH global, (5) ENE local, and (6) EW local.

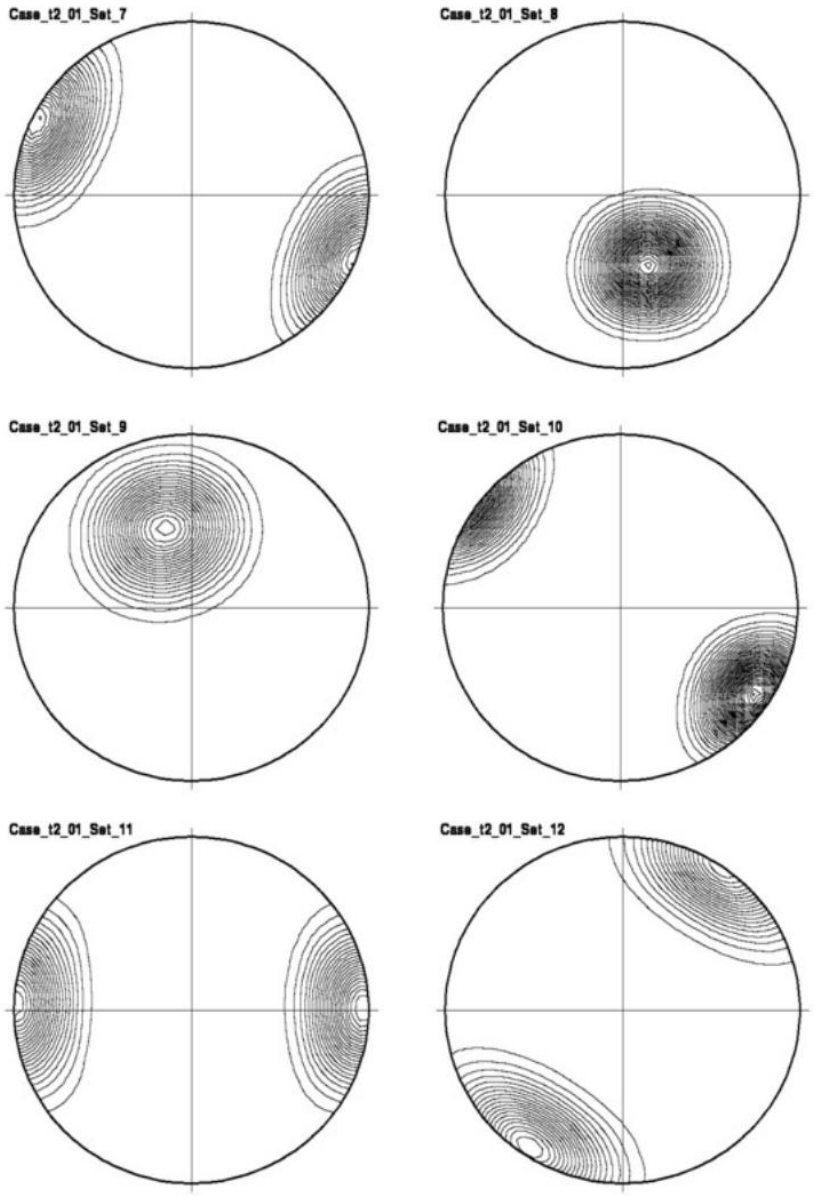

Figure A3.3b. Equal-area stereonet plots of simulated fracture pole directions for the last three fracture sets in fracture domain FFM01, TCM model: (7) NNE local, (8) SH2 local, (9) SH3 local; plus the first three sets of FFM06: (10) NE global, (11) NS global), and (12) NW global.

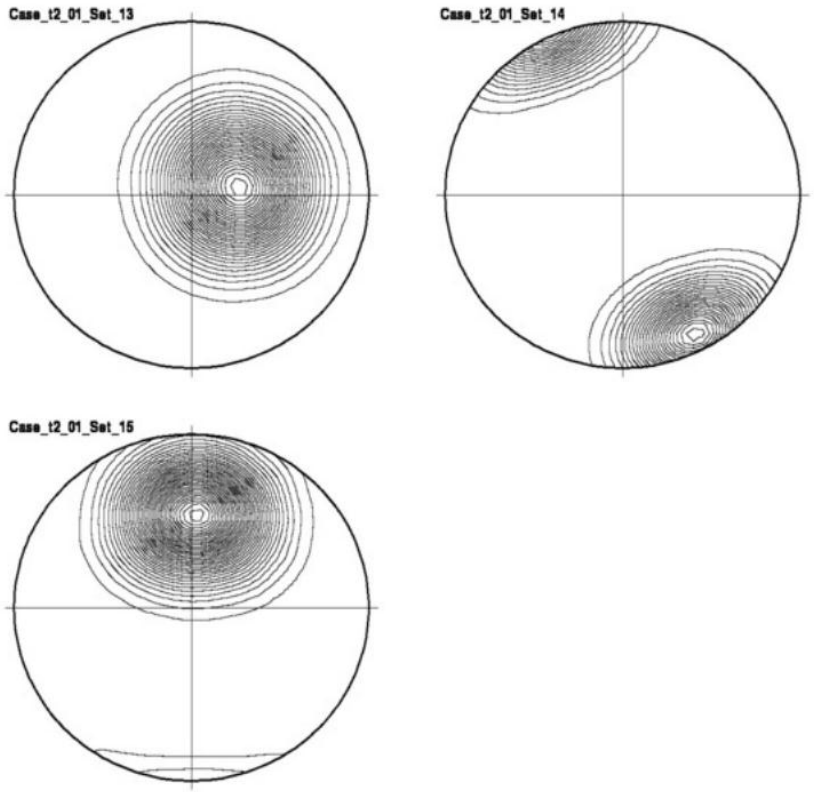

Figure A3.3c. Equal-area stereonet plots of simulated fracture pole directions for the last three fracture sets in fracture domain FFM06: (13) SH global, (14) ENE local, and (15) SH2 local.

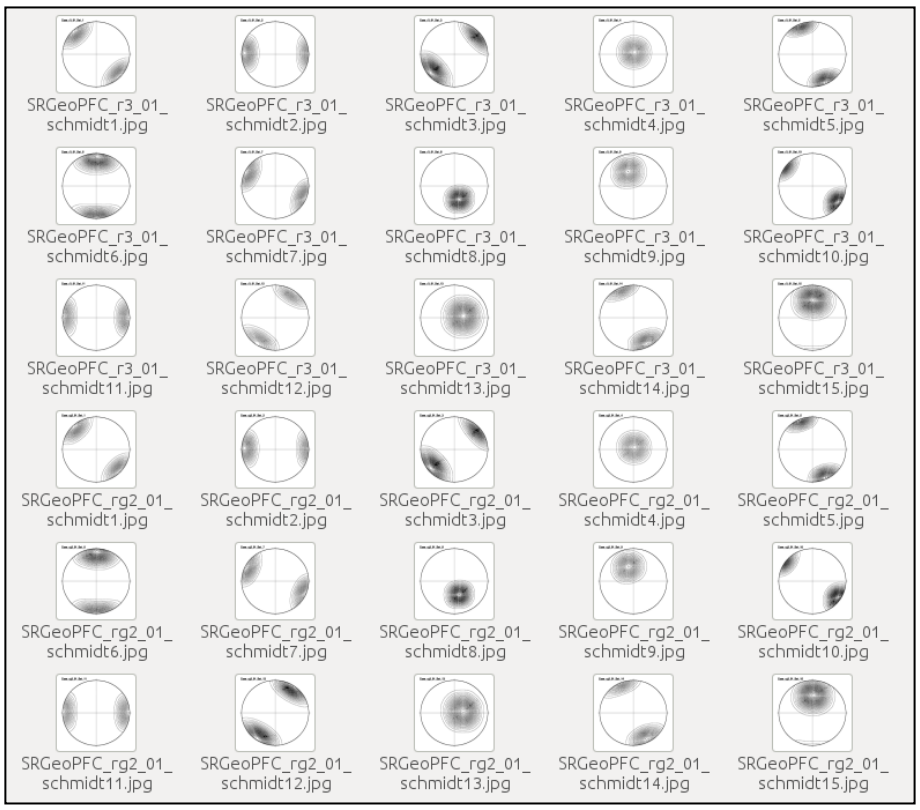

Figure A3.4. Comparison of equal-area stereonet plots of simulated fracture pole directions for the r_0-fixed model base case (calculation case r3, top 15 plots) versus the elevated P_{32} variant (calculation case rg2, bottom 15 plots).

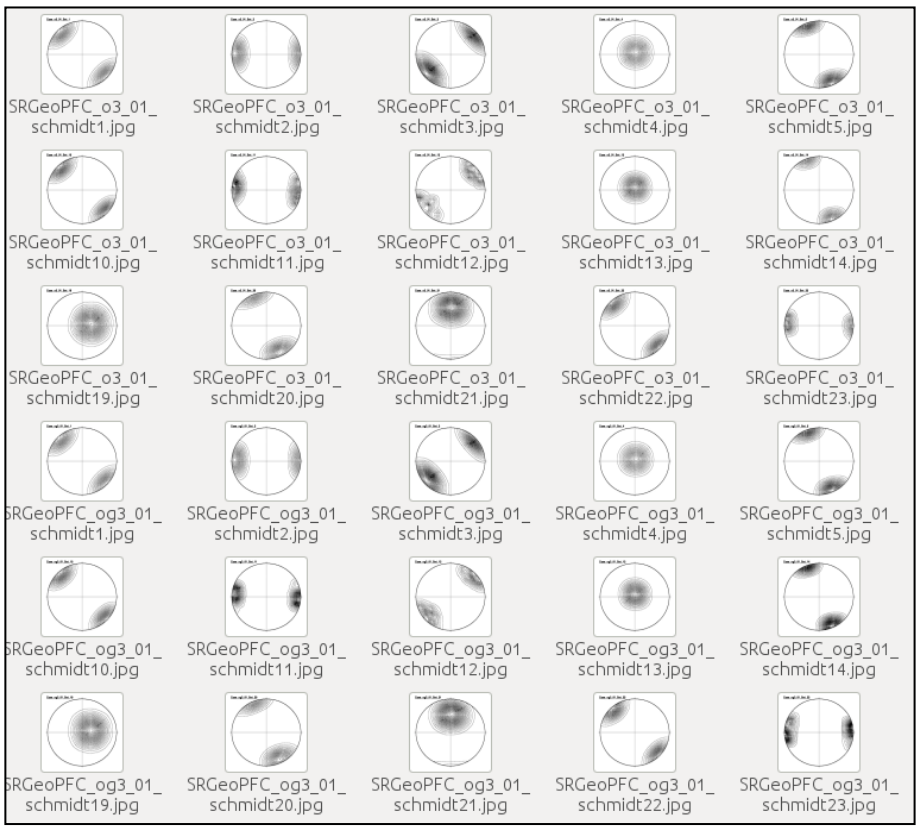

Figure A3.5a. Comparison of equal-area stereonet plots of simulated fracture pole directions for the OSM-TFM model base case (calculation case o3, top 15 plots) versus the elevated P_{32} variant (calculation case og3, bottom 15 plots).

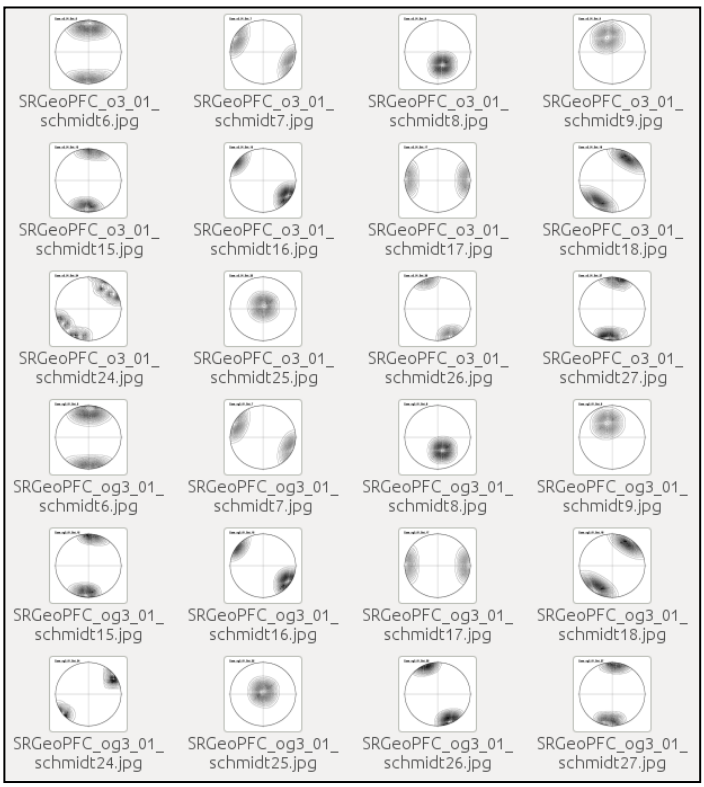

Figure A3.5b. Comparison of equal-area stereonet plots of simulated fracture pole directions for the OSM-TFM model base case (calculation case o3, top 12 plots) versus the elevated P_{32} variant (calculation case og3, bottom 12 plots).

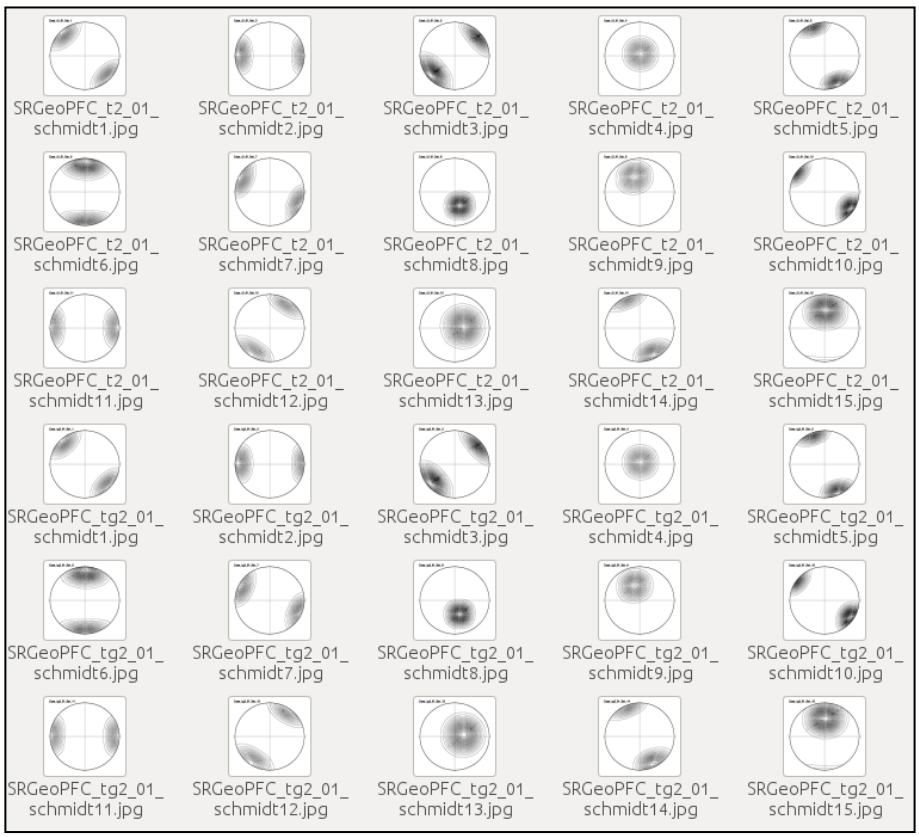

Figure A3.6. Comparison of equal-area stereonet plots of simulated fracture pole directions for the TCM model base case (calculation case t2, top 15 plots) versus the elevated P_{32} variant (calculation case tg2, bottom 15 plots).

2014:44

The Swedish Radiation Safety Authority has a comprehensive responsibility to ensure that society is safe from the effects of radiation. The Authority works to achieve radiation safety in a number of areas: nuclear power, medical care as well as commercial products and services. The Authority also works to achieve protection from natural radiation and to increase the level of radiation safety internationally.

The Swedish Radiation Safety Authority works proactively and preventively to protect people and the environment from the harmful effects of radiation, now and in the future. The Authority issues regulations and supervises compliance, while also supporting research, providing training and information, and issuing advice. Often, activities involving radiation require licences issued by the Authority. The Swedish Radiation Safety Authority maintains emergency preparedness around the clock with the aim of limiting the aftermath of radiation accidents and the unintentional spreading of radioactive substances. The Authority participates in international co-operation in order to promote radiation safety and finances projects aiming to raise the level of radiation safety in certain Eastern European countries.

The Authority reports to the Ministry of the Environment and has around 315 employees with competencies in the fields of engineering, natural and behavioural sciences, law, economics and communications. We have received quality, environmental and working environment certification.

Strålsäkerhetsmyndigheten
Swedish Radiation Safety Authority

SE-171 16 Stockholm
Solna strandväg 96

Tel: +46 8 799 40 00
Fax: +46 8 799 40 10

E-mail: registrator@ssm.se
Web: stralsakerhetsmyndigheten.se